

Advanced Computer Simulations Of Nanomaterials And Stochastic Biological Processes

Maria S. Minakova

A dissertation submitted to the faculty of the University of North Carolina at Chapel Hill in partial fulfillment of the requirements for the degree of Doctor of Philosophy in the Department of Chemistry.

Chapel Hill

2012

Approved by:

Garegin A. Papoian

John Papanikolas

Christopher Fecko

Richard Cheney

Max Berkowitz

Michael Rubinstein

Abstract

Maria S. Minakova: Advanced Computer Simulations Of Nanomaterials And Stochastic
Biological Processes

(Under the direction of Dr. Garegin A. Papoian and Dr. John Papanikolas)

This dissertation consists of several parts. The first two chapters are devoted to of study of dynamic processes in cellular organelles called filopodia. A stochastic kinetics approach is used to describe non-equilibrium evolution of the filopodial system from nano- to micro scales. Dynamic coupling between chemistry and mechanics is also taken into account in order to investigate the influence of focal adhesions on cell motility.

The second chapter explores the possibilities and effects of motor enhanced delivery of actin monomers to the polymerizing tips of filopodia, and how the steady-state filopodial length can exceed the limit set by pure diffusion. Finally, we also challenge the currently existing view of active transport and propose a new theoretical model that accurately describes the motor dynamics and concentration profiles seen in experiments in a physically meaningful way.

The third chapter is a result of collaboration between three laboratories, as a part of Energy Frontier Research Center at the University of North Carolina at Chapel Hill. The work presented here unified the fields of synthetic chemistry, photochemistry, and computational physical chemistry in order to investigate a novel bio-synthetic compound and its energy transfer capabilities. This particular peptide-based design has never been studied via Molecular Dynamics with high precision, and it is the first attempt known to us to simulate the whole chromophore-peptide complex in solution in order to gain detailed information about its struc-

tural and dynamic features.

The fourth chapter deals with the non-equilibrium relaxation induced transport of water molecules in a microemulsion. This problem required a different set of methodologies and a more detailed, all-atomistic treatment of the system. We found interesting water clustering effects and elucidated the most probable mechanism of water transfer through oil under the condition of saturated Langmuir monolayers.

Together these computational and theoretical studies compose a powerful and diverse set of physical approaches and both analytical and numerical methodologies, that can be successfully applied in the fields of biology, chemistry and biophysics.

Acknowledgements

I am delighted to express my sincere gratitude to the people who made this dissertation possible. First and foremost I am most deeply grateful to my advisor, Dr. Garegin Papoian. His contagiously positive attitude, exceptional scientific intelligence and talent to provide constructive criticism inspired me to apply to graduate school at the first place and guided me through this long and intricate process. His audacity in exploration of such a wide range of computational and theoretical research areas always inspires me. I'm sincerely grateful for the opportunities he offered that allowed me to learn new skills in a variety of projects and to better understand modern scientific process.

Looking at the big picture, I'm infinitely grateful to my beloved mother Irina Minakova, who encouraged me to pursue science, even if it implied traveling across the ocean. She is my beacon of kindness and hope: two qualities that make any success more joyful and any misfortune more bearable.

My group members are undoubtedly an invaluable source of new ideas, fruitful scientific and life discussions, emotional support and true camaraderie. I would like to especially thank Dr. Davit Potoyan, Dr. Christopher Materese, Dr. Pavel Zhuravlev, Aram Davtyan, Dr. Lonhua Hu, Dr. Konstantin Popov, Dr. Ignacia Echeverria, and Stephanie Bettis. I'm also very grateful to the students and postdocs in Dr. Papanikolas group, who made me feel welcome at UNC after the majority of my lab has moved to the University of Maryland.

I thank people in Chemistry Department and Medical School at the University of North

Carolina at Chapel Hill, as well as faculty and students of IPST at the University of Maryland at College Park, who organized research seminars inviting brilliant and prominent speakers. Such active scientific environment greatly affected my shaping as a scientist.

There are also people who greatly contributed specifically to the research presented in this dissertation. I am grateful to Dr. Richard Cheney and his research group members for helpful discussions about possible roles of Myosin proteins in filopodia and stereocilia.

The majority of work presented here was done using UNC Killdevil, Topsail(retired), Emerald(retired) supercomputers, which are outstanding computational resources. I'm especially thankful to Jenny Avis Williams for her outstanding dedication to help researches with any possible technical difficulties and educate them about new and more effective ways to perform high-performance computing.

Table of Contents

List of Tables	ix
List of Figures	x
1 Introduction	1
2 Mechanochemistry of Nascent Adhesions in Filopodia	6
2.1 Introduction	6
2.2 Methods	8
2.2.1 Filopodial system composition and setup	8
2.2.2 Simulation scheme of the stochastic processes involved	11
2.2.3 Bundle relaxation due to polymerization	12
2.2.4 Model parameters	17
2.2.5 Modeling the Nascent Adhesions	17
2.2.6 Modeling the cell substrate	19
2.3 Results and discussion	20
2.3.1 Retrograde flow dependence on NA binding rate	21
2.3.2 Retrograde flow dependence on NA rupture force	23
2.3.3 Retrograde flow dependence on substrate stiffness	24
2.3.4 Different regimes in growth dynamics	28

2.4	Conclusions	30
3	Theory of Active Transport in Filopodia and Stereocilia	32
3.1	Introduction	32
3.2	Methods	34
3.2.1	Model parameters	34
3.2.2	Stochastic simulations	35
3.2.3	Retrograde flow	35
3.2.4	The boundary conditions	36
3.3	Results and discussion	38
3.3.1	Motor distributions	38
3.3.2	Phantom motors model failure	40
3.3.3	Finite filament capacity	41
3.3.4	Jammed motors	41
3.3.5	Transport of actin	48
3.4	Conclusions	54
4	Position-Dependent Energy Transfer between Ruthenium(II) and Osmium(II) Modified Coiled-Coil α-Helical Peptide Dimers	57
4.1	Introduction	57
4.2	Methods	60
4.2.1	MD Simulation Protocol	60
4.3	Results and discussion	64
4.3.1	<i>2f-Os/2f-Ru</i> Heterodimer	64
4.3.2	<i>2c-Os/2b-Ru</i> Heterodimer	67
4.3.3	<i>2g-Os/2e-Ru</i> Heterodimer	69
4.4	Conclusions	74

5	Non-equilibrium Water Transport in a Nonionic Microemulsion System	76
5.1	Introduction	76
5.2	Methods	78
5.2.1	MD Simulation Protocol	78
5.2.2	Cluster Analysis	79
5.3	Results and discussion	81
5.4	Conclusions	89
A	Supplementary information for the manuscript "Theory of Active Transport in Filopodia and Stereocilia"	91
A.1	Efficiency of active transport and non-monotonic profile	91
A.2	The boundary conditions	91
A.3	Detailed balance in the motor part	94
A.4	G-actin profiles and experiments	95
A.5	More connections to experiments	96
A.6	Retrograde flow	96
B	Supplementary videos for Chapter 4	98
	Bibliography	108

List of Tables

2.1	Model parameters	18
4.1	Helical stability and metal-metal distance measurements	65
4.2	Helical stability measured using Guanidinium denaturation	70
4.3	Dependence of the energy transfer rate on the position: global analysis	72

List of Figures

1.1	Simulation methods applied for processes of various length and time scales. . .	2
2.1	Schematic representation of the filopodial system with a substrate and NAs . . .	9
2.2	Bundle relaxation due to polymerization: scheme and applied forces	13
2.3	Time evolution of the bundle tip and pointed end coordinates	16
2.4	Retrograde flow speed dependence on NA binding rate	22
2.5	Retrograde flow speed dependence on NA rupture force F_{rupt}	23
2.6	Retrograde flow speed dependence on substrate stiffness κ_{sub}	25
2.7	Diagram of filopodial dynamic states as a function of F_{rupt} and k_{on}	27
2.8	Examples of various dynamic regimes in the filopodial system	29
3.1	Kinetics scheme of chemical reactions for a filopodium system	39
3.2	Comparison of the mean field analytical models with stochastic simulations . . .	42
3.3	Motor concentration profiles inside a filopodium: jammed motors model	44
3.4	G-actin concentration profiles for different parameter values	48
3.5	Active transport fluxes for different parameter values	53
3.6	Concentration profiles for actin-on-the-motors $A(z)$ and motors $c_b(z)$	55
4.1	Schematic representation of the chromophore-peptide system	59
4.2	Peptide sequence and helical heptad repeat scheme	61
4.3	Metal-metal distance distribution for various chromophore placements	66
4.4	Fraction of α -helical content in each peptide as a function of time	68
4.5	Snapshots of typical spacial "stacking" chromophore arrangements	70
4.6	Time-resolved emission transients for the metallopeptide systems	73

5.1	Snapshot of the system and examples of observed water-surfactant complexes	82
5.2	Probability distribution function for 1D "water only" clustering	84
5.3	Marginal probability distribution for 2D "water+surfactant" clustering	85
5.4	Radial distribution functions for various water and surfactant atom pairs	86
5.5	Number fraction distributions across the microemulsion slab	87
A.1	Actin concentration profiles	92

Chapter 1

Introduction

Computational chemistry and biophysics are relatively modern fields in natural sciences, and they are slowly becoming powerful and indispensable parts of theoretical investigations in the corresponding fields. The invention of computing machines not only allowed theoretical scientists to successfully perform incredibly complicated calculations, but also, for the first time in history, design and run *numeric experiments*, e.g. modeling of a process evolving in time. We can construct numerical experiments that are yet unfeasible experimentally, and (dis)proof new and existing concepts of how the world works. Nowadays modeling is neither a fancy toy for privileged minds, nor it is sophisticated exotic decoration for the experimental data. Simulations and analytical theory compose an essential scientific approach to answer "what?" and "why?" questions rising in various research projects.

Having said that, we have to acknowledge the fact simulations should necessarily be performed in conjunctions with experimental studies of the same process in order to be relevant and verifiable. To achieve consistency, the design of a numerical experiment should be accurate and efficient [1]. Given the variety of accessible simulation methods, one should carefully choose an approach that can provide us with the most precise information within the reasonable amount of time.

Several theoretical and modeling methods are placed on the time and length scale plot, as shown in Figure 1.1 along with the names of the research projects in parentheses, including

those applied for the research projects presented herein (see Figure 1.1).

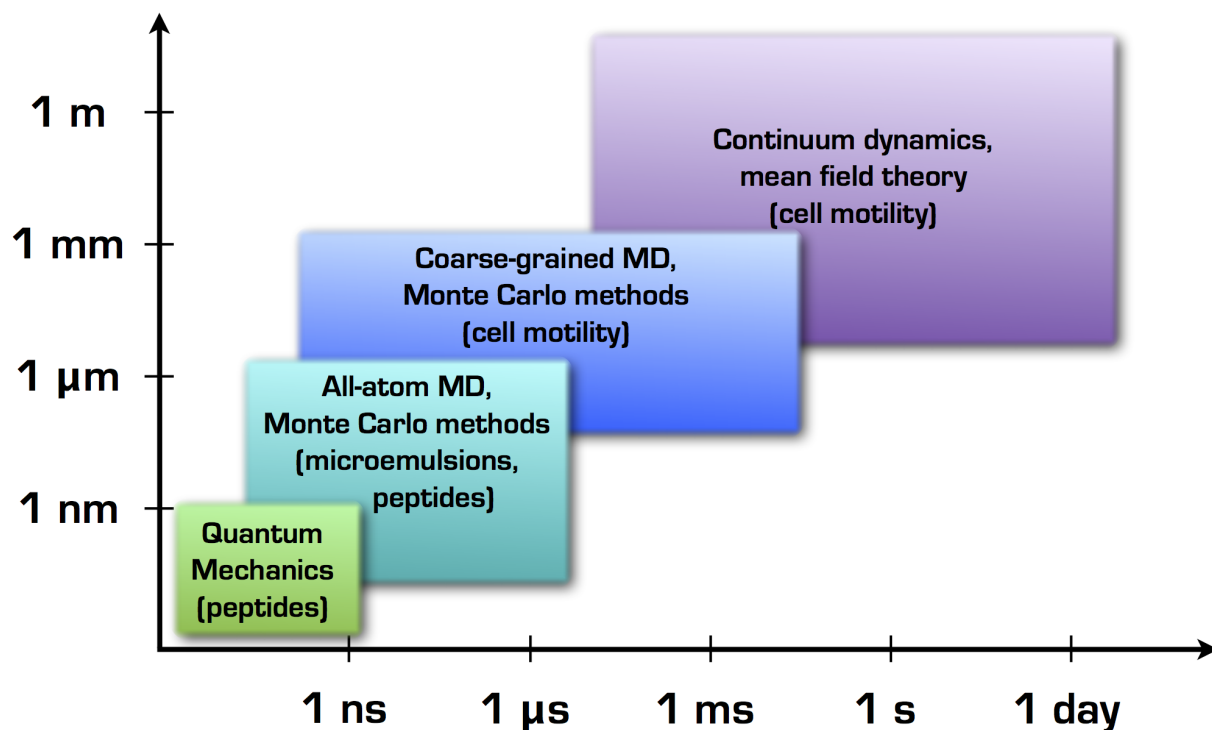


Figure 1.1: Quantum Mechanics provides a variety of *ab initio* calculation methods, including Density Functional Theory (DFT) utilized for the parametrization of Ruthenium-based chromophores (see, Chapter 4), and even hybrid methods that include both all-atom molecular dynamics and quantum mechanics. All-atom Molecular dynamics is based on propagation of Newton Laws time and space. All-atom MD has been utilized to study microemulsions system in Chapter 5 and new peptide grafter chromophore system in Chapter 4. All-atom can also include additional constructs imposing proper temperature, pressure and structural constraints on the system. When all-atom representation becomes inefficient a simplified Coarse-grain models can be derived from All-atom MD and extend the dynamics studies to larger sizes and longer timescales. Probabilistic methods majority of which are based on Monte Carlo-Metropolis algorithm can not provide detailed information about kinetics and dynamics, but allow extensive sampling of the phase space with correct statistical distributions. A Monte-Carlo derived approach was utilized in Chapters 1-2 to study various aspects of cell motility. At some point when the system size is large enough it can be treated via self-consistent field theories with possible use of perturbations or other non-equilibrium techniques, as was done in Chapter 1 to compare analytical theory with detailed stochastic simulations.

First, note that these blocks are distributed mainly along the diagonal. This happens to be

so, because the majority of chemical and biological processes that we can observe and study have an internal correlation in space and time. Events happening on smaller length scales occur in shorter time periods, and the larger the system size is, the longer the time period will be for the transformations to take place. The exact form of the functional dependence between propagation in space and time depends on the process, for example, for the diffusion-based processes it is $t \propto L^2$.

Second, the applicability of these methods to other regions of time-length scale plot works only in one direction: from the bottom to the top. While approximate methods, such as coarse-grained and continuum dynamics, are essentially derived from higher resolution methods, they omit significant amount of information and contain drastic simplifications. If it was computationally feasible to apply *brute force* and run higher resolution simulations for larger time and length scales, it would be done so.

The detailed introduction into the computational methods showed in Figure 1.1 and their comparative analysis can be found in several excellent books [1–3]. The variety of computational and analytical approaches that is presented in this dissertation is based on the specific research questions. For example, when a microemulsion slab is undergoing non-equilibrium relaxation, the transport of matter is often observed on a micro- and mesoscopic scales (see Chapter 5). The macroscopic experimental measurements are unable to explicitly show, how such transport is facilitated. Meanwhile all-atom Molecular Dynamics (MD) can study this microscopic transport down to the level of following one water molecule through the surfactant and consequently oil layers. It can provide data to elucidate specific water-surfactant interactions responsible for molecules association and migration through the hydrophobic medium.

Another good candidate for all-atom MD is a new synthetic compound, for which exact structural and dynamic properties are often unknown. Ruthenium-based chromophores planted on coiled coils is an example of a new semi-biological and semi-synthetic molecular system, which aims to have precisely controllable energy and electron transfer properties, as discussed

further in Chapter 3. Ability to maintain such control requires detailed knowledge of how chromophores move in space under normal conditions, how they interact with each other and the underlying peptide scaffold. All this information is extremely difficult to obtain from experiments, but it is directly accessible in visual and statistical forms from all-atom MD (see Chapter 3). Although all-atom MD can not simulate energy and electron transfer directly, the observed chromophore packing conformations can be plugged in Quantum Mechanical (QM) calculations to study electron structure coupling and estimate energy transfer propensity for each packing conformation.

If we consider dynamics of biological systems and microorganisms, the naturally rising length scale range is between the size of one protein and the size of the whole cell or a microorganism. For instance, when a cell samples environment around it, it grows long needle-like protrusions, called filopodia. The size and lifetime of these organelles are largely determined by their function. Filopodial growth and retraction is assisted by a variety of regulatory proteins and molecular proteins, and it also depends on the mechanical properties of both the cell and its environment (see more details in Chapters 1-2).

Moreover, the dynamics of a filopodium is dissipative in energy through consumption of the “energy molecule” ATP and is essentially a non- equilibrium (de) polymerization of the globular protein actin. Therefore the smallest piece in the system is one actin monomer and the fastest event is diffusion. This particular system presents a challenge of integrating the fields of stochastic dynamics, chemistry, biology and mechanics, and can be successfully described using Monte-Carlo type of simulations, that coarse grains some of the nano-scopic dynamics and accounts for many body effects and the uncertainty about initial conditions via implementing random variables into the system evolution (see Chapters 1-2). If such system is capable of reaching a steady-state within the time scale of observation, a self-consistent field approach can be used to create a qualitative model of the process and compare it with the numeric experiments, as was done in Chapter 2. This approach ignores microscopic details and

fluctuations in the dynamics, but it can elucidate main and secondary factors defining specific dynamic behavior and allows us to better understand the first design principles of the biological systems.

Chapter 2

Mechanochemistry of Nascent Adhesions in Filopodia *

2.1 Introduction

Focal Adhesions (FAs) play an important role in cell motility and sometimes have lethal impact on the whole cell cycle [4,5]. They have been extensively studied experimentally [6–8] and recently gained significant interest from computational and theoretical scientists as well [9, 10]. Since Focal Adhesions is effectively an "umbrella" term, and it may imply different complexes from nascent nanoscale protein aggregations that link cell cytoskeleton with the extra cellular matrix (ECM) to the large micron size protein conglomerations that include stress fibers and dynamic multi protein complexes that function in a cooperative fashion [11, 12], we are going to use the term Nascent Adhesions (NAs) to describe the small cytoskeletal links to ECM inside filopodia. The properties of different kinds of NAs differ on many levels, including chemical composition, topology, structural arrangement, mechanical properties and dynamic behavior. No single model can describe all these different structures, however the majority of NAs appear to share a lot in common, if they are considered at a certain moment of the cell cycle. For example, nascent NAs formed at the cell frontier have a specific purpose to let the cell grow or move forward to a certain point in order to decide, if that direction is preferable.

Therefore these structures should have such strength and longevity that would allow poly-

*Maria Minakova, Garegin A. Papoian

merization and other migration related processes to take place within the NAs lifetime. Simultaneously NAs have to be highly responsive to both the intra- and extracellular signals to allow the cell to adapt to the dynamically changing environment. Indeed, NA breakage can dramatically affect the direction and speed of motion. It has been proposed that nascent NAs form at the cell front in both lamellipodia and filopodia [13]. NAs embedded in lamellipodia are thought to be responsible for the mobility of the cell front and contribute to the activation of pulling the rest of the cell body forward, toward the chosen direction [13]. The role of NAs in filopodia is more elusive. Since filopodia are very thin, long and highly mobile, the contribution of NAs formed on their tips is likely a not very significant factor in the mechanics of the cell's body. However, nascent NAs clearly play an important role for the filopodial dynamics, that in turn affect the cell sensing ability and consequently the cell motility activation or inhibition.

Moreover, the question of filopodial growth up to the lengths observed experimentally is still open. Competition of diffusion and retrograde flow sets a limit on how far a filopodium system can grow, given the G-actin concentration in the bulk and the average speed of retrograde flow [14]. Indeed, the equality between the diffusional flux of G-actin monomers toward the tip and the retrograde flow flux that pulls polymerized filamentous actin (F-actin) back to the cell bulk (see Figure 2.1) determines the steady-state filopodial length [14]. Given the experimentally measured model parameters, this approach yields a steady-state filopodial length $\approx 1\mu m$. On the other hand, certain cells can grow filopodia up to $\approx 15 - 100\mu m$ [15–17] with speeds, that exceed the growth velocity given by diffusion alone. In order to address this discrepancy, several plausible hypotheses have been offered in the biophysical community, including active transport by tip-directed motors [18] and actively modulated hydrodynamic flows [19].

In this study we would like to explore a different mechanism that can significantly contribute to the filopodial growth and retraction dynamics, and it involves retrograde flow mod-

ulation by NAs. The retrograde flow is an active flux counteracting diffusion and consequent actin polymerization. It is created by clusters of myosin II motors that bind to two filaments and pull them against each other, creating an effective sliding motion [20–22]. However classic kinetic models do not contain any mechanic components that could affect the force balance, slow down such sliding motion, and hence diminish the retrograde flow itself. It has to be mentioned that membrane tension contributes to the retrograde flow as well, but an average force generated by the membrane pulled away from the cell has been measured to be ≈ 10 pN [23, 24], while a cluster of 5-50 myosin motors can generate forces on the order of 100-1000 pN [25, 26].

We have developed a highly detailed model of a filopodium organelle with an explicit two-dimensional (2D) substrate and NAs that are both chemically active species and elastic springs, that store and transfer stress from the substrate across the membrane to the filopodial bundle. We coupled the kinetic rates to the mechanical stress and implemented energy minimization and force balance calculations in the filopodial system. Such integrated approach allowed us to study in detail the filopodial dynamics in the presence of a substrate and NAs, extensively sample the parameter phase space, and compose a diagram of dynamic regimes exhibited by this system.

2.2 Methods

2.2.1 Filopodial system composition and setup

A schematic representation of our filopodial system is shown in Figure 2.1. It consists of $N=16$ actin filaments (F-actin), while the monomeric actin (G-actin) bound to ATP can diffuse inside a filopodial tube from the bulk (the left boundary) to the tip (the right boundary).

The enveloping membrane is represented by a fluctuating force at the tip, that can slow

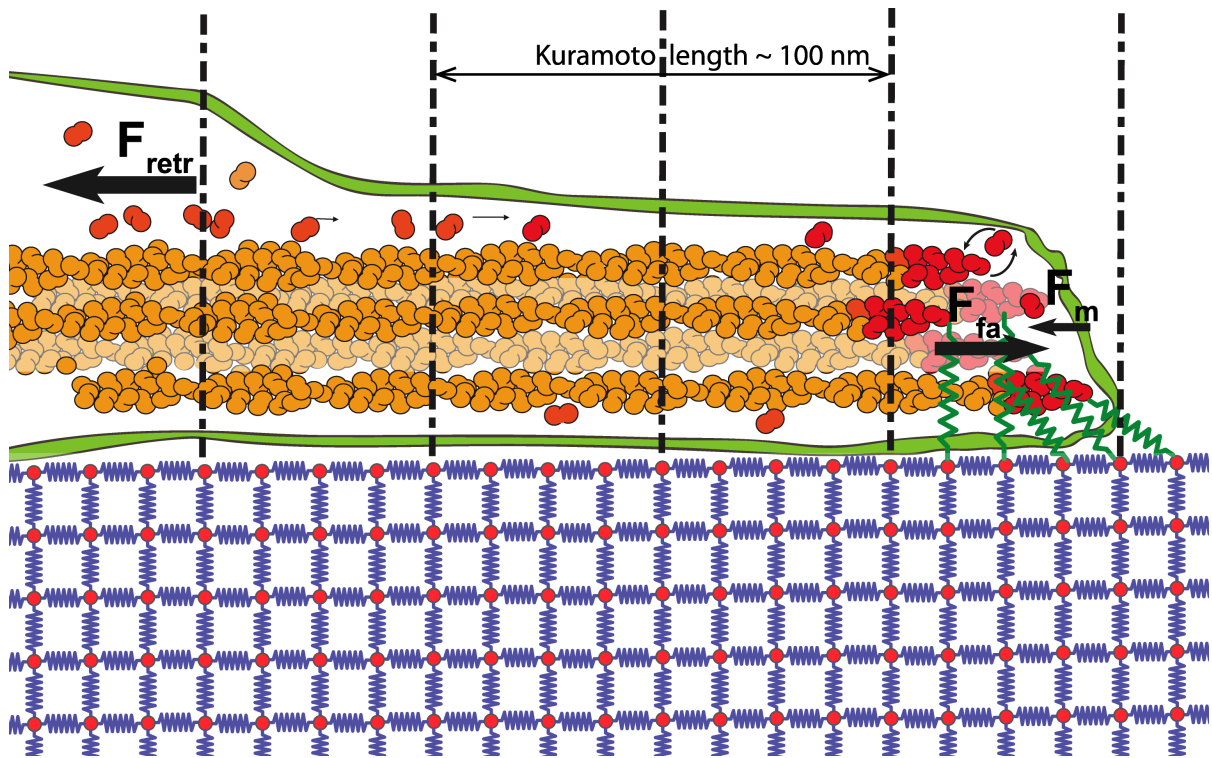


Figure 2.1: Illustration of the filopodial system containing 16 actin filaments, diffusing G-actin; Fluctuating membrane that affects polymerization at the tip, Nascent Adhesions (NAs) that have dual nature of chemically active species and elastic springs if attached to substrate and filaments (discussed in detail further); Retrograde flow contribution by myosin motors is modeled as a constant force F_{retr} ; and 2D substrate consisting of beads connected by elastic springs.

down the polymerization. This type of mechanochemical coupling corresponds to the "brownian ratchet model" [27]. Since actin filaments have a persistence length $\approx 10 \mu m$ [28] and are also bundled by regulatory proteins, we assume them to have a linear conformation and behave as incompressible rods.

The activity of myosin motors on the base (the left boundary) is modeled as a constant pulling force F_{retr} , which contributes to the net retrograde flow along with the membrane surface tension F_m pushing toward the filopodial base. It is possible to make both contributions stochastic, however there is no reliable information on their probability distributions or correlation functions. Therefore we take into account only average values of F_{retr} and assume Gaussian probability distribution for F_m .

NAs are in reality membrane bound protein complexes that can bind to F-actin and to the substrate through the cell membrane. Therefore the formation of NA is a multi-step process. In our coarse-grained model we assume NAs formation to be an one-step kinetic reaction, where the k_{on} rate is given by the slowest binding and k_{off} rate corresponds to the weakest bond in the whole complex, which is between NA and F-actin. It has been shown that the extra cellular bonds mediated by integrins can be very strong, and in many cases it is easier to pull the integrin complex out of the cell membrane, than to break a bond between NA and the substrate [12,29]. Therefore, when NA formation reaction happens, we assume that the extra cellular end of the NA is already bound to a bead on the substrate. When NA is active, i.e. bound to F-actin, it acts as an elastic spring and contributes to the force balance inside the filopodium and potential energy of the substrate as well.

The filopodium model shown in Figure 2.1 also contains an explicit 2D substrate, that is represented by a network of beads, connected by elastic springs. It is discussed in more detail in the corresponding methods section.

2.2.2 Simulation scheme of the stochastic processes involved

In order to optimize the performance of our simulations, we coarse-grain our dynamics to avoid spending the majority of time simulating brownian dynamics. The mechanical events were considered to be the fastest to occur, so all mechanical components have enough time to equilibrate in between the reactions.

The filopodial tube is divided into compartments, each $l_c=54$ nm long, so that the furthest distance between two species in the neighboring compartments is on the order of 100 nm. It corresponds to a mean free path for a protein species in the cytosol, before it can meet and react with another species. This quantity is also called Kuramoto length [30]. Therefore, we do not simulate diffusion of species inside one compartment and consider the events on the larger time scales, assuming fast equilibrium within one compartment. Species inside one compartment can participate in chemical reactions with probabilities given by the corresponding kinetic rates.

The main circuit of our computational modeling is a Monte Carlo approach spatially resolved in 1D, which is also called the direct Gillespie algorithm [31,32]. During the simulation we iteratively perform the following steps:

- a) the first random number is thrown to determine Δt time interval between the previous and next events, taking into consideration all possible chemical and diffusion events;
- b) all reaction rates that depend on the mechanical properties are updated;
- c) the second random number is thrown to choose a particular event for realization;
- d) if the chosen reaction is potentially force-generating (polymerization or involving NAs) potential energy is minimized and force balance is calculated;
- e) retrograde flow is calculated from the force balance inside a filopodium, and the filopodial system is shifted back by $\sim v_r \cdot \Delta t$. It should be mentioned that the center of mass of the substrate is not affected by the retrograde flow. However the retrograde flow affects the positions of active NAs, which in turn create additional pulling forces on the NA-connected

substrate beads. By the end of each simulation we have records of concentrations for all species including NAs, filament lengths, retrograde flow speed, substrate bead positions.

2.2.3 Bundle relaxation due to polymerization

What happens with the filopodial bundle, if it elongates by the length of one monomer in the presence of pushing membrane and pulling back myosin motors? In more microscopic view this setup corresponds to all N filaments getting polymerized by one monomer and becoming $(M+1)$ monomers long. Let us consider a more coarse-grained view of a filopodium, shown in Figure 2.2, and look at this system at three moments of time, where a) and c) show the bundle at equilibrium before and after the elongation event correspondingly.

The polymerization of individual filaments can occur due to the membrane fluctuating away from the bundle, so monomers can diffuse into the free space and polymerize. At some intermediate step b) one can assume that elongated bundle of consisting of $(M+1)$ monomers is compressed at its initial length $M \cdot \delta$, where $\delta = 2.7$ nm is the monomer size, and $M \gg 1$. Assuming the bundle to behave as an elastic rod, we can estimate its elastic force $\approx \kappa_{bun} \cdot \Delta l_{bun}$, that pushes equally against lamellipodial actin network at the base (left boundary x_n) and membrane at the tip (right boundary x_m). Both the membrane and the lamellipodial network resist such sliding motion and produce net drag forces, opposing the motion of each boundary x_m and x_n .

Strictly speaking, neither membrane at the tip nor actin network at the base are continuous viscous media with well-defined friction coefficients. In the first order approximation we are going to assume, similar to [10], that both membrane and actin network have effective friction coefficients ξ_m and ξ_n respectively. Exact values for these parameters are not available, however we estimated the appropriate order of magnitude from physical considerations, as discussed further in section 2.2.4. We assume that the actin network shows higher viscous

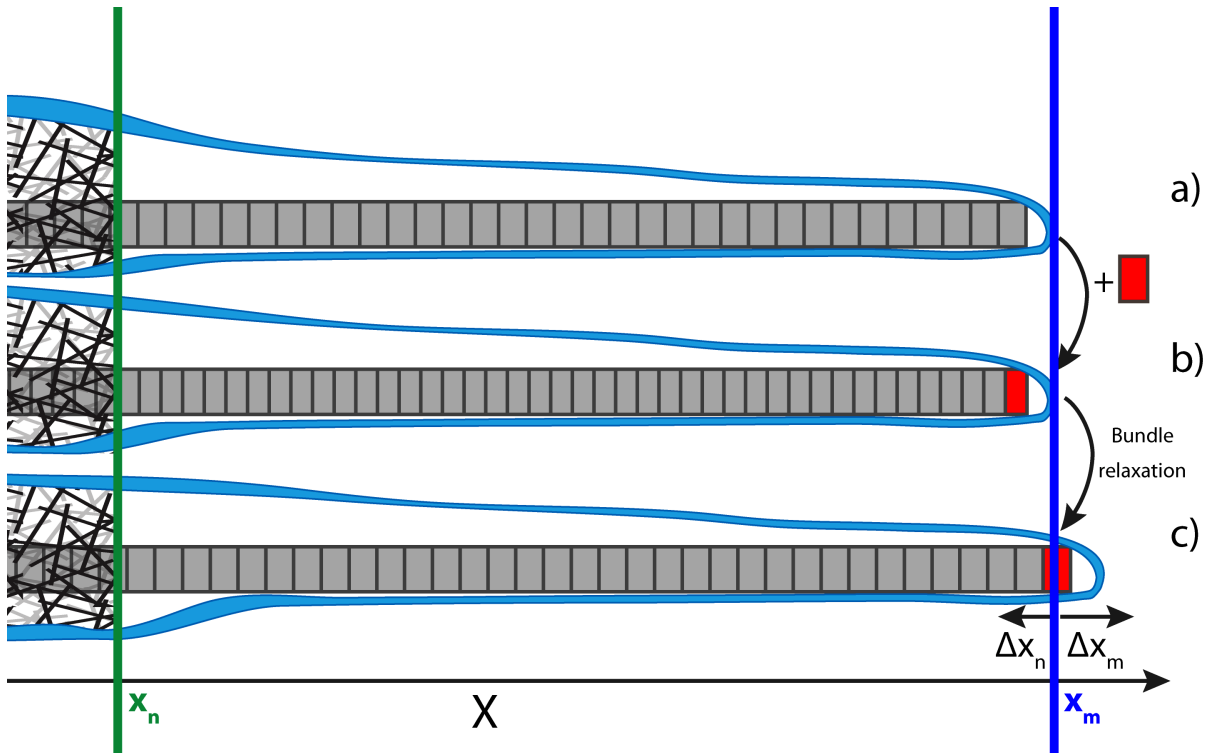


Figure 2.2: A coarse-grained view the filopodial system at three moments of time: a) the bundle of M monomers long before the elongation; b) intermediate step after the elongation by one monomer has happened. For simplicity the bundle is considered to be M monomers long, but to contain $(M+1)$ monomers. It create elastic force pushing the tip forward against the membrane, and pushing pointed end back against lamellipodial network. c) the bundle after the relaxation, where the bundle length is $(M+1)$, and both tip and back coordinates are shifted according to the force balance in the system.

resistivity to bundle pushing, than the membrane. We set $\xi_n = \gamma \cdot \xi_m$, where $\gamma = 4$ is the ratio between membrane and network friction coefficients (see section 2.2.4).

Let us write equations of motion for the bundle end, which is network attached, with the coordinate x_n , and membrane attached tip of the bundle with the coordinate x_m :

$$\begin{cases} \sum F|_n = -\xi_n \dot{x}_n - f_r + \kappa_{bun} \Delta l_{bun}(t) = 0, \\ \sum F|_m = -\xi_m \dot{x}_m - f_m + \sum_i k_{fa} \Delta l_{fa,i} - \kappa_{bun} \Delta l_{bun}(t) = 0. \end{cases} \quad (2.1)$$

The first terms in equations 2.1 are viscous drag forces for the bundle pushing the network and the membrane, f_m and f_r are magnitudes of membrane pushing and retrograde flow pulling forces; and we also add the elastic contribution from all active NAs that resist the sliding motion of the bundle. Bundle length at all times can be written as $\Delta l_{bun}(t) = (x_m(t) - x_n(t)) - (M + 1) \cdot \delta$, and our equations take the following form:

$$\begin{cases} \gamma \xi_m \dot{x}_n - f_{retr} + k_{bun}((x_m - x_n) - (M + 1)\delta) = 0, \\ -\xi_m \dot{x}_m - f_m + \sum_i k_{fa} \Delta l_{fa,i} - k_{bun}((x_m - x_n) - (M + 1)\delta) = 0. \end{cases} \quad (2.2)$$

System of equations 2.2 can be solved numerically at each moment of time, if the NAs number and individual displacements are known. Meanwhile, we can solve the system of equations 2.2 analytically in the absence of NAs, with the following boundary conditions:

$$\begin{cases} x_m(0) = M \cdot \delta, \\ x_n(0) = 0. \end{cases} \quad (2.3)$$

And the solutions take the form:

$$\begin{cases} x_m(t) = \frac{\gamma}{\gamma+1} \left(\frac{\gamma \cdot f_{mem} - f_{retr}}{k_{bun} \cdot (\gamma+1)} - \delta \right) \exp \left(-\frac{\gamma+1}{\gamma} \frac{k_{bun}}{\xi_m} \cdot t \right) - \frac{f_{retr} + f_{mem}}{\xi_m(\gamma+1)} \cdot t + M \cdot \delta, \\ x_n(t) = \frac{-1}{\gamma+1} \left(\frac{\gamma \cdot f_{mem} - f_{retr}}{k_{bun} \cdot (\gamma+1)} - \delta \right) \exp \left(-\frac{\gamma+1}{\gamma} \frac{k_{bun}}{\xi_m} \cdot t \right) - \frac{f_{retr} + f_{mem}}{\xi_m(\gamma+1)} \cdot t \end{cases} \quad (2.4)$$

The analytical solutions 2.4 are plotted in Figure 2.3 and have two time dependent terms: exponential decay corresponding to the bundle relaxation due to the elongation by one monomer, and a linear shift with time, that is given by the balance of forces acting on the bundle. It should be noted, that the speed of relaxation depends only on the bundle rigidity and membrane versus network friction coefficients: $\frac{\gamma+1}{\gamma} \frac{k_{bun}}{\xi_m}$. Also time τ_{relax} required for bundle to reach its new equilibrium length is ≈ 0.01 s.

If the average time required for the bundle elongation $\langle \tau \rangle$ by one monomer is less than this estimate, the bundle would not be able to fully equilibrate between the elongation events. Since the bundle should be at equilibrium when the filopodium reaches a steady-state, we can estimate $\langle \tau \rangle$ from the simulations without NAs that reach a steady-state regime: $\langle \tau \rangle \approx 0.04$ s.

We can also evaluate the maximum number of elongation events per second, given by the polymerization reaction rates $(k_{pol}c_{a,0} - k_{depol})$, where $c_{a,0}$ is bulk concentration of G-actin monomers. This yields $\tau_{min}^{elong} = 1/(k_{pol}c_{a,0} - k_{depol}) \approx 0.01$ s. Since the G-actin concentration at the tip is always much smaller than $c_{a,0}$, $\tau_{min}^{elong} \gg 0.01$ s. Therefore the filopodial bundle should have enough time to equilibrate between elongation events. This conclusion allows us avoid solving the problem of bundle relaxation dynamically, and rather adjust bundle's bottom and top coordinates by the corresponding fraction of a monomer size to account for the relaxation between the elongation events.

It should be noted that this adjustment showed to be a minor correction to the filopodial dynamics and did not significantly change the observed behavior in the presence of NAs.

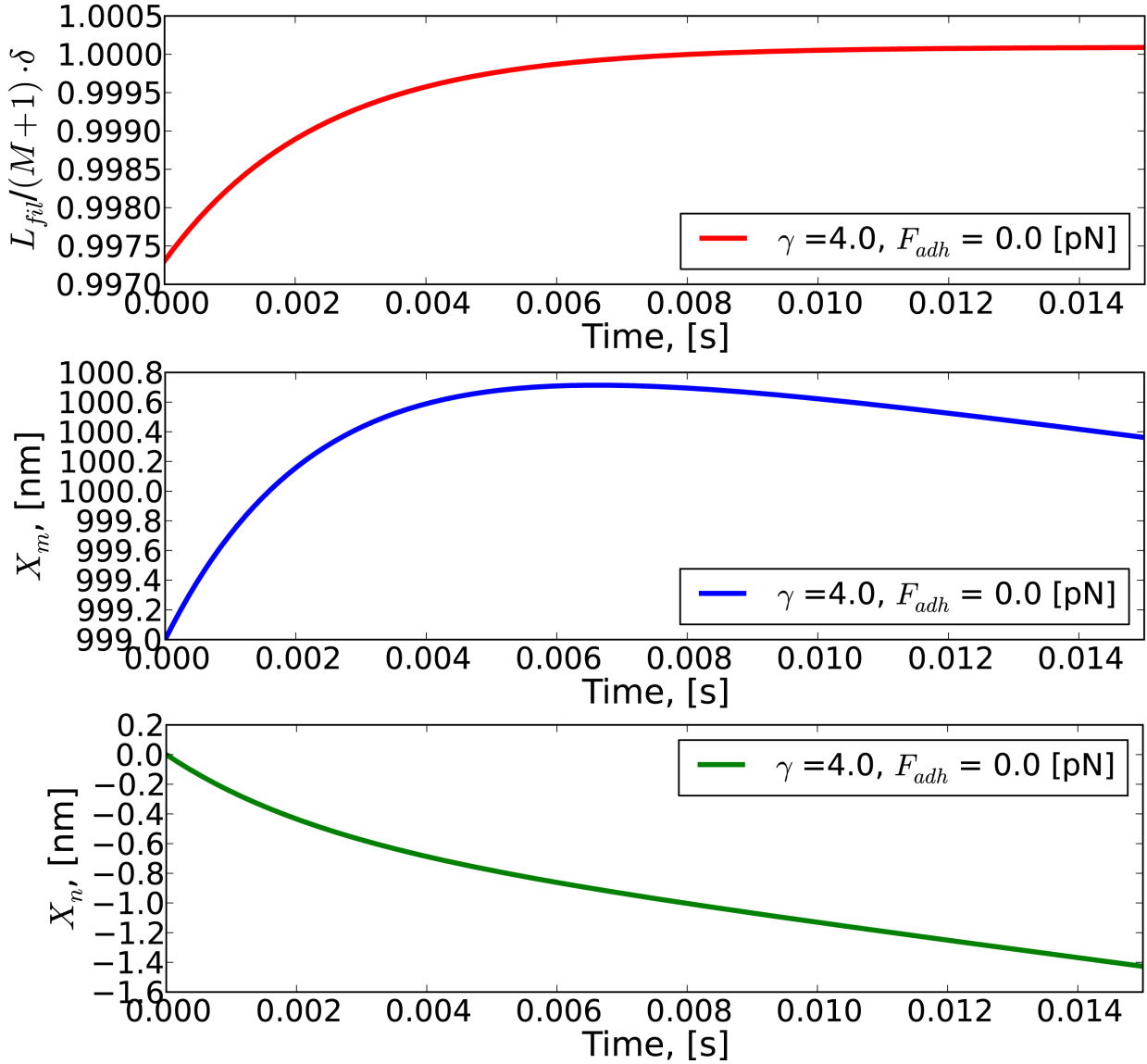


Figure 2.3: Time evolution of the bundle tip and pointed end coordinates: a) normalized filopodial length $L_{fil}(t) = x_m(t) - x_n(t)$; b) filopodial tip coordinate x_m close to the enveloping membrane; c) filopodial base coordinate x_n attached to the lamellipodial network.

2.2.4 Model parameters

The majority of the parameters used in this work is taken from the experimental literature, and the rest is estimated using simple physical considerations. All parameters are shown in the section 2.2.4 with corresponding references.

Friction coefficient ξ_m was estimated using the following logic. Since at steady-state filopodial length is constant, between two consecutive bundle elongations by δ , retrograde flow speed $v_{r,0} = 70$ nm/s should pull filaments back by $\delta = 2.7$ nm (no NAs). Therefore tip coordinate x_m is going to be a periodic function with the same value every $\tau' = \delta/v_{r,0}$ time steps. This condition $x_m(\tau') - x_m(0) = 0$ gives us the equation for ξ_m , shown in Equation 2.5.

$$\lambda_1 \cdot (e^{(\lambda_2 \cdot \frac{1}{\xi_m})} - 1) - \lambda_3 \cdot \frac{1}{\xi_m} = 0, \quad \text{where} \quad (2.5)$$

$$\lambda_1 = \frac{\gamma}{\gamma + 1} \left(\frac{\gamma \cdot f_{mem} - f_{retr}}{k_{bun} \cdot (\gamma + 1)} - \delta \right),$$

$$\lambda_2 = -\frac{\gamma + 1}{\gamma} \cdot k_{bun} \tau,$$

$$\lambda_3 = -\frac{f_{retr} + f_{mem}}{\gamma + 1} \cdot \tau.$$

Solving this nonlinear equation we obtain $\xi_m \simeq 0.379$ (pN· s/ nm) and $\xi_n \simeq 1.52$ (pN· s/ nm), which is in the same range as other reported estimates [10, 38].

2.2.5 Modeling the Nascent Adhesions

Model parameters for the nascent NAs are summarized in section 2.2.4. The NA unbinding rate k_{off} depends on the amount of stress applied on it, according to the "slip bond" model, that is characterized by exponential growth of unbinding rate with a loading force shown in

Table 2.1: Model parameters

Parameter	Value	Reference/Note
Filopodium diameter, d_f	150 [nm]	[14, 33]
Actin monomer size, l_{actin}	2.7 [nm]	[14]
Number of filaments, N	16	[14]
Actin polymerization rate, k_{pol}	11.6 [$1/\mu M \cdot s$]	[14]
Actin depolymerization rate, k_{depol}	1.4 [1/s]	[14]
Membrane friction coefficient, ξ_m	0.0397 [$pN \cdot s/nm$]	*
Friction coefficient ratio, γ	4	
Bundle rigidity, κ_{bun}	128 [pN/nm]	estimated as for a semi-flexible rod similar to [28]
NA spring constant, κ_{adh}	5 [pN/nm]	[10, 34]
Retrograde flow force, f_{retr}	100 [pN]	set to satisfy experimentally measured $v_r \leq 100$ nm/s
Membrane surface tension force, f_{surf}	10 [pN]	[23, 35]
Default retrograde flow speed, $v_{r,0}$	72 nm/s	[14]
NA binding rate, k_{on}	0.09 - 1.8 [$1/\mu M \cdot s$]	[9]
NA unbinding rate (no stress), $k_{off,0}$	0.01 [1/s]	[29]
NA rupture force, F_{rupt}	2 - 17 [pN]	[34, 36]
NA equilibrium spring length, $l_{fa,0}$	30 [nm]	[37]
Total number of NAs (active and inactive)	6	number of activated integrins is often suggested to be small at the filopodial tips
Substrate equilibrium spring length	4.5 [nm]	set so each NA at the tip has enough substrate beads to attach to
Substrate spring constant, κ_{sub}	1-200 [pN/nm]	
Substrate bending constant, $\kappa_{sub,\theta}$	1-200 [pN/rad]	

section 2.2.5 [12, 39].

$$k_{off} = k_{off,0} \cdot \exp\left(\frac{k_{fa} \cdot |l_{fa} - l_{fa,0}|}{F_{rupt}}\right) \quad (2.6)$$

We have varied the typical rupture force F_{rupt} in order to study, how the filopodial dynamics is going to change, if individual NAs become stronger or weaker. Since NAs are thought to form at the tip [13], the question raises, how inactive NAs are transported to the front, after breaking somewhere along the bundle. Moreover, if we allow spontaneous formation of NAs without restricting the overall NA number, the bundle eventually gets "glued" to the substrate even for very low NA binding rate k_{on} , and retrograde flow stalls irreversibly.

It seems reasonable to assume that NAs deactivate after breaking, and new ones are activated at the tip, but the pathways involved and their quantitative characteristics are not fully known to allow the explicit implementation of the NA activation and deactivation processes. Therefore we conserve the total number of NAs (see section 2.2.4) and introduce fast diffusion-like hopping of inactive NAs toward the tip, where they can bind to the filament tips again. The rate of this process should be large enough to avoid artificial delay in NA formation, and we found that rates \geq diffusion rate ($D = 5 \mu m^2/s$) satisfy this condition.

2.2.6 Modeling the cell substrate

The underlying substrate in our setup can be a tissue, a hydrogel, or any gel or solid medium. In our model it is a 2D network of beads connected by springs. Different types of network connectivity can be simulated using our modeling software, that would allow to study the dependence of network elastic moduli on the filopodial dynamics coupled via NAs. The specific stress distribution inside the substrate is not critically important for the filopodial

growth however, and the net elastic force acting on few individual NAs is the factor affecting NA longevity and hence filopodial length through the magnitude of retrograde flow speed v_r . Nevertheless, stress distribution and network topology would become significant for NAs embedded in 3D partitions of the cell, such as lamellipodia and lamella. Here we present the simplest topology, which is a rectangular network without defects. We account to two basic types of deformation: compression/stretching and shear. Harmonic interaction potentials between the connected beads are shown in Equations 2.7:

$$\begin{cases} U_{stretch} = \sum_i \kappa_{sub} \cdot (l_{sub,i} - l_{sub,0})^2, \\ U_{bend} = \sum_j \kappa_{sub,\theta} \cdot \left(\theta_j - \frac{\pi}{2}\right)^2. \end{cases} \quad (2.7)$$

Each bead can be connected to a NA, and we chose the bead density so there are plenty beads available for NA formation. We assume that when a NA forms, it is in a state close to equilibrium with minimum stress applied on it. Therefore in order to find an appropriate bead for NA binding, we assured that the distance between NA attachment on the filament tip and a bead position was $\approx l_{fa,0}$ (see section 2.2.4).

2.3 Results and discussion

Each simulation is a single stochastic trajectory for one specific point in a multidimensional phase space of model parameters, which provides detailed information about various observables on micro-, meso- and macro- length scales. We have access to the microscopic observables, such as NA number, retrograde flow speed at all times, and the substrate network conformation. From those we calculate or measure a number of mesoscopic quantities, such as distributions of the retrograde flow speed and concentrations of chemical species, as well as

distribution of stresses. In addition to that, we measure various macroscopic characteristics for our system, such as lengths of individual filaments, the filopodial length, the speed of growth or retraction, and potential energy of the system. Beside the intricate coupling between these observables for each particular trajectory, our main interest lies in the exploration of how the modulation of mechanical properties or chemical propensities can influence the dynamics of the system.

2.3.1 Retrograde flow dependence on NA binding rate

Cell motility processes, including nascent NAs in filopodia, are undoubtedly dependent on how actively the NAs form. From the simplest mass law considerations, NA number should be a hyperbolic function of the binding constant: $c_{fa} \propto k_{on}/(k_{on} + k_{off})$. It is also straightforward to expect a linear decrease in the retrograde flow speed if the net NA number increases, since $\langle v_r \rangle \propto (f_r + f_m - c_{fa} \cdot \kappa_{fa} \cdot \langle \Delta l_{fa} \rangle) / \xi_n$. Therefore the average retrograde flow should have a hyperbolic form in general as a function of k_{on} . However there is no easy analytical way to predict how this dependence is going to change when individual NAs become stronger.

Figure 2.4a shows a typical probability distribution for the retrograde flow speed v_r for several values of NA rupture force F_{rupt} . It clearly demonstrates that the distribution shifts dramatically toward lower v_r when F_{rupt} raises, including bimodal phase as well. We use these distributions to compute the average $\langle v_r \rangle$ along with the standard deviations in order to denote the amount of fluctuations. Figure 2.4b shows the $\langle v_r \rangle$ dependence on NA binding rate k_{on} for several F_{rupt} . Let's note that the forms of all curves look hyperbolic, however the magnitude is very different. For weak NAs characterized by low values of F_{rupt} retrograde flow does not significantly depend on the formation probability, and so it does for very strong NAs. The strongest sensitivity to k_{on} is exhibited in the medium range of F_{rupt} values, which is an interesting result.

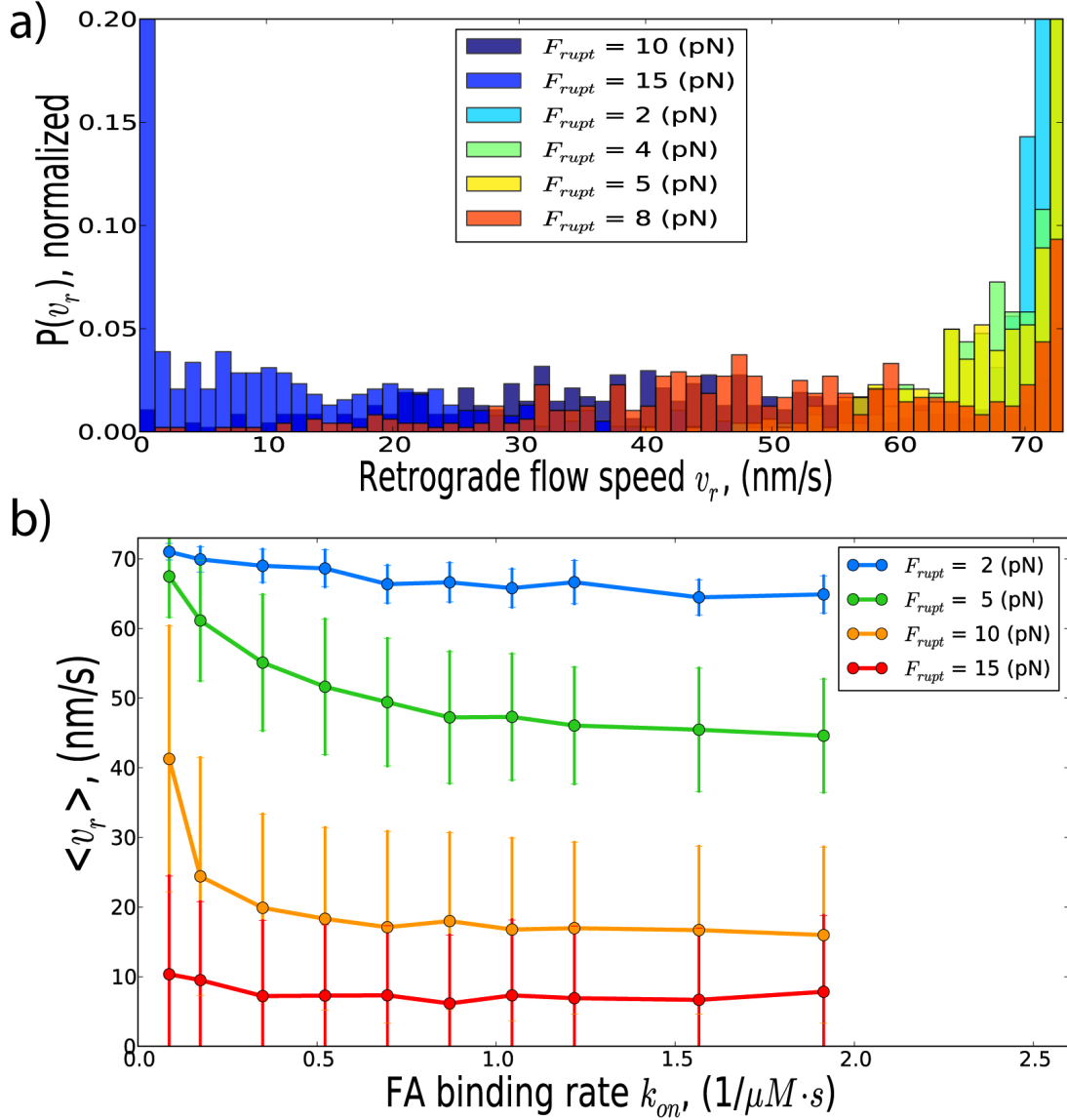


Figure 2.4: Retrograde flow speed v_r dependence on NA binding rate k_{on} : a) Probability distributions $P(v_r)$ shown for several values of NA strength, characterized by the typical rupture force F_{rupt} . Note significant shift of $\max(P(v_r))$ toward smaller v_r , when individual NAs become stronger (larger F_{rupt}). b) Average values of v_r shown with corresponding standard deviations as a function of the NA binding rate k_{on} . $\langle v_r \rangle$ decreases with rising NA binding constant k_{on} . However this dependence is mild for weak and strong NAs (see $F_{rupt}=2, 15$ pN), and it is more pronounced for medium range of F_{rupt} . Note the magnitude of fluctuations raises when individual NA become stronger (error bars from top to bottom).

If NA formation is a rare event, one should anticipate increased fluctuations in their number and the retrograde flow speed v_r consequently. This trend can be clearly seen in Figure 2.4b, if we follow as the error bar size changes from top to the bottom curves. It is an intriguing question, what is more beneficial: to have fewer, but stronger NAs, that produce large discrete noise in the system dynamics, or larger number of weaker NAs introducing less noise in the retrograde flow speed and possibly the length fluctuations as well.

2.3.2 Retrograde flow dependence on NA rupture force

Since the individual NA strength introduced via NA rupture force F_{rupt} showed to be an important factor defining the dynamics in the system, we have sampled a physically plausible range of F_{rupt} .

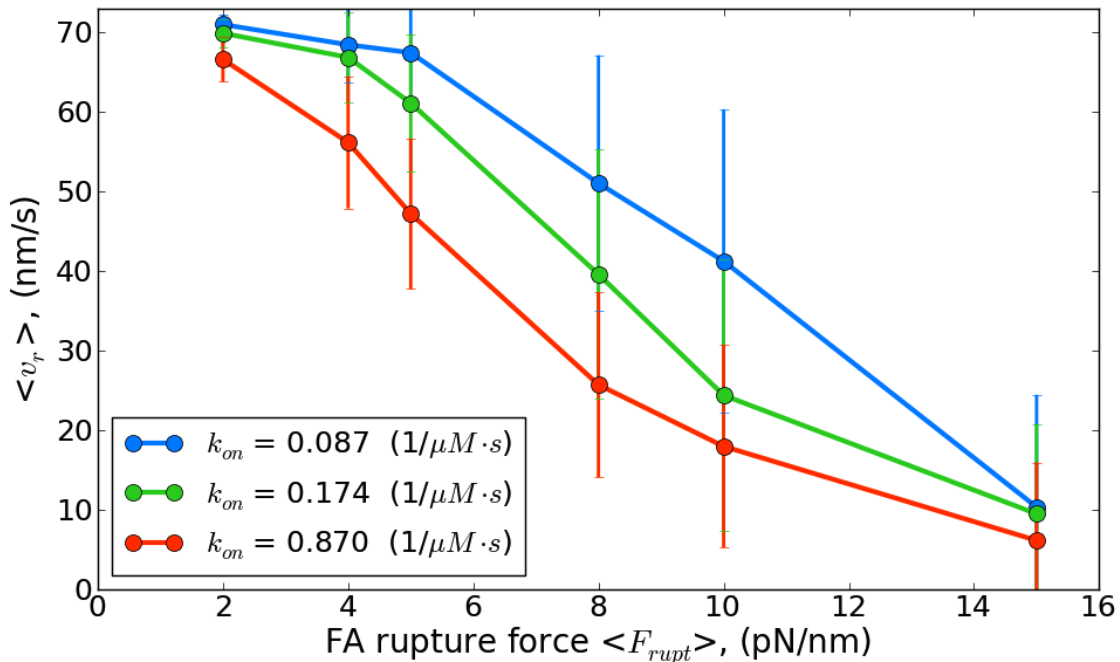


Figure 2.5: Retrograde flow speed v_r dependence on NA rupture force F_{rupt} : Average values of v_r shown with corresponding standard deviations as a function of the NA binding rate F_{rupt} , shown for several values of the NA binding constant k_{on} . $\langle v_r \rangle$ decreases dramatically with rising strength of individual NAs.

The results are shown in Figure 2.5 for several binding constants k_{on} . Both decrease of $\langle v_r \rangle$ and raise of fluctuations can be clearly seen from this picture, as well as the fact, that k_{on} does not define the value of v_r as much as F_{rupt} does, but it affects how quickly v_r decays with the increase in NA strength. It should be mentioned that the error bars in Figure 2.5 can include not only the widely spread v_r probability distributions, but also bimodal distributions of v_r , one example of which can be seen in Figure 2.4a. Such bimodal distributions would produce large standard deviations for the mean $\langle v_r \rangle$. The presence of bimodal probability distributions for v_r is an indirect evidence for oscillatory regimes, and is going to be discussed in more detail below.

2.3.3 Retrograde flow dependence on substrate stiffness

Now let's look at how retrograde flow speed v_r depends on the rigidity of the substrate. If we gradually move in the parameter phase space toward higher values of $\{\kappa_{sub}, \kappa_{sub,\theta}\}$ we can see that not only the average $\langle v_r \rangle$ shifts toward higher values, but also the change in how $\langle v_r \rangle$ and L_{max} (maximum filopodial length achieved during 100 s simulation) depend on the model parameters. To promptly correct for the general shift in $\langle v_r \rangle$, we have divided measured $\langle v_r \rangle$ by $\langle v_{r,\infty} \rangle$ on an infinitely stiff substrate, which in our model would be the stiffest substrate simulated $\{\kappa_{sub} = 50 \cdot \kappa_{fa}, \kappa_{sub,\theta} = 50 \cdot \kappa_{fa}\}$, when all other kinetic and mechanical parameters are fixed. The similar normalization was done to the maximum reached filopodial length L_{max} . The dependence of these normalized values is shown in Figure 2.6.

In previously reported models [9, 10] it was shown that dynamic response of the system should be highly sensitive to the substrate rigidity, and retrograde flow speed $\langle v_r \rangle$ should rise with the substrate stiffness. It can be seen in Figure 2.6a that v_r does have a general tendency to increase along with the substrate stiffness, however this dependence is close to negligible for weak NAs and is highly affected by noise for strong NAs. The most sensitive response of

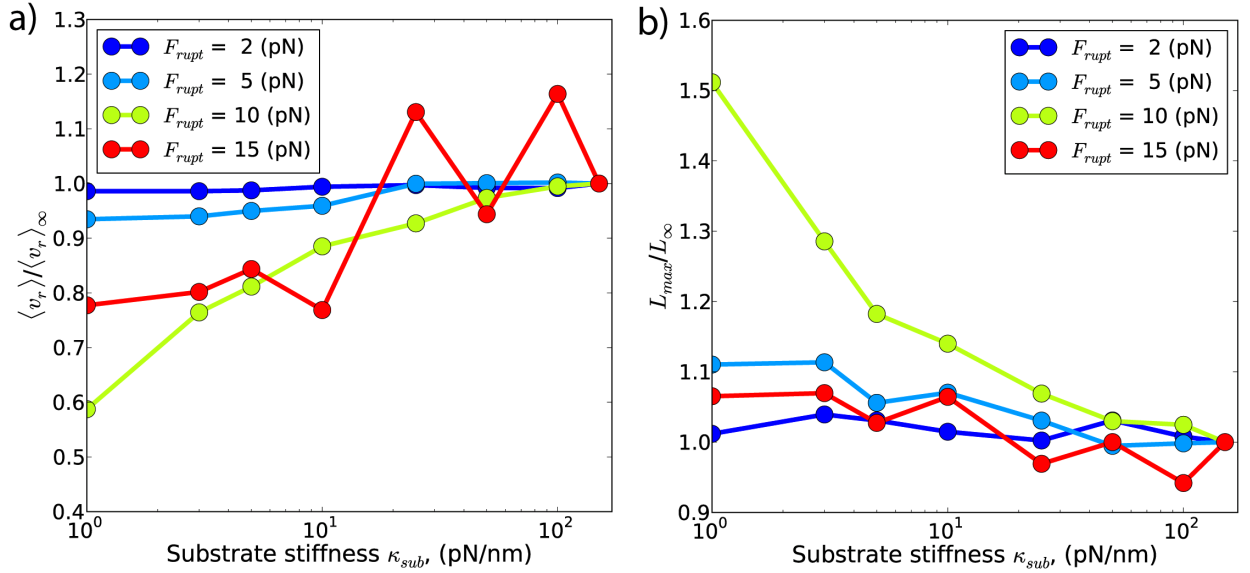


Figure 2.6: a) Retrograde flow speed v_r dependence on substrate stiffness κ_{sub} . The measured values of v_r were normalized to the ones on the stiffest substrate simulated, which is a numeric approximation for the asymptotic value $v_{r,\infty}$ on an infinitely rigid substrate; b) Maximum reached filopodial length L_{max} as a function of substrate stiffness κ_{sub} , normalized in similar manner as v_r . We do not show the error bars on these dependences for the sake of clarity of the picture, Note that fluctuations in the measured v_r for large F_{rupt} values were significantly high. In such cases different trajectories can be in different states by the end of the simulation, and large ensembles should be simulated for each point in order to obtain smooth dependences for v_r and L_{max} . All simulations were made for the low NA binding rate $k_{on}=0.174$ $1/\mu M \cdot s$.

filopodial system lies in the medium values of F_{rupt} and intensifies if NA formation becomes a rate event. Unfortunately, at the same time as k_{on} decreases the noise in the v_r increases dramatically and affects the smoothness of the tendencies shown in Figure 2.6. The maximum length L_{max} which filopodium can grow up to within first 100 s is also sensitive to substrate stiffness in the same region of the parameter phase space as v_r . This similarity in dynamic response can be rationalized by using the mean-field model of filopodial growth developed in [14]. No impact from NA is considered in that model, but luckily it depends only on the actin involved kinetic processes, which NAs do not affect in a direct way. By modulating v_r the the original model we can still use the functional dependence of steady-state filopodial length on v_r , shown in ??.

$$L = \frac{\pi R^2 D^2}{N} \cdot \left(\frac{\delta}{v_r} \left(c_{a,0} - \frac{k^-}{k_+} \right) - \frac{1}{k_+} \right). \quad (2.8)$$

Therefore, as the first order approximation L_{max} should depend on v_r in a hyperbolic manner, which qualitatively agrees with the trends demonstrated in Figure 2.6.

It is important to notice that the sensitivity of the filopodium system to the substrate stiffness is not a general property, but rather raises in a confined region of parameter phase space, which differs our model from the previous efforts [9, 10]. In addition to that, our model clearly shows the importance of noise in this system, which can dramatically affect the output of the simulation and should create a significant variation among an ensemble of filopodia.

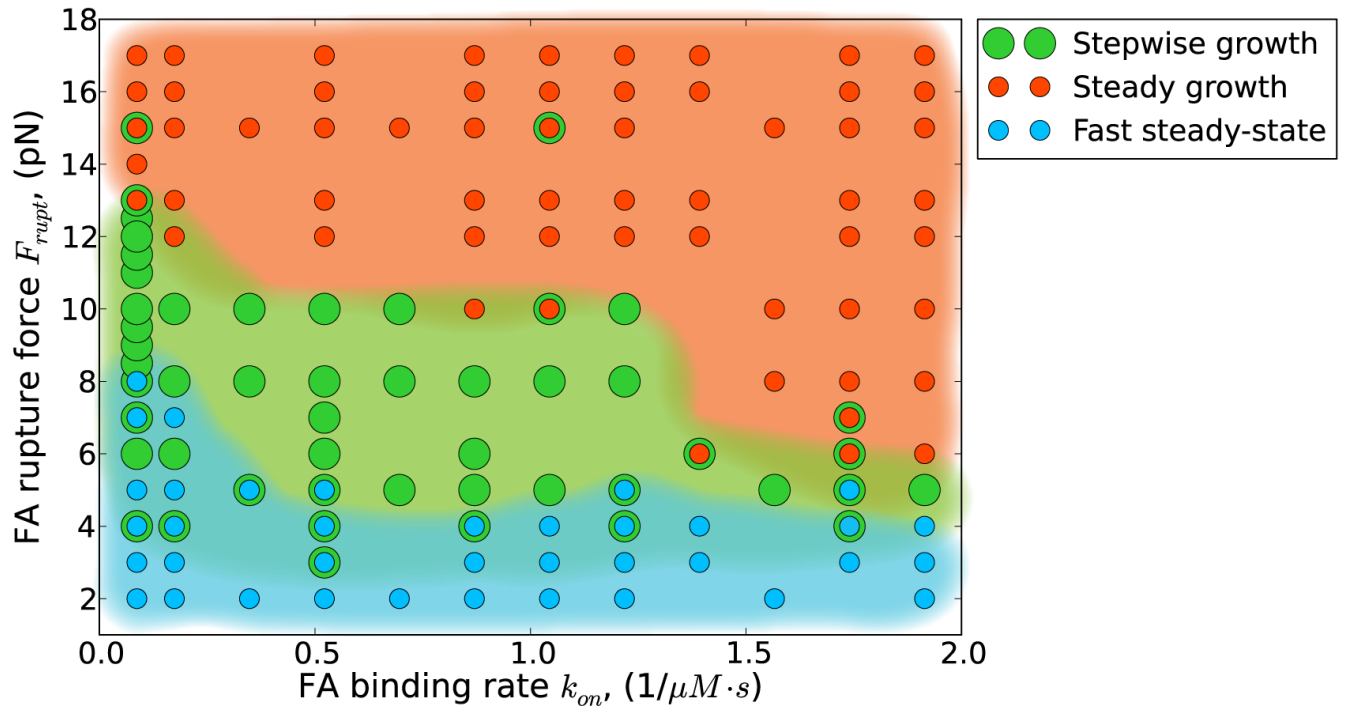


Figure 2.7: Diagram of filopodial dynamic states as a function of F_{rupt} and k_{on} on a soft substrate. At low F_{rupt} and wide range of k_{on} a filopodium quickly reaches its steady-state (colored in blue). At intermediate F_{rupt} and a wide range of values of k_{on} a new stepwise growth pattern emerges (colored in green). For large values of F_{rupt} and various k_{on} the stepwise grows smooths out to be a steady growth and low fluctuations, despite the fact that v_r fluctuations rise tremendously.

2.3.4 Different regimes in growth dynamics: what causes oscillations and stepwise growth

Moving up to the macro-scale observable in our simulations, the length of the filopodium as a whole, we can see a variety of dynamic regimes, exhibited by the system (see Figure 2.7).

The softer is the substrate the more likely we are to find a special growth regime, which we are going to call as "stepwise growth" in this manuscript. It is colored in green on our diagram of states and is often referred to as "stick-slip" behavior. This regime also includes oscillating steady-state in the narrow region of low binding constant k_{on} and medium-large rupture forces F_{rupt} . It should be mentioned that we have not observed the stepwise growth regime on stiff substrates.

Stepwise growth (green region in Figure 2.7) slowly emerges from the NAs steady-state regime (blue region in Figure 2.7), sometimes through a special case of oscillating steady state (for very low k_{on} values), when F_{rupt} raises. For even larger values of F_{rupt} stepwise growth regime smoothly morphs into a NA enhanced steady filopodial growth (orange region in Figure 2.7).

We have not observed any sharp boundaries between the dynamic regimes, and they smoothly transition one to another, and it is a nontrivial problem to mark the regimes in the transition regions of the state diagram, which is highlighted by different colors displayed on top of each other in the diagram. As an example of typical dynamics regimes, let us consider a few representative trajectories, shown in Figure 2.8. In case of very strong NAs (red curve) we characterize this type of growth as steady, enhanced due to the presence of NAs. However one can easily see residual step structure that is however much less notable, that for the cases of $F_{rupt} = 9, 12$ pN.

Indeed, if there is no well defined order parameter in the system that would exhibit a jump, the process of distinguishing different states becomes a challenging task. Our separation be-

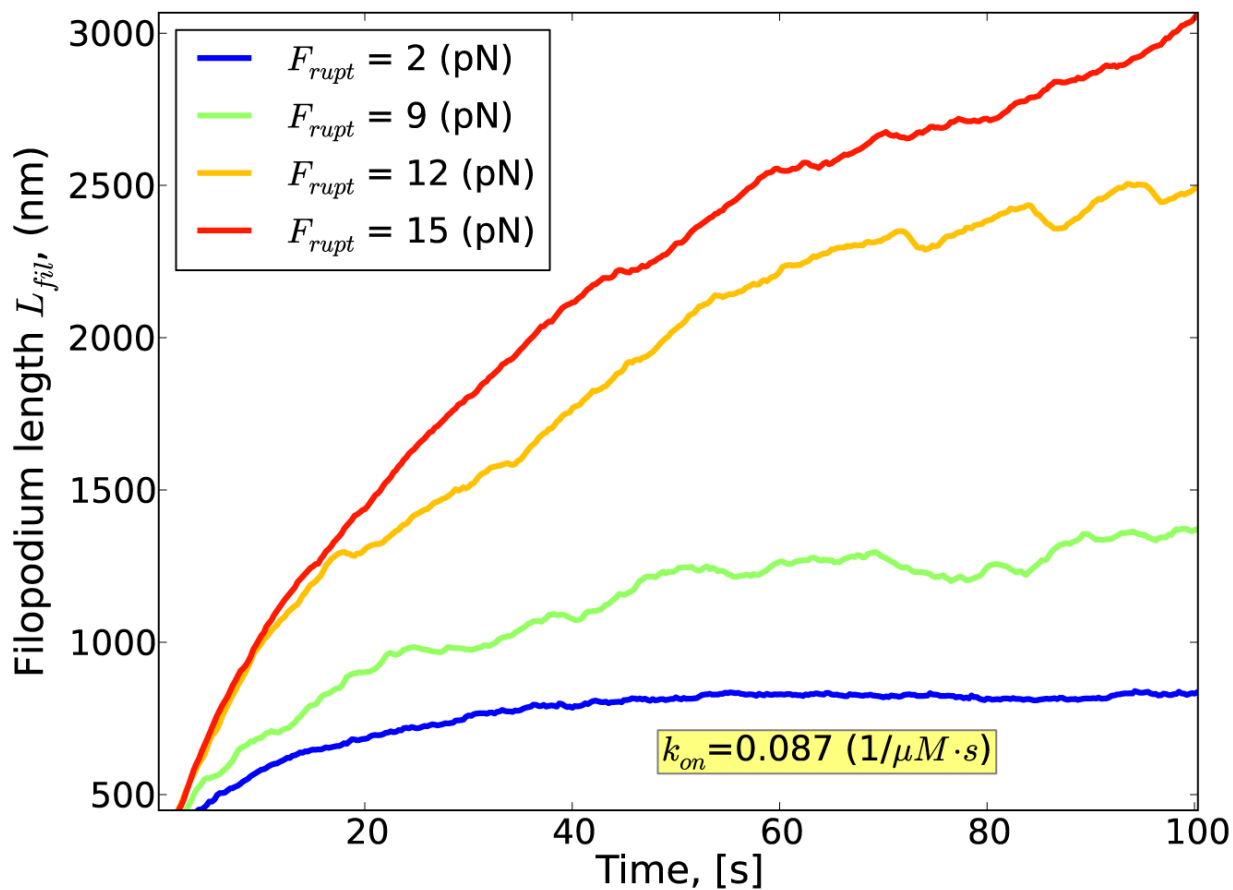


Figure 2.8: Examples of various dynamic regimes in the filopodial system on a soft substrate for several rupture forces F_{rupt} . All curves show filopodial length evolution with time and illustrate NAst steady-state regime (blue curve), an oscillating steady-state (green curve), an stepwise growth (orange curve), and steady Fa enhanced growth (red curve).

tween oscillating and non-oscillating steady state, as well as stepwise versus enhanced growth was based on the quantitative condition that steps or oscillations in a time period Δt should be much larger than the length fluctuations in the pure actin system without NA and have a magnitude of at least 10% of the length $\langle L \rangle_{\Delta t}$. The majority of time this condition corresponds to length fluctuations ≥ 100 nm.

Another fundamentally important result is the non-trivial self-averaging of fluctuations in the filopodial system. Note, that for strong NAs, i.e. large values of F_{rupt} , retrograde flow speed exhibits significantly large fluctuations, which are sometimes on the order of the value $\langle v_r \rangle$ itself (see Figure 2.5). However, if we look at the filopodial length, our macroscopic observable, it has minor fluctuations for large F_{rupt} and is exhibiting stepwise behavior only for very low k_{on} values. Therefore the high level of micro- and mesoscopic fluctuations may not directly translate onto the macroscopic fluctuations, when there are several sources of microscopic noise.

2.4 Conclusions

We have developed a self-consistent stochastic model for filopodial dynamics that integrates a number of mechanical properties and an extracellular substrate. This model has a complex multi-component nature, similar in structure to [9], but does not contain additional phenomenological relations or synergistic connections between variables. We employed the approach that is similar to [10] with explicit energy minimization and force balance calculation. Furthermore, we describe the system of interest on much greater level of detail that reported in [9, 10], and couple mechanic response with discrete stochastic chemical reactions. This model allowed us to explore and uncover a variety of dynamic behaviors of the filopodial system in a multidimensional phase space of model parameters. Our method allows not only tracing the general dependences of the observable averages, but provides full information about

their probability distributions and their coupling.

We have shown that retrograde flow modulation is strongly affected by individual mechanical NA properties and less by the kinetic rates. Also there are regions in the phase space of parameters where fluctuations raising in the system can not be ignored, and the ensemble averages should be considered rather than time averages for active growth and retraction processes. That is, if maximum or steady-state values of $\langle v_r \rangle$ or $\langle L \rangle$ are of main interest, filopodial systems can show significant deviations from sample to sample.

However when the main interest lies in how that steady-state is achieved (with oscillations or not), there can be a significant noise reduction between meso- and macroscopic variables in the system. Such noise self-averaging leads to a more homogeneous type (regime) of dynamic behavior for a particular set of system parameters. Note that not only the number of NAs and thus retrograde flow are stochastic variables, but the polymerization kinetics are sources of discrete noise as well. This brings us to an important conclusion. When all sources of stochastic noise are considered, previously reported synergetic response [9] may easily disappear due to the self-averaging of fluctuations.

It appears that intermediate values of NA strength and binding rate are the most beneficial for the unusual stepwise growth, and that regime is present on soft substrates, while on stiffer substrates we can treat our system as one with pure actin and just rescale the retrograde pulling force to a lower value due to the presence of NAs.

Chapter 3

Theory of Active Transport in Filopodia and Stereocilia *

3.1 Introduction

Molecular motor transport in a living cell is one of the most fascinating processes in cellular biophysics. Molecular motors play crucial roles in many elongated organelles, such as neuronal axons [40], flagella [41], filopodia [42], stereocilia [43,44] and microvilli [43]. A naive view of cellular motor transport is that of motor molecules orderly following each other on the substrate and carrying cargo, which they unload at a destination point. However, in reality motors not only walk, but also diffuse around the cell, randomly binding and unbinding to their substrate filaments and/or cargo. To a large extent these processes are governed by molecular noise. To understand how the motors perform their functions – be it cargo delivery to the growing end of an organelle or creating stresses in a flagellum, or even in artificial systems [45, 46] – it is necessary to know their spatial distribution in these systems.

The spatial distribution of the motors could influence the delivery of building material towards the growing end of a dynamic elongated organelle, such as a filopodium or a stereocilium. In the absence of motors, the length of such organelle is expected to be limited by the slow diffusional delivery of the material to the tip [47]. Furthermore, prior computational modeling of simple, conveyor-belt-like transport of monomeric species by molecular motors indicated

*Maria Minakova, Pavel I. Zhuravlev, Yueheng Lan , Garegin A. Papoian

that specially designed cooperative mechanisms are needed to achieve any appreciable active transport flux [48]. Two main reasons for the transport inefficiency are sequestration of cargo by motors and diminution of motor speeds due to clogging of the filamentous bundle by walking motors [48]. These “traffic jams” may also be inferred from the corresponding spatial distributions of motors, as discussed below. Another intriguing experimental observation is the localization of the myosin motors at the tips of filopodia [42] and stereocilia [44]. All of these findings provide sufficient motivation to look deeper into the spatial distributions of motors and their cargo in actin based protrusions, and, in particular, to better understand the physical mechanisms which control the delivery of the building materials to the protrusion tips.

The goal of the current work is to find the stationary distributions of motors and their respective G-actin cargo inside cellular protrusions, such as filopodia or stereocilia. We also investigate the way these distributions ultimately regulate the lengths of the corresponding protrusions. In stereocilia, for example, fine regulation of length is important and is clearly coupled to function [49]. One expects the lengths of filopodia to also be controlled by cell’s mechanochemical machinery, as seen, for example, in very long filopodia in sea urchin cells [50]. Prior calculations showed that diffusional transport is unlikely to provide sufficient G-actin flux to produce such long filopodia [47, 48]. In our detailed computational models of motor and G-actin transport in filopodia and stereocilia, the main processes that determine the spatial distributions of motors are: 1) directed walking of bound motors on the filaments driven by ATP hydrolysis; 2) diffusion of free motors in the cytosol, and 3) the chemical exchange between the bound and free motors. In this work, we have developed an analytical mean-field theory to obtain the stationary concentrations of bound and free motors. It turns out, that the mean-field equations for motor profiles are highly non-linear and cannot be solved numerically using most common approaches, requiring instead a special phase portrait analysis to construct the solution. The resulting motor distributions are in quantitative agreement with our detailed stochastic simulations of growing filopodia and in qualitative agreement with experimental

data for Myosin IIIa in stereocilia and filopodia [44]. Furthermore, since the motor proteins may carry cargo such as G-actins, we also derived the corresponding mean-field equations for the G-actin stationary dynamics. Since G-actin's availability at the protrusion tip determines the corresponding speed of polymerization, the motor driven G-actin transport may critically influence and, hence, regulate the steady state lengths of filopodia or stereocilia.

Surprisingly, our mean-field equations indicate that there exists a universal stationary motor profile, which does not depend on the protrusion length and is robust with respect to model parameters or even nature of the elongated enclosed cylindrical environment. We provide a simple explanation for the observed universality of motor concentration profiles. Furthermore, detailed stochastic simulations show that the G-actin concentration profile in filopodium to be non-monotonic, with a minimum, followed by a maximum, which is an interesting, non-trivial result [51]. Using our mean-field analyses, we suggest a physical explanation that gives rise to the observed non-monotonic G-actin distributions. Finally, the stationary motor and cargo distributions may be kinetically difficult to reach for longer filopodia or stereocilia, hence, in the end we discuss the issue of sensitivity to the initial conditions.

3.2 Methods

3.2.1 Model parameters

We employ the following computational setup (Fig. ??). There are $N = 16$ actin filaments in the cylindrical filopodial tube with radius $R = 75$ nm) [52]. There are two protofilaments in each filament, so we use half a monomer size $\delta = 2.7$ nm. These values yield a concentration of F-actin monomers in a filopodium $c_s = N/\pi R^2 \delta \approx 560 \mu\text{M}$. G-actin is diffusing along the filopodium ($D = 5 \mu\text{m}^2/\text{s}$) [53] while its concentration at the filopodial base is maintained by the cell at a constant bulk level $a(0) = 10 \mu\text{M}$ [48, 54, 55]. At the tip, G-actin monomers can react with the N barbed ends with the rate $k^+ = 11.6 \mu\text{M}^{-1}\text{s}^{-1}$ and depolymerize with

rate $k^- = 1.4 \text{ s}^{-1}$ [55]. Retrograde flow moves the filaments backwards with a constant speed $v_r = 70 \text{ nm/s}$ [56]. Myosin motors also diffuse along the filopodium ($D = 5 \mu\text{m}^2/\text{s}$), but in addition they can bind to a filament with the rate k_{on} (for all the binding and on-rates we use the diffusion-limited value of $10 \mu\text{M}^{-1}\text{s}^{-1}$), unbind with the rate k_{off} ($10 - 100 \text{ s}^{-1}$) and perform forward and back steps on filaments with the rates $k_{\rightarrow} = 50 \text{ s}^{-1}$ and $k_{\leftarrow} = 5 \text{ s}^{-1}$. In the continuous analytical model these rates translate into $v = (k_{\rightarrow} - k_{\leftarrow})l_{\text{ss}} \approx 1400 \text{ nm/s}$ (with motor step size $l_{\text{ss}} = 32.4 \text{ nm}$). If a motor is bound to a filament, it can also load actin with the rate $k_l = 10 \mu\text{M}^{-1}\text{s}^{-1}$ and unload it with the rate k_{ul} ($10 - 30 \text{ s}^{-1}$). To prevent sequestration, when a loaded motor unbinds from a filament, it simultaneously releases its G-actin cargo. Motors cannot step on or bind to an F-actin monomer unit occupied by another motor. Like with G-actin, the unbound motors concentration at the base $c_f(0)$ was kept constant at the bulk value ($0.1 - 1 \mu\text{M}$).

3.2.2 Stochastic simulations

Polymerization, depolymerization, motor stepping, binding and unbinding, actin loading and unloading and diffusion are treated like chemical reactions with set rates, based on the algorithms elaborated in our prior works [47, 48, 51].

3.2.3 Retrograde flow

The retrograde flow plays an important role in setting up the stationary length, as it defines the actin flux through the filopodial cross-section (or, rather two equal fluxes with opposite signs). In the model reported in this work, we use a constant retrograde flow speed, which depends neither on polymerization, nor on various protein concentrations. In reality, the retrograde flow rate can be influenced by many factors both in the cell bulk (active machinery pulling filaments back; rearrangements and filament degradation in lamellipodia) or in filopodia itself, like focal adhesions [57], or force from the membrane acting on a filament which is

polymerizing against it. We investigated the coupling between the retrograde flow and polymerization in our previous work (reported in the Appendix A) [48]. This coupling can be easily taken into account in the mean-field sense, where the results are in close agreement with more detailed stochastic simulations that allow for the retrograde flow fluctuations. In this work we focused on the phenomena brought in by molecular motors inside the filopodium, and, hence, chose in favor of a simpler model where the retrograde flow is simply held constant and does not depend on other parameters and processes. This assumption can be released in a straightforward manner, if needed.

3.2.4 The boundary conditions

The choice of the third boundary condition for the equations describing the motor profiles is a subtle issue and depends on the particular question one has in mind. This choice only has a slight effect on the solution of the equations, so it is not very important. However, it is worthwhile to discuss it for clarity purposes.

For the purely mathematical, continuous problem, where the filaments don't exist outside the tube, the appropriate boundary condition is $c_b(0) = 0$ (from which follows the $A(0) = 0$ in the actin part) and no additional assumptions (like detailed balance) are required. Indeed, if the filaments do not cross the $z = 0$ point, neither can bound motors, hence $J_b(0) = 0$, and as $J_b = v(c_b)c_b$, $c_b(0) = 0$. This argument can be presented in a more detailed way. Let us consider a small (going to infinitesimal later) volume of the tube near the base. Integrating the second of the motor equations over this volume one gets:

$$\frac{\partial J_b}{\partial z} = -k_{\text{off}}c_b + k_{\text{on}}c_f, \quad (3.1)$$

$$\int_0^{\delta z} \frac{\partial J_b}{\partial z} dx dy dz = \int_0^{\delta z} (-k_{\text{off}}c_b + k_{\text{on}}c_f) dx dy dz, \quad (3.2)$$

$$(J_b(0 + \delta z) - J_b(0+))S_f = (-k_{\text{off}}c_b(\alpha\delta z) + k_{\text{on}}c_f(\alpha\delta z))S_f\delta z, \quad (3.3)$$

where S_f is cross-section of the filopodium and $0 \leq \alpha \leq 1$.

Since $J_b(0+) = 0$,

$$J_b(0 + \delta z)S_f = (-k_{\text{off}}c_b(\alpha\delta z) + k_{\text{on}}c_f(\alpha\delta z))S_f\delta z, \quad (3.4)$$

$$\lim_{\delta z \rightarrow 0} J_b(\delta z) = \lim_{\delta z \rightarrow 0} (-k_{\text{off}}c_b(\alpha\delta z) + k_{\text{on}}c_f(\alpha\delta z))\delta z = 0, \quad (3.5)$$

and as $J_b = v(c_b)c_b$, one can conclude that $\lim_{\delta z \rightarrow 0} c_b(\delta z) = 0$ and use the boundary condition

$$c_b(0) = 0. \quad (3.6)$$

In our simulations, however, the space is split into compartments, and the concentration profiles are not continuous, and the first point corresponds to the first compartment, which spans 54 nm starting from $z = 0$. It is not obvious how to directly compare the simulation results with continuous analytical curves at $z = 0$. To compare one should take average of the analytical curve over the first 54 nm and using it as $c_b(0)$ and solve the equations again. Alternatively, one can assume detailed balance between c_f and c_b at $z = 0$ (and between c_b and A in the actin equations), which turns out to be a good approximation.

In real filopodia the filaments continue into the cell bulk (unlike our simulations), making the $c_b = 0$ condition of the formal problem less relevant. Detailed balance in the cell bulk, on the other hand, is a plausible assumption as a first approximation. The next approximation would require modeling of the filaments with motors in the bulk (the lamellipodium) explicitly.

Thus, the detailed balance BCs are more interesting and relevant for the physical problem, so they are the ones used in the paper. However, it turns out that both alternative BCs lead to almost indistinguishable results, except for the very beginning of the concentration profiles.

To demonstrate this, we plotted below the graphs corresponding to the solution of the formal mathematical problem, with no additional assumptions, and the $c_b(0) = 0$ boundary condition (Figs. 3.2-3.6).

3.3 Results and discussion

This section is organized in two parts: the “motor” part and the “actin” part. In the “motor” part, we present three increasingly realistic mean-field models of motor stationary profile along the tube. By gradually adding complexity we reproduce the results of the stochastic simulations of growing filopodia with Gillespie algorithm, which is the most comprehensive representation of the complex system dynamics in our work, and thus serves as a check for our mean-field model. Since the resulting motor distribution does not depend on the filopodial length, we use it in the “actin” part to find the G-actin flux due to active transport, the G-actin concentration profile and the stationary filopodial length set up by the balance of actin fluxes.

Structurally, a filopodium is a bundle of 10 – 30 actin filaments enveloped by the cell’s plasma membrane (Fig.3.1). Filaments are growing at the filopodial tip consuming G-actin monomers [58] delivered from the bulk of the cell by diffusion and possibly motor transport [48]. The filaments are pulled back into the cell bulk by special mechanisms inside the cell, in addition, the barbed ends at the tip are pushed by membrane elastic resistance, resulting in a gradual motion of the filaments backwards known as retrograde flow [56]. We do not include other regulatory proteins or filament elasticity into the baseline scenario for motor distribution and filopodial growth.

3.3.1 Motor distributions

In the “motor” part of the problem, we consider a cylindrical tube with two types of motors – free and bound – that are subject to two different mechanisms of transport – diffusional and

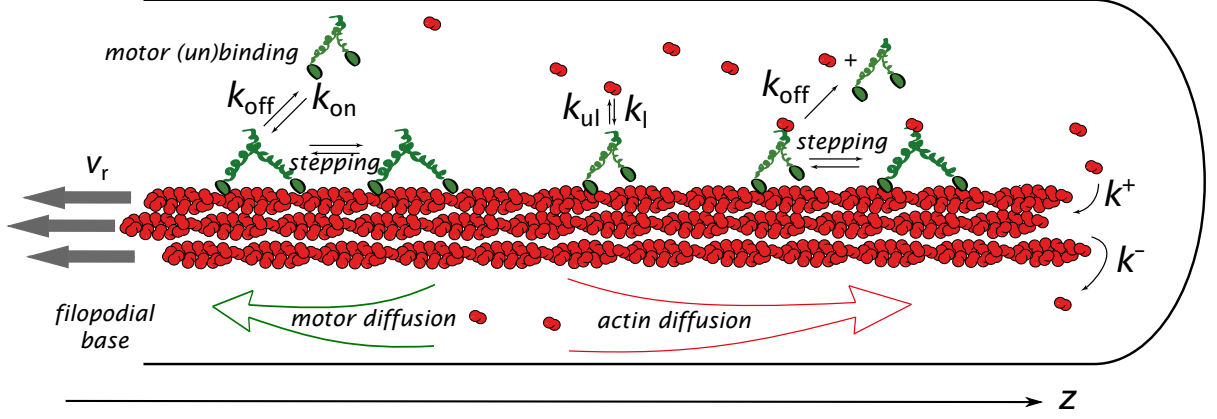


Figure 3.1: A representation of the filopodial model is shown with kinetics scheme of chemical reactions. A filopodium is a cylindrical tube with a bundle of parallel actin filaments inside enveloped by cell's membrane. The motors can walk on filaments (with speed v determined by forward and backward stepping rates) or diffuse in the solution (with diffusion constant of $5 \mu\text{m}^2/\text{s}$). They can bind and unbind to the filaments (with rates k_{on} and k_{off}) and, when on filaments, load and unload G-actin (with rates k_l and k_{ul}). A loaded motor can detach from the filament simultaneously releasing G-actin. Thus, there is no G-actin bound to motors in the solution, fulfilling the non-sequestering regime condition.

active – respectively. The problem is, therefore, one-dimensional, and we introduce concentrations of free and bound motors, $c_f(z)$ and $c_b(z)$ and write the continuity equations [59]:

$$\frac{\partial c_f}{\partial t} + \frac{\partial J_f}{\partial z} = k_{\text{off}}c_b - k_{\text{on}}c_f = - \left(\frac{\partial c_b}{\partial t} + \frac{\partial J_b}{\partial z} \right), \quad (3.7)$$

where $J_f(z)$ and $J_b(z)$ are forward fluxes for free and bound motors respectively, and k_{off} is the unbinding rate of a motor from a site on a filament. For the rate constant of binding between a motor molecule and an F-actin monomer unit, we use the diffusion-limited rate constant, $k_{\text{on}}^{\text{dl}} = 10 \mu\text{M}^{-1}\text{s}^{-1}$, which translates into $k_{\text{on}} = k_{\text{on}}^{\text{dl}}c_s$ rate for a motor to bind to any monomer unit, c_s being the concentration of F-actin monomer units, which are the binding sites, inside the filopodium. To calculate c_s we count F-actin monomer units in the filopodial volume 1 monomer unit thick, yielding $c_s = N/S\delta$, where N is number of filaments, δ is monomer half-size, and S is filopodial cross-section. Fick's law defines $J_f(z) = -D\partial_z c_f$. We assume there

are plenty of motors in the cell bulk, which sets a fixed $c_f(0)$ as a BC at the filopodial base. We can also assume that there is detailed balance between free and bound motors in the cell bulk, and, therefore, at the base, and obtain the third BC, $k_{\text{on}}c_f(0) = k_{\text{off}}c_b(0)$. Interestingly, an alternative BC may be adopted without relying on this assumption in case when filaments cease to exist outside of the tube and when comparison with discrete stochastic simulation results is not needed. This BC, which turns out to be $c_b(0) = 0$, is elaborated in the Appendix A, where it is also shown that the choice between the two alternative BCs leads to almost identical results. For the stationary solution of Eq.3.7, the total motor flux through a cross-section, corresponding to the integral, $J_f + J_b = \text{const}$, turns out to be zero, $J_f + J_b = 0$, because of the reflecting BC at the tip. Interestingly, this is the only time the filopodial tip enters the solution for the motors, and it does not introduce the filopodial length as a parameter. Consequently, the stationary motor concentration profiles do not depend on the length. Such universality of motor profile is robust, because it will be also present in other elongated organelles and enclosed cylindrical environments, as long as the system is governed by diffusion and directed random walk, yielding equations of the form Eq.3.7 with these BCs. This is a surprising and important result.

3.3.2 Phantom motors model failure

The simplest expression for the bound motor flux is $J_b = (v - v_r)c_b$, where v is average motor speed generated by ATP hydrolysis steps, and v_r is the retrograde flow speed. Now we have a closed system of equations for the concentrations with stationary solution defined by $Dc_f''(z) = -k_{\text{on}}c_f(z) + k_{\text{off}}c_b(z) = (v - v_r)c_b'(z)$. This linear set of homogenous ODE (phantom motors model, or PMM) has been solved analytically (but with different BCs) to find a motor concentration profile in a stereocilium [59]. Our BCs yield an exponential growth of both free and bound motor concentrations towards the tip of a filopodium (dashed lines on Fig.3.2). The PMM solution strongly disagrees with the stochastic simulations of the same

system. The reason for the failure is that in the PMM motors do not interact with each other and can bind onto filaments unlimitedly, regardless of the finite number of binding sites. In reality, $c_b(z)$ is capped by the concentration of binding sites, which in our simulations equals F-actin monomer unit concentration c_s .

3.3.3 Finite filament capacity

In order to account for the saturation of binding sites, one has to make $k_{\text{on}} = k_{\text{on}}^{\text{dl}}(c_s - c_b) = k_{\text{on}}^0(1 - c_b/c_s)$ dependent on the number of available binding sites [60]. The mean-field equations (FFC) become non-linear and can be solved numerically. The results are in a much better agreement with the stochastic simulations (solid lines in Fig.3.2). Still, the discrepancies are rather notable, especially, for the concentration of free motors (Fig.3.2 (inset)).

3.3.4 Jammed motors

To improve the accuracy of the mean-field model, one has to take *clogging* into account. The binding site occupancy prevents a motor from stepping on that site, which leads to the slowdown of the active transport, or *traffic jamming*. To obtain the new equations in a comparatively rigorous fashion, we start with a picture of 1D-lattice with biased random walk obeying the Fermi – Dirac statistics (i.e. a motor can not step to an occupied lattice site) [60]. The dynamics of the system (assuming no correlations between lattice site occupancies) are described by an equation similar to the master equation:

$$\begin{aligned} \dot{b}_n &= k_{\rightarrow} b_{n-1} (1 - b_n) + k_{\leftarrow} b_{n+1} (1 - b_n) - \\ &\quad - k_{\rightarrow} (1 - b_{n+1}) b_n - k_{\leftarrow} (1 - b_{n-1}) b_n - \\ &\quad - k_{\text{off}} b_n + k_{\text{on}}^{\text{dl}} (1 - b_n) c_f(z_n), \end{aligned} \tag{3.8}$$

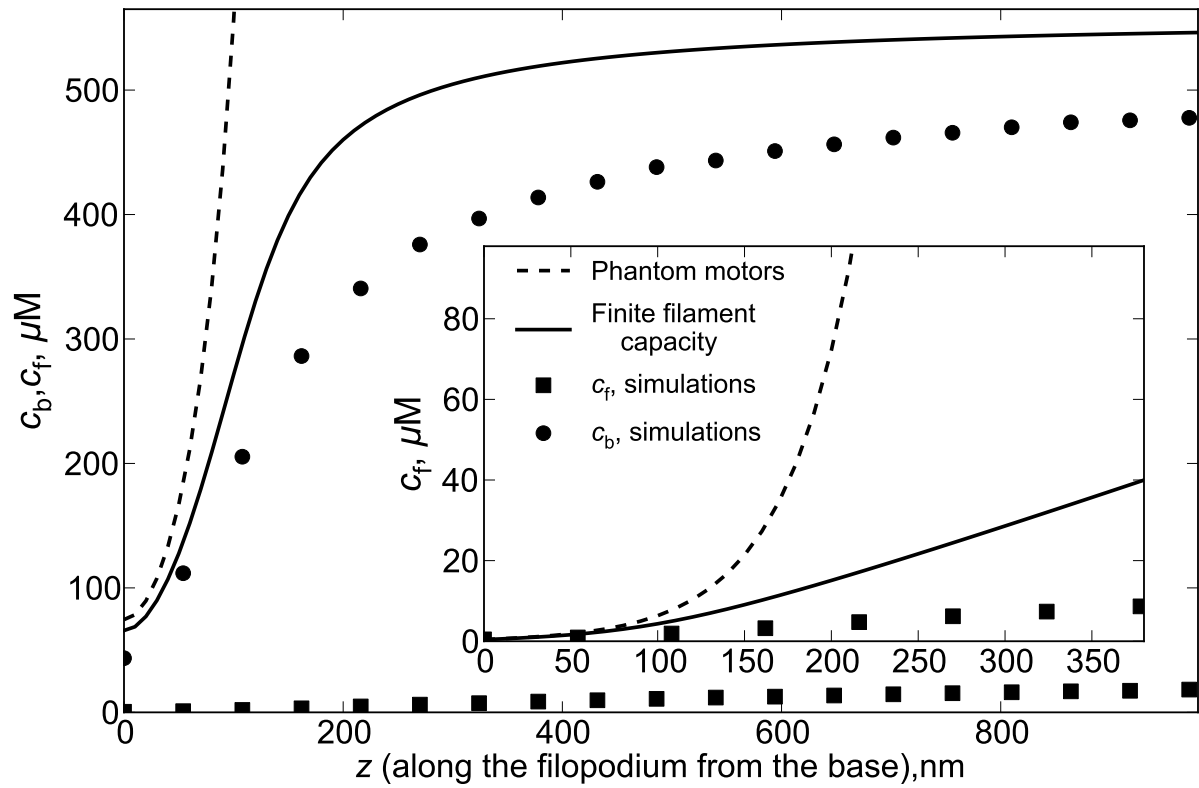


Figure 3.2: Comparison of the mean field analytical models with the stochastic simulation results. The dashed line is the phantom motors model, the solid line is the FFC model, where limited number of binding sites on the filaments is taken into account. Circles are simulation results for c_b , and squares for c_f . Inset zooms into low concentration region to show curves for c_f .

where b_n is the probability that the n -th site is occupied, z_n is the spatial location of the n -th site, and $k_{\rightarrow}, k_{\leftarrow}$ are the rates for the forward and the backward steps. The terms for the fluxes resulting from motor steps are obtained by the product of probability that the source site is occupied and probability that the destination site is free multiplied by the step rate. Although the length of motor step is equal to 12 monomers, and there are several filaments inside a filopodium, these subtleties do not influence the continuum limit ($c_b(z) = c_s b_n$). The continuum version of Eq.3.8 coincides with Eq.3.7 where $J_b = v c_b (1 - c_b/c_s)$ where $v = (k_{\rightarrow} - k_{\leftarrow}) l_{ss}$ and l_{ss} is motor step size. The difference of this expression from the FFC model can be perceived as the modification of the motor speed by the probability that the next site is free. After including the retrograde flow into the final expression for the bound motor flux ($J_b = c_b(v(1 - c_b/c_s) - v_r)$), we get the equations for the jammed motor model(JMM):

$$\begin{cases} -Dc_f'' = k_{\text{off}}c_b - k_{\text{on}}c_f(1 - c_b/c_s), \\ [c_b(v(1 - c_b/c_s) - v_r)]' = k_{\text{on}}c_f(1 - c_b/c_s) - k_{\text{off}}c_b. \end{cases} \quad (3.9)$$

The JMM equations considerably strain the mean field approach, for instance, they have regions of instability. They cannot be solved with finite differences methods (at least, in a physically meaningful way), but for biologically reasonable parameter values, the mean-field treatment can be saved through the phase portrait analysis of the JMM equations. After using the integral $J_f + J_b$ with the BC, we can rewrite the JMM equations as a set of two first order ODEs and investigate it as an evolving dynamical system (with z treated as “time”):

$$c_f' = -\frac{v}{Dc_s}c_b^2 + \frac{v - v_r}{D}c_b, \quad c_b' = \frac{-k_{\text{off}}c_b + k_{\text{on}}(c_b)c_f}{v - v_r - 2vc_b/c_s}. \quad (3.10)$$

We see that c_b' goes to infinity on the singular line $c_b^* = (1 - v_r/v)/2c_s$ except at the point (P) where the numerator in Eq.3.10 is also zero. P is therefore the only point where the

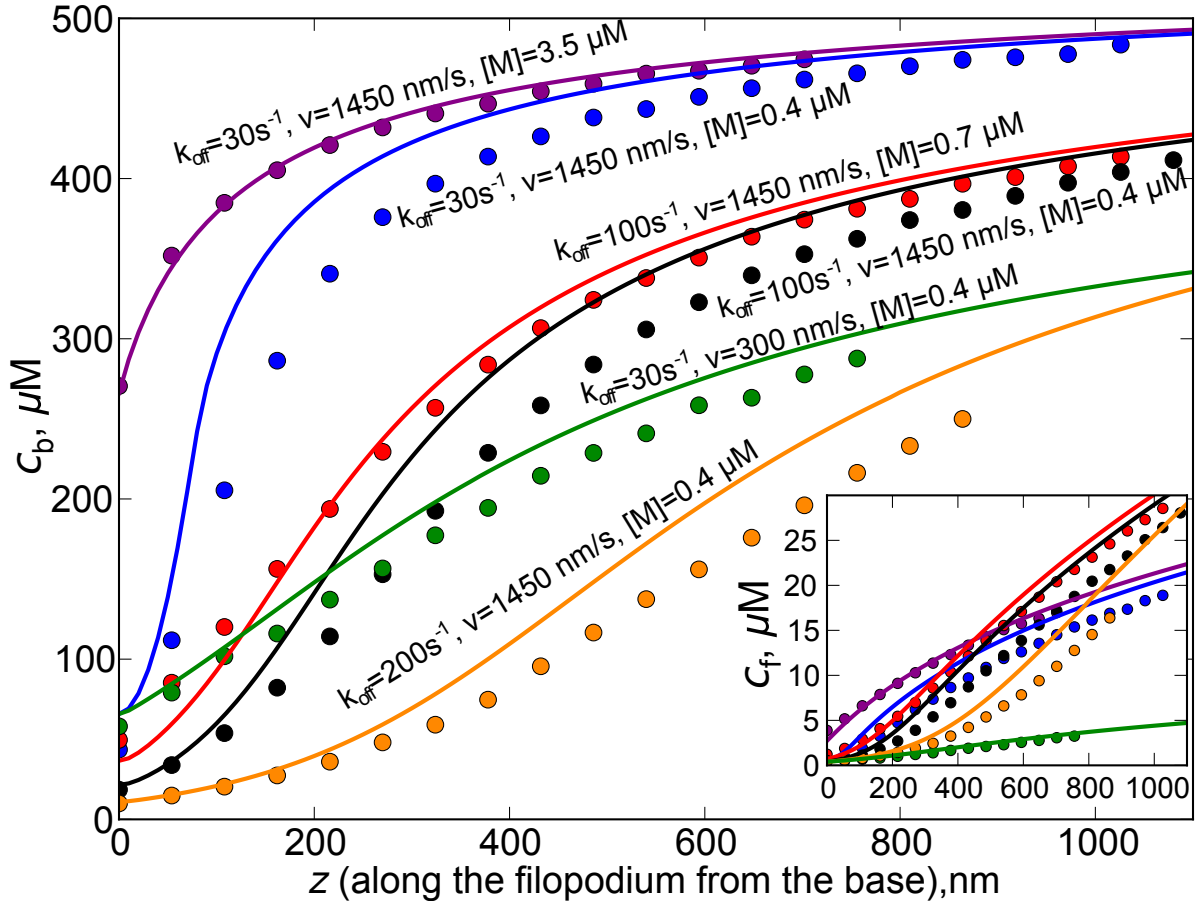


Figure 3.3: Motor concentration profiles inside a filopodium are shown according to stochastic simulations and jammed motors model for various parameter sets (motor affinity to filaments, motor speed, motor concentration). For each set of parameters, the simulations points continue up to the filopodial length from the corresponding simulation. Theoretical curves were computed for all lengths. Inset zooms into low concentration region to show curves for C_f .

trajectory can cross the singular line with a physically meaningful result. Still, c'_b is undefined in P and will take an arbitrary value when calculated numerically. However, we notice that the system has a non-trivial saddle fixed point Q , when $c_f(Q) = k_{\text{off}}/k_{\text{on}}^0(v/v_r - 1)c_s$ and $c_b(Q) = (1 - v_r/v)c_s$. The point Q corresponds to almost fully saturated filaments (allowing just enough directed motor flux, so that it is fully compensated by retrograde flow) and free motors in chemical equilibrium with the filaments – a situation one would expect far from the filopodial base. This situation is actually observed in the FFC model and the simulations. Thus, as “time” approaches infinity, a physically meaningful solution should be approaching the point Q along its stable eigenvector, similar to the FFC solution. Shooting backward in “time” from Q along its stable manifold we recover the solution down to the singular line of $c_b = c_b^*$. To finish the construction of the solution for the JMM we integrate the Eq.3.10 up to the singular line and combine the two parts, thus avoiding the need to cross the singular line.

The solutions for various sets of parameters – k_{off} , $c_f(0)$, and v – are given in Fig.3.3. The JMM gives a very good approximation to the stochastic simulations. We confirmed these stationary solutions, by numerical integration of the time-dependent JMM PDEs.

Our results are in qualitative agreement with experiments on delivering of espin1 by Myosin IIIa (M3a) in stereocilia and filopodia, which show gradually growing and saturating M3a concentration profiles, called “drop-like” by the authors due to the characteristic form of their appearance in fluorescence images [44]. Similar fluorescence shapes would be expected from the curves in Fig.3.3. In particular, the M3a profiles in longer stereocilia have longer saturated regions (bright appearance), which can be explained by our proposed universality of the JMM profiles with respect to organelle length. Indeed, in a longer organelle, a larger part of the same concentration profile would be above the visibility threshold, thus, showing up as a larger saturated region.

In our model, traffic jams build up rather close to the organelle base(Fig.3.3), which compromises the transport role played by motors if it requires them to be walking far from the

base in large numbers. A cell might employ special mechanisms to prevent early jamming, for instance, it could immobilize motors at the organelle tip, effectively removing them from the picture, while they would still show in fluorescence. Localization at the tips is sometimes observed in fluorescence experiments [42, 61]. Whirlin, a scaffolding protein, would be one possible candidate for a motor immobilizer. Whirlin was suggested to form complexes with several Eps8 and myosins [61], so if these complexes are anchored at the tip, they could act as a myosin sink and prevent jamming.

Apart from jamming, the efficiency of transport may be also decreased by sequestration of the delivered material by motors. Thus, when very fast or very long protrusion is required, alternative processes may be needed. For example, in *Drosophila* S2 cells, preformed microtubules are pushed from the center of the cell by kinesins and protrude the membrane forming long processes [62]. In axons, cytoskeletal proteins have to be synthesized locally in the growth cone [40, 63], possibly because the need for their consumption is exceeding the active transport delivery limit.

Mathematically, the “motor” problem is a good example of the need for preliminary qualitative knowledge of the behavior of the system. Solving the FFC model allowed us to construct the JMM solutions, and the simulations provided a consistent check for the mean field model, as well as motivation to challenge the PM model, which turned out to be inapplicable at greater protrusion lengths.

To put the problem in a larger context, it is well known, that stochastic chemical kinetics can be directly mapped onto quantum field theory [64, 65]. In this language, the JMM corresponds to coupled bosonic (diffusing motors) and fermionic (walking motors) fields. Earlier works on the problem of motors in a tube have used bosonic-bosonic(PMM) [59] or fermionic-fermionic [66] theories, which in a mean-field approximation yield equations similar to Eq.3.9. Our work is the first to solve the bosonic-fermionic model, yielding a solution rather different from these prior solutions, and one which matches most closely the physical reality of active

transport in protrusions such as filopodia or stereocilia.

Concluding this part with the most important finding, the stationary distribution of motors in filopodia is universal for all filopodial lengths. This universality is not filopodia- or stereocilia-specific, but generic for enclosed cylindrical environments with diffusion and active transport that have the same BCs. This powerful model can now be used, for instance, to calculate the rate of focal adhesion formation or the flux of actin monomers that can be delivered for polymerization and growth. Luckily, since this flux is independent of the overall length, it is now straightforward to find how the length is modified by active transport using mean-field equations that couple actin transport to filament polymerization dynamics, which is discussed next.

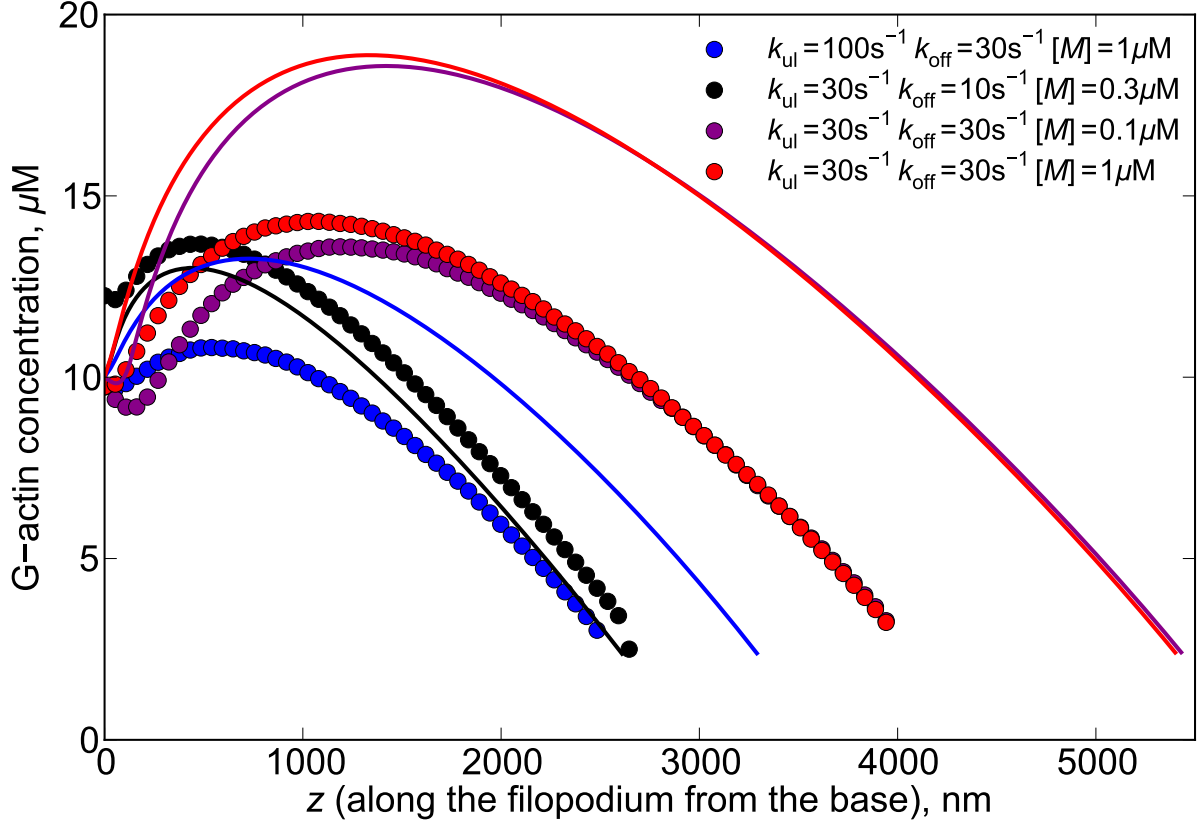


Figure 3.4: G-actin concentration profiles for different parameter values are shown. Circles represent the results of stochastic simulations and lines are the solutions of Eq.3.13 for $a(z)$. All the profiles end when the concentration drops below a_{tip} (Eq.3.12) which is about $2.3 \mu\text{M}$ for our parameter values.

3.3.5 Transport of actin

To model the active transport of G-actin we allow, in addition to the scheme described above, for motors to load and unload G-actin molecules. We consider the case when motors can only load G-actin when they are bound to the filaments, and not when they are free in cytosol. In this way, the problem of sequestration of G-actin by motors [48] mentioned above is avoided. The requirement is not completely artificial, as similar mechanisms are known in other motor systems. For instance, kinesin tail can interact with its head domain in an auto-inhibitory way [67], possibly preventing important interactions between the head and the

microtubule [68]. One possible reason for that is saving ATP, but it could also serve to prevent sequestration of the cargo by freely floating motors.

We will now find the filopodial stationary length along with actin concentration profiles. The length is set by the balance of actin fluxes, which should hold in stationary case just like the balance of motor fluxes discussed above [47]. There are three transport fluxes of actin: diffusional flux $J_D = -D\partial_z a$ (where $a(z)$ is the concentration of freely diffusing actin), retrograde flow flux $J_r = -Nv_r/S\delta = -v_r c_s$ and active transport flux J_{AT} . The stationary condition is $J_D + J_r + J_{AT} = 0$. In addition, at the tip, polymerization converts G-actin to F-actin, directing the sum of all G-actin transport fluxes ($J_D + J_{AT}$) to the retrograde flow. The polymerization flux is $J_P = N(k^+ a_{\text{tip}} - k^-)/S$, where k^\pm are the (de)polymerization rates, and in the stationary case

$$J_P = -J_r = J_D + J_{AT}. \quad (3.11)$$

In other words, the growth (or retraction) stops, when the concentration of G-actin at the tip a_{tip} provides polymerization flux J_P equal to the retrograde flow flux J_r [47]. This condition yields

$$a_{\text{tip}} = (v_r/\delta + k^-) / k^+. \quad (3.12)$$

We proceed to finding the stationary length by finding the whole profile $a(z)$ and seeing where $a(z)$ reaches a_{tip} . G-actin can diffuse, load to the motors-on-filaments and unload, and also be carried forward by them in directed fashion. As discussed in the first section, the stationary motor concentration profile is independent of actin cargo or diffusing G-actin, or of the filopodial length. Therefore, from the actin dynamics viewpoint, $c_b(z)$ is just an external stationary field, not a variable. Thus, after taking into account binding site saturation and traffic jamming, the equations for actin yield a set very similar to Eq.3.9:

$$\begin{cases} -Da'' + k_1 a(c_b - A) - k_{ul} A = 0, \\ [(v(1 - c_b/c_s) - v_r) A]' - k_1 a(c_b - A) + k_{ul} A = 0, \end{cases} \quad (3.13)$$

where $A(z)$ is the concentration of actin carried by motors. The first equation describes the balance of G-actin in solution. In addition to diffusion, the G-actin in cytosol can be loaded on the motors-on-filaments with the loading rate k_1 and unloaded with the rate k_{ul} . The factor $(c_b - A)$ is the concentration of unoccupied motors-on-filaments. The term in square brackets in the second equation, which describes the fluxes of G-actin bound to the motors, is equal to active transport flux J_{AT} (and differs from J_b in the ‘‘motor problem’’ only by having the factor A instead of c_b). The BCs are also similar to those for motors: 1) at the filopodial base the concentration of G-actin is equal to the bulk concentration in the cell, $a(0)$; 2) assuming detailed balance of the loading reaction in the bulk and at the base, $A(0) = k_1 a(0) c_b(0) / (k_1 a(0) + k_{ul})$ (see Appendix A for additional discussion); and 3) like before, we have a conservation law rather than a boundary condition. Finding an integral by summing Eqs.3.13, we obtain $J_D + J_{AT} = \text{const} = -J_r = -v_r c_s$, (after applying Eq.3.11 to find the constant).

Knowing the motors-on-filaments concentration $c_b(z)$ one is able to solve Eq.3.13 numerically. Here we use the solution of Eq.3.9, but $c_b(z)$ could in principle be estimated from fluorescence experiments [42, 44, 61] or detailed stochastic computer simulations. Since all the BCs for Eq.3.13 are related to the filopodial base ($z = 0$), the solution can be constructed starting from zero in a straightforward process. The location of the filopodial tip z_{tip} at the stationary length is the point is set by the condition $a(z_{\text{tip}}) = a_{\text{tip}}$ (Eq. 3.12) is reached is the filopodial tip position at stationary length. To summarize the protocol for our analysis, we first compute the motor profile distribution $c_b(z)$ from Eq.3.9, followed by the G-actin profile distribution, $a(z)$, from Eq.3.13, and finally we determine the steady-state filopodial length by

finding the position z_{tip} , where $a(z)$ intersects with a horizontal line drawn at the height a_{tip} .

From Eq.3.13, we predict that the G-actin distribution in a filopodium growing with the help of non-sequestering molecular motor transport is non-monotonic. This result (also supported by stochastic simulations) is far from obvious, but it can be rationalized through the following arguments. First, assuming J_{AT} is small at the filopodial base, which is often the case, the slope of $a(z)$ has to be negative there, because of the conservation law given by Eq.3.11, which requires balancing of $J_D + J_{AT}$ and J_r at the base. On the other hand, one would expect motors to pump the concentration in the tube, so that it grows as a function of distance from the base, as does $c_b(z)$ itself. Thus, empty motors “vacuum up” the diffusing G-actin near the base, creating the negative slope of $a(z)$ and transporting these bound molecules farther into the tube. Hence, at some point, $a(z)$ starts to increase, so the slope changes to positive, thus creating a minimum (the minimum may nearly disappear at higher J_{AT} values at the base, as seen for a red curve in Fig.3.13). However, at the same time, traffic jam builds up, decreasing the efficiency of G-actin pumping forward, so after reaching a maximum $a(z)$ starts to drop once again (Fig.3.4). Alternatively, the slope of $a(z)$ at the tip has to be negative as well: $a(z) > a_{\text{tip}}$ everywhere inside the filopodium, or it would not be able to grow past the point where $a(z) < a_{\text{tip}}$. With the requirement of the negative slope both at the base and the tip, it could either be a monotonic decrease, or at least one minimum followed by one maximum. In the absence (or inefficiency) of active transport, we observe the former situation, a nearly linear decrease (Fig. S1). When motors do pump G-actin forward, they create a minimum by sucking up G-actin, and then a maximum, after they jam and slow down the pumping of G-actin. Fig.3.5 shows the magnitude of active G-actin flux J_{AT} which starts to drop sharply after the region of jamming build up. Interestingly, in some cases J_{AT} may be higher at the tip when the unbinding rate, k_{off} , is increased, which may seem counterintuitive, as motors in this case are less processive and spend less time on filaments. On the other hand, the jamming starts further in the tube, increasing transport efficiency in these specific cases.

On the left hand side of the broad maximum in Fig.3.4, the J_D is negative and works against the positive J_{AT} (Fig.3.5). After the motor jam builds up, J_{AT} decreases, so J_D has to increase correspondingly because of Eq.3.11. Thus the burden of actin delivery transfers from motors to diffusion, so at the tip J_{AT} can be almost negligible compared to J_D (for one of the parameter sets in Fig.3.5 it is 53 molecules/second vs. 360 molecules/second). Interestingly, J_{AT} is still considerable far from its maximum which is very close to the base due to the quick jam development. One of the factors sustaining J_{AT} is the high value of unjammed motors speed, on the order of micron per second, which can still deliver noticeable flux even when diminished by an order of magnitude due to jamming. However, it turns out it is still mainly the diffusion that delivers monomers to the tips of long filopodia for the most of their lengths. The role of active transport can be formulated as that of increasing the concentration gradient for diffusion through locally increasing the concentration near the base, or in the middle of the filopodial tube. From the point of view of actin flux balance, the latter is the same as having a higher “effective” bulk concentration of G-actin in a filopodium with no active transport.

The mean-field model for actin is either in quantitative or semi-quantitative agreement with the stochastic simulations, depending on model parameters (Fig.3.4-3.6). The filopodial stationary length is reached when the G-actin concentration drops below a_{tip} (Eq. 3.12), equal to $2.3 \mu\text{M}$ for the retrograde flow rate of $v_r = 70 \text{ nm/s}$. The profiles in Fig.3.4 end when they reach this value. In terms of stationary length, and positions and heights of G-actin concentration peaks, the discrepancy between the analytical mean-field solution (solid lines) and stochastic simulations (circles) is less than 20 – 25%. The shapes of the corresponding curves are almost identical, and the discrepancy amounts to scaling the mean-field curves down in both axes. Interestingly, the agreement between mean-field results and stochastic simulations is very accurate for bound species, $c_b(z)$ and $A(z)$, as seen in Fig.3.6, as well as between various transport fluxes (Fig.3.5). Hence, barely noticeable discrepancies for bound species profiles and corresponding fluxes amplify into noticeably larger errors for the cytosolic actin

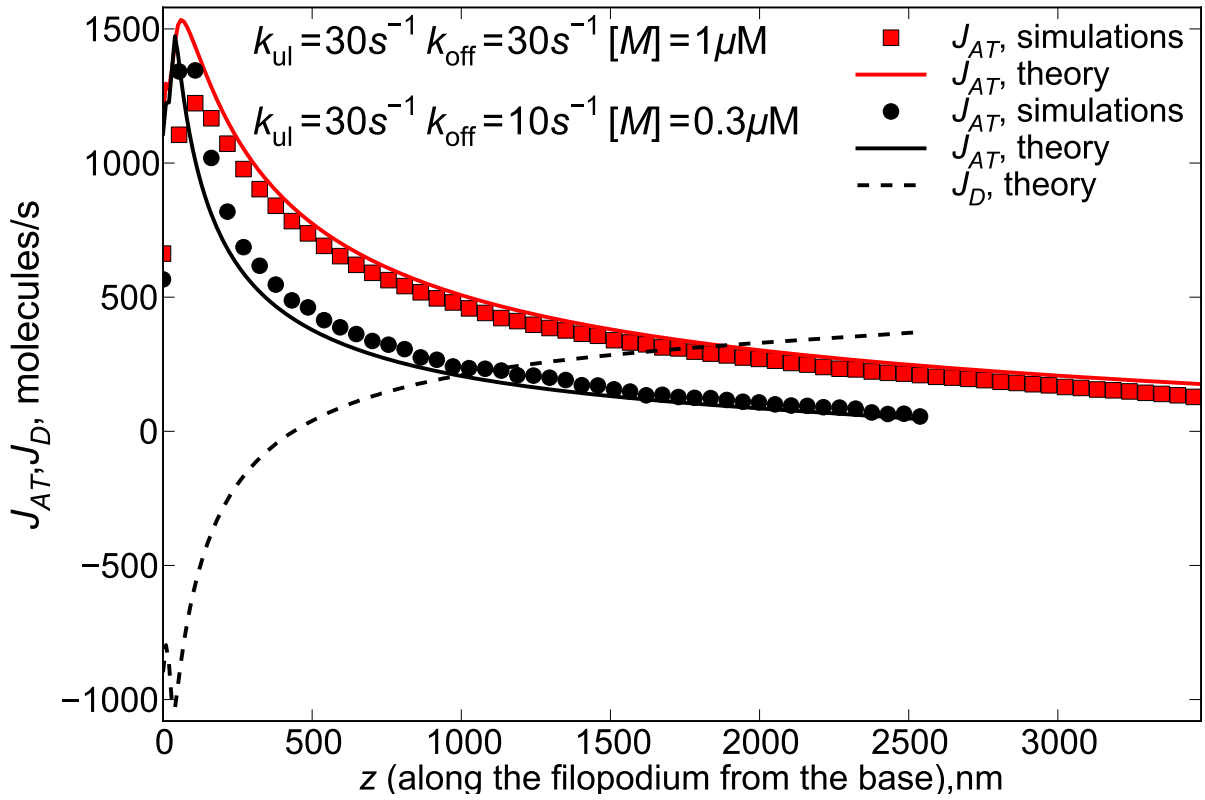


Figure 3.5: Active transport fluxes for different parameter values are calculated as $J_{AT}(z) = (v(1 - c_b(z)/c_s) - v_r) A(z)$. Symbols correspond to $A(z)$ and $c_b(z)$ taken from the results of stochastic simulations, and lines are plotted by taking $c_b(z)$ and $A(z)$ from the solutions of Eqs.3.9 and 3.13. Active transport flux decreases after the traffic jam is formed. The retrograde flow flux J_r of 415 molecules/s determines the flux of G-actin monomers which need to be delivered to the tip at steady state. Dashed line shows the diffusional forward flux of G-actin for $k_{ul} = 30 \text{ s}^{-1}$, $k_{off} = 10 \text{ s}^{-1}$, $[M] = 0.3 \mu\text{M}$ (corresponding to the black curve on Fig.3.4). Active flux is still significant even far from the start of the jam, however, starts to vanish near the tip.

concentration profiles, which in turn determines the filopodial length. This amplification may be understood as a result of pumping current created by motors, which is highly nonlinear. The trend of seeing better agreement for shorter filopodia supports this point of view. Yet another way to formulate the quantitative correspondence between mean-field and simulation results as simple scaling of axes is that noise and fluctuations renormalize the parameters in the mean-field theory [47]. In general, if molecular fluctuations are very strong at small protein copy numbers and couple to nonlinear chemical kinetics, the resulting dynamical behaviors might be rather different from the corresponding mean-field predictions [69,70]. In the context of active transport in filopodia, the fluctuations are moderate within certain regime of model parameters, however, the mean-field picture is destroyed when fluctuations become too large in case of other model parameters, as we have seen in the “motors” part of the problem. In simulations, reaching the steady-state length predicted by the mean-field theory may be a very slow process, taking up to 15 min, sometimes showing more than one distinct stationary or quasi-stationary state [51]. Even within the mean-field theory two different steady states for the same set of parameters are possible (when the first minimum in G-actin profile is lower than a_{tip} (Eq. 3.12)). In such cases the filopodial evolution (and length in particular) can be largely defined by the initial conditions for its growth or retraction. Paralleling the stochastic dynamics of a filopodium to navigating an energy landscape [71], one may suggest that this energy landscape is somewhat rugged, similar to that of spin-glasses or heteropolymers, with many kinetic traps appearing as quasi-stationary states.

3.4 Conclusions

We have constructed a comprehensive set of mean field models to describe a possible mechanism of G-actin active transport inside filopodium or stereocilia. The predictions of these equations quantitatively reproduce most of detailed stochastic simulation results and are con-

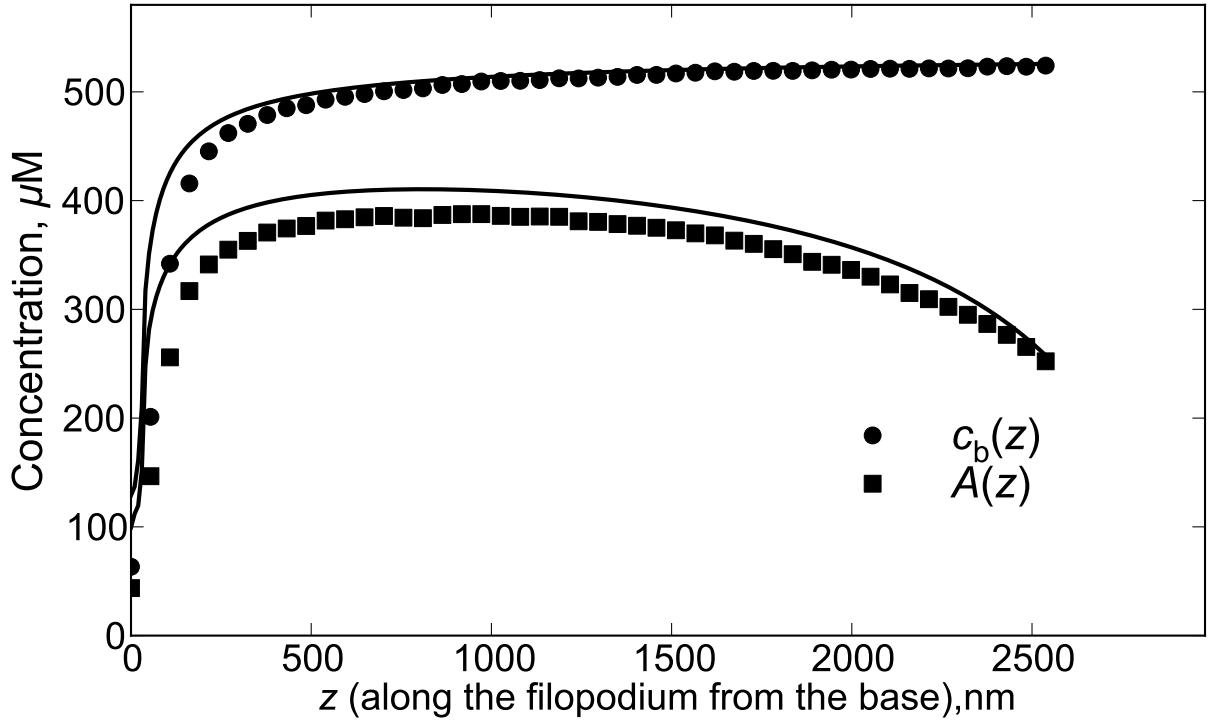


Figure 3.6: Concentration profiles for actin-on-the-motors $A(z)$ and motors $c_b(z)$ are shown for $k_{\text{on}} = 30 \text{ s}^{-1}$, $k_{\text{off}} = 10 \text{ s}^{-1}$, $[M] = 0.3 \mu\text{M}$ (corresponding to the black curve on Fig.3.4) from analytical solution. The concentration of F-actin binding sites $c_s = N/S\delta = 558 \mu\text{M}$ caps $c_b(z)$, while $A(z)$ is in turn capped by $c_b(z)$. Symbols correspond to $A(z)$ and $c_b(z)$ taken from the results of stochastic simulations, and lines are plotted by taking $c_b(z)$ and $A(z)$ from the solutions of Eqs. 3.9 and 3.13.

sistent with a number of experiments on measuring motor fluorescence in actin based protrusions. The concentration profiles of molecular motors are universal, independent of the protrusion length. This is a fundamental property of the problem of motors in a tube, independent of parameters or even the actin-bundle nature of the tubes considered in this work.

According to our model, motors form a traffic jam relatively close to the base of the filopodial tube, which greatly slows down their walking further into the tube. However, local pumping of G-actin up to the jamming region can create enough G-actin concentration gradient for diffusion to be able to sustain filopodia several times longer than in the absence of active transport. The pumping is manifested as a non-trivial concentration profile of diffusing G-actin, with a minimum followed by a maximum. Hence, despite jamming, motor transport can be quite efficient in producing much longer protrusions. Interestingly, multiple steady state solutions seem possible under certain combinations of rate constants and species concentrations, which is an issue that should be explored further both experimentally and theoretically. We also observed that kinetic barriers may slow down the approach to the steady state for longer filopodia and stereocilia, hence, finite-time observations may sensitively depend on the initial conditions, and could explain some of the variability seen among neighboring protrusions of the same cell.

This chapter is reproduced with permission from Pavel I. Zhuravlev, Yueheng Lan, Maria S. Minakova, and Garegin A. Papoian, Theory of Active Transport in Filopodia and Stereocilia, PNAS, in press. Contributions: Maria, Pavel and Garegin have developed three mean-field models; Pavel and Maria have run stochastic simulations; Pavel and Garegin have worked on the discrete description of bound motor dynamics and actin fluxes and spacial profiles; Yueheng characterized and solved the non-linear system of equations for the Jammed Motor Model.

Chapter 4

Position-Dependent Energy Transfer between Ruthenium(II) and Osmium(II) Modified Coiled-Coil α -Helical Peptide Dimers *

4.1 Introduction

The design of molecular materials capable of performing complex functions is pivotal to bottom-up approaches in molecular electronics [72–75], sensing [72, 76, 77] and solar energy conversion [78–84]. The most common strategy for building artificial assemblies uses covalent bond formation to connect molecular components with rigid linkers that dictate both distance and orientation. While this approach provides exquisite control over spatial parameters [85–88], the optimization of functional performance often requires the development of new synthetic routes making the implementation very difficult, especially as the number of molecular components increases. Alternatively, chromophores have been placed on easily synthesized scaffolds such as polymers [89–95], dendrimers [72, 80, 96–107] and organogels [108–111]. However this approach can yield assemblies that are not mono-disperse in molecular weight or chemical composition and incorporate many different morphological constituents. While large systems are readily made and some control over the primary structure is possible, the

*Maria Minakova, Christopher K. Materese, Garegin A. Papoian

flexible scaffolds result in solution structures that vary from one assembly to the next. Another approach to achieve functional architectures draws inspiration from natural systems, which combine simple molecular building-blocks to form highly complex functional systems. Nature exploits relatively weak non-covalent interactions to achieve functional architectures with a hierarchical control, in which sequence defines structure, which defines function. Proteins, lipids, and oligonucleotides form the structural framework that organize functional elements in spatial proximity and with well-defined orientations [112]. To this end, functionalized biological molecules such as oligonucleotides [113–116], amyloid-like peptide fibrils [117], and even derivatized virus coated proteins have been designed and investigated as functional materials [118]. These types of designed systems [117, 119–125, 125–131] that mimic the organizational strategies of biomolecules provide a number of advantages, including design flexibility, ease of synthesis, and spatial control of functionality through supramolecular architectures that allow for fine-tuning of materials properties.

Herein we report the design of an artificial polypeptide system based on a heterodimeric coiled-coil architecture in which the primary sequence defines both the secondary and tertiary structure, which provides fine control of the positioning of octahedral tris(bipyridyl) transition metal complexes $[MII(bpy)_3]^{2+}$ ($M = Ru$ or Os , $bpy = 2,2$ -bipyridyl). Coiled-coils are a common protein motif and provide structural architecture for many important protein scaffolds including α -keratin [132] and tropomyosin [133, 134]. Moreover, the sequence-structure rules are well defined, allowing for the design of highly tunable molecular architectures by control of the primary sequence. In this study we demonstrate the ability of the peptide secondary structure to control relative positioning of the octahedral complexes, resulting in systematic tuning of the energy transfer properties of the system. The $Ru(II)$ and $Os(II)$ metal complexes are positioned near the midpoints of two complementary peptide chains, each consisting of 28 residues (Figure 4.1). The primary sequence of each chain is chosen such that they adopt a dimeric supramolecular structure consisting of two α -helical coils, in which the hydropho-

bic residues are shielded from the aqueous environment and the hydrogen bonding and ionic interactions are maximized. Photo excitation of the Ru(II) complex in the folded assembly results in energy transfer to the lower energy Os(II) acceptor on the opposing chain. Since the metal complexes are placed on different peptide chains, energy transfer is only possible if the two chains associate in solution, making this system particularly sensitive to the secondary and tertiary structure of the peptide scaffold.

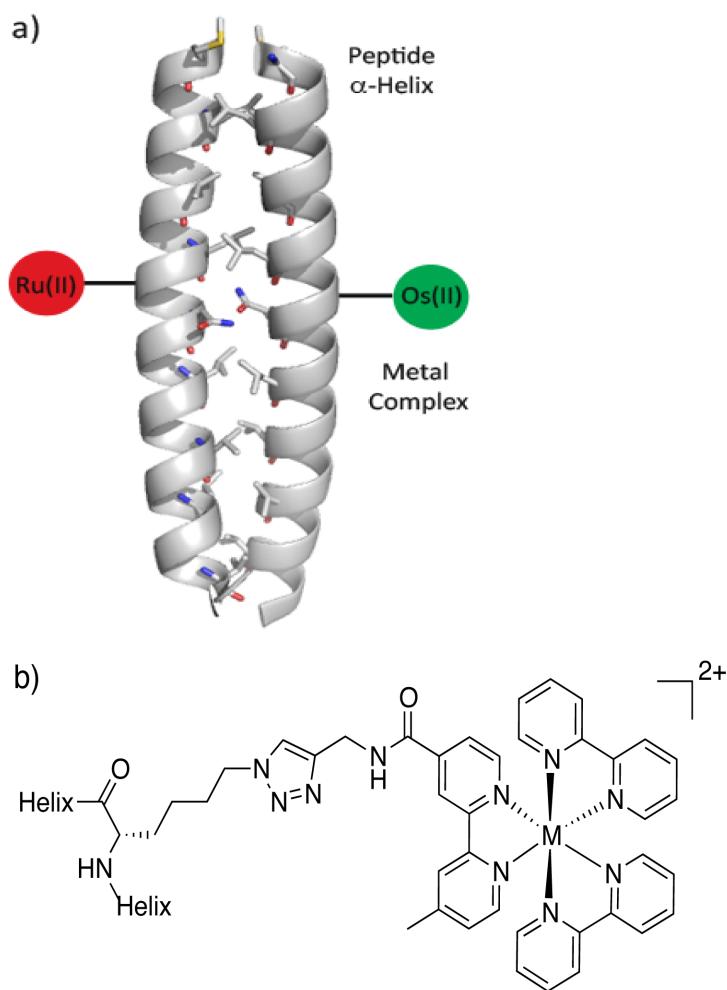


Figure 4.1: (a) Illustration of metallopeptide system containing the α -helical coiled-coil scaffold and metal complexes (coiled coil: pdb 2AHP). (b) Structure of the metal complex and its attachment to the α -helix.

A set of peptide structures that systematically vary the positions of the two metal complexes was studied by taking advantage of two flexible synthetic methodologies: solid-phase peptide synthesis (SPPS) and the copper(I)-catalyzed azide-alkyne cycloaddition (CuAAC or click reaction). SPPS is advantageous as it allows for exact positioning of the chromophores in the primary sequence. The use of click chemistry as an orthogonal linkage strategy between the chromophores and peptides has several advantages. First, it avoids issues with formation of statistical mixtures of species, as was obtained in the electron transfer coiled-coil systems developed by Ogawa, in which the chromophore linkage was accomplished via non-specific coordination chemistry [126–131]. Secondly, click chemistry provides advantages over the direct amide linkage used in the electron-transfer oligoproline systems reported by Meyer, in which orthogonal protecting group strategies had to be employed [123–125]. Variation in the placement of the complexes along the peptide backbone as shown in Figure 4.2 results in predictable changes in the energy transfer rate, which are measured using time-resolved emission methods.

Variation in the rate by almost an order of magnitude across the series, as well as denaturation studies, confirm that energy transfer is the direct result of folding into a well-defined tertiary structure. All-atom molecular dynamics simulations provide insight into the microscopic environment, revealing an assembly with a dynamic, yet robust, tertiary structure that effectively controls the relative positioning of the two complexes.

4.2 Methods

4.2.1 MD Simulation Protocol

Since no crystal structure was available for the system, the initial structure was generated using PyMOL [135], which is a molecular visualization tool capable of constructing simple

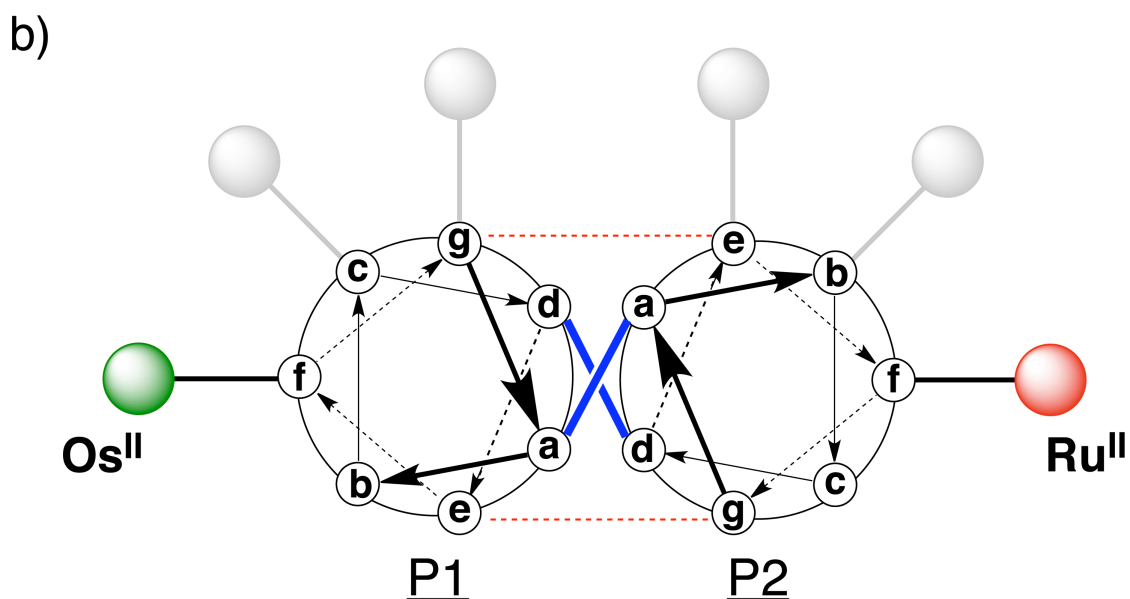
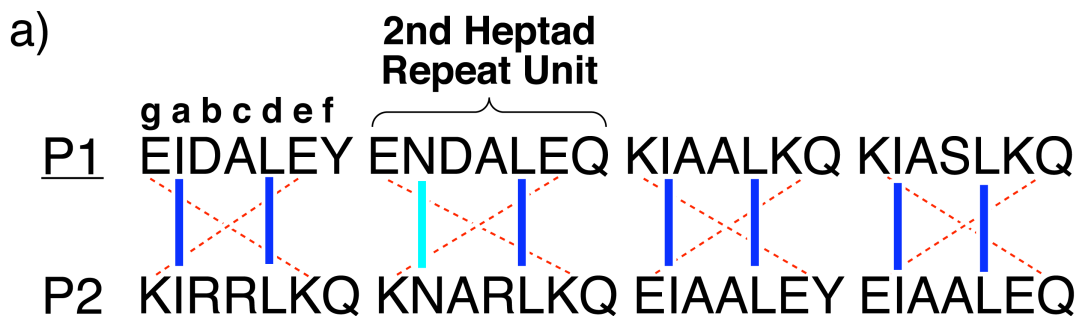


Figure 4.2: (a) Primary sequences of the P1 and P2 peptides using the single letter amino acid code (in capitals). Each 28-residue peptide has four heptad repeat units. The common letter designations for the heptad positions (**a-b-c-d-e-f-g**) are shown above the first heptad repeat unit for P1. The hydrophobic interactions are shown as blue lines, the hydrogen bonding interaction between Asn side-chains is shown as a cyan line, and the complementary ionic interactions between the two peptides are shown as red dashed lines. (b) A helical-wheel diagram displaying the potential points for attachment when viewed down helix axis from the N-terminus. The P1 peptide is modified with Os(II) at the f, c, or g position within the second heptad. The P2 peptide is modified with Ru(II) at the f, b, or c position within the second heptad.

peptides. The *P1* and *P2* peptides were initially generated independently using PyMOL's helical parameters and were then manually aligned with care taken to avoid steric clashes, while satisfying the key hydrophobic contacts at the interface. The tris-(triazolylmethyl)amine ligand segment was constructed using Gaussview, part of the Gaussian 03 suite [136]. Ruthenium(II) and osmium(II) are very similar from an MD perspective. Since the primary focus of these simulations is peptide dynamics, ruthenium was used as the central atom in both complexes and osmium was not explicitly included. This is not expected to have any significant impact on the simulations, since the metal atoms are nearly completely shielded from the rest of the system by the the bipyridyl ligands, and metals formal charge, which is the same for Ru(II) and Os(II), plays the most important role. In order to examine the effect of linker positioning on the complexes, the following three systems were created: System 1, which corresponds to the *2f-Os/2f-Ru* metallopeptide pair, System 2 which corresponds to the *2c-Os/2b-Ru* metallopeptide pair, and System 3 which corresponds to the *2g-Os/2e-Ru* metallopeptide pair.

The simulations were prepared using the AMBER [137] force field with the ff99SB [138] parameter set. Since the AMBER libraries do not possess parameters for the artificial amino acids used as tethers, or for the chromophores themselves, these values needed to be collected from literature or obtained through quantum calculations. Partial charges for the linker and chromophores were obtained through Gaussian calculations using the restricted B3LYP [139] with the LANL2DZ [140] basis set. Charges derived using the restricted electrostatic potential (RESP) technique [141] gave spurious results for the ruthenium and the chelating nitrogen atoms in the bipyridyl ligands. RESP has difficulty predicting the correct charge for buried atoms since the charges are assigned in an effort to reproduce the external electrostatic potential [141]. Because of this, Mulliken charges were used in lieu of RESP charges. In general, Mulliken charges tend to be slightly more exaggerated than RESP charges with an average difference in predicted charge of $0.1(\pm 0.1)e$ for all atom excluding the ruthenium and those atoms immediately surrounding it. There was insufficient memory to compute partial charges

for the entire linker and complex. In order to deal with this issue, the partial charges for the base of the peptide up to the γ -carbon of the side chain were extracted from the standard lysine amino acid residue. Force constants for Ru-N stretches, N-Ru-N (*cis/trans*) bends, C-C-N-Ru dihedrals, H-C-N-Ru dihedrals and van der Waals parameters were obtained from Brandt et al. [142]

Since AMBER does not explicitly support Octahedral geometry, chelating nitrogen atoms were divided into three distinctly named but chemically identical types in order to establish different bending force constants for *cis* and *trans* positions. Each of the three simulations were performed with 13000 explicit TIP3P water molecules in a box with the dimensions $\approx 75 \times 75 \times 75 \text{ \AA}$ under periodic boundary conditions. The charge of each system was neutralized by the addition of sodium counter ions, followed by the subsequent introduction of an additional 10mM NaCl. Each system was held at constant volume, and the peptides were frozen in place while the water and ions were minimized for 200,000 steps. Subsequently, all constraints were removed from the systems and they were minimized for an additional 200,000 steps. The systems were gradually heated via Langevin temperature control to 300 K in the incremental steps of 5 K every 50 ps.

The production runs proceeded under the constant pressure, moderated by Langevin piston (set to 1 *atm*), with 2 *fs* time steps using the SHAKE algorithm and Ewald summation for long-range interactions. Short-range non-bonded interactions were calculated at each step, while long-range interactions were only calculated on even steps and the pair list was updated every 10 steps. System coordinates were saved every 2000 steps (4 *ps*) for analysis for a total simulation length of 300 *ns* for each system.

4.3 Results and discussion

All atom molecular dynamics simulations were performed on each of the three coiled-coils to gain insight into the molecular level interactions in these systems. Since Ru(II) and Os(II), when enveloped by the bipyridyl ligands, are practically identical from a molecular dynamics perspective, Ru(II) was used as the central atom for simulation in both bipyridyl complexes. For the sake of concise comparisons with experiments, we retain the same nomenclature for the metalloprotein pairs. It is important to mention that since a single metal-metal distance can map into a variety of different conformational arrangements between two metal complexes, we present below detailed trajectory analysis, with supplementary movies providing additional structural information (see Appendix B).

4.3.1 *2f-Os/2f-Ru* Heterodimer

Both bipyridyl complexes in the *2f-Os/2f-Ru* system start from a distal position relative to the peptide backbone. During the equilibration phase the complexes were frequently found in the proximity of the coiled-coil peptide backbone, likely driven by favorable hydrophobic interactions. To overcome the bias of the deliberately chosen initial conditions, the first 250 *ns* of the simulation were not included when calculating the distance distributions. The subsequent data collection phase was run for approximately 500 *ns*. The dynamics of the bipyridyl complexes and their unnatural side chains can be described by two regimes. First, there are large-scale conformational rearrangements during which the tethered complexes escape from their states bound to the coiled-coil and are free to explore the phase space to find new collapsed conformations. Secondly, there are small-scale oscillations within these conformations, which occur on a much faster timescale, but do not result in significant displacement of the metal complexes.

The attachment points for the bipyridyl complexes in the *2f-Os/2f-Ru* system are far enough

Table 4.1: Dependence of the Coiled-coil Secondary Structure and Metal-Center Displacement on Substitution Position.

	Helicity index α , X-Os-P1	Helicity index α , Y-Ru-P2	Ru-Os average distance
X=2f, Y=2f	0.458 ± 0.097	0.559 ± 0.079	3.100 ± 0.336
X=2c, Y=2b	0.631 ± 0.139	0.593 ± 0.124	1.444 ± 0.319
X=2g, Y=2e	0.249 ± 0.097	0.070 ± 0.116	1.195 ± 0.048

away from each other that the two complexes do not come into direct contact during the entire course of the simulation. The corresponding metal-center displacement distributions and the trajectories from which they were derived are shown in Figure 4.3.

The inter-metal distance distribution is broad (over a 3 nm range) and non-Gaussian. Throughout the course of the simulation, the metal-center displacements observed for the *2f-Os/2f-Ru* system are relatively large and would be expected to limit the efficiency of energy transfer. As discussed above, these simulations indicate that the Frster energy transfer mechanism may play an important role for this complex.

Interestingly, the bipyridyl complexes appear to influence the stability of the *2f-Os/2f-Ru* coiled-coil structure as illustrated in the Appendix B Movie 6. α -Helical peptides have an increased propensity toward fraying near the termini, and when the metal complex and the *2f-Os/2f-Ru* peptide terminus approach each other, the complex can entrain the ends of the peptides by providing competing hydrophobic interactions which result in further fraying. This partial folding and unfolding can be observed in the timeline plot of the helicity index α which is equal to the ratio of the number of residues in the α -helical conformation compared to the total number of residues in a sequence (see Figure 4.4 and Table 4.1). The implications of this observation are elaborated below.

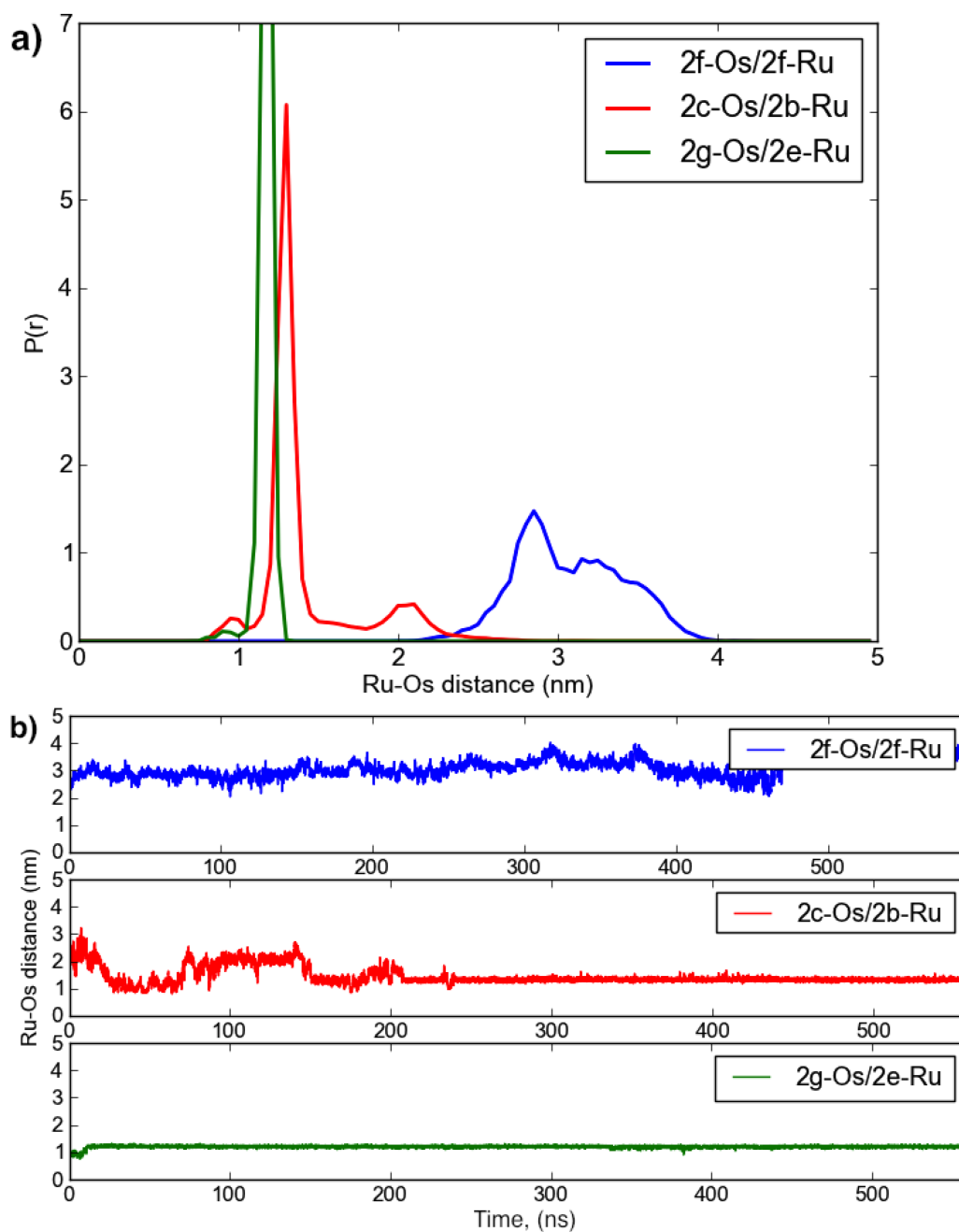


Figure 4.3: (a) Comparative plot of Ru-Os distance histograms (normalized) for different chromophore placements, including $2f\text{-Os}/2f\text{-Ru}$, $2c\text{-Os}/2b\text{-Ru}$, and $2g\text{-Os}/2e\text{-Ru}$. (b) Ru-Os distance evolution in time for the $2f\text{-Os}/2f\text{-Ru}$, $2c\text{-Os}/2b\text{-Ru}$, and $2g\text{-Os}/2e\text{-Ru}$ metallopeptide pairs.

4.3.2 *2c-Os/2b-Ru* Heterodimer

After extensive equilibration for approximately 300 ns, the initial conformation for the data collection corresponded to spatially separated bipyridyl complexes with relaxed linkers and a slightly perturbed structure for the coiled-coil scaffold. During the first 20 ns of the production run, the bipyridyl complexes do not form any stable close contact, with one complex actively exploring the surface of the peptide scaffold. At 25 ns the two complexes contact each other and form a loose association, in which a single bipyridyl ring aligns with the triazole ring of the complementary peptide linker (see Figure 4.5a). This was followed by closer stacking of the metal complexes, and resulted in characteristic parallel alignment of bipyridine rings (see Figure 4.5b). The metal complexes showed relatively fast (0.2 ns) conformational rearrangement of the bipyridine rings between them, often including a non-parallel, 45° meta-stable stacking (see Appendix B Movie 1 and 2). The comparative graph of distance distributions in Figure 4.3 shows that *2c-Os/2b-Ru* system has a roughly bimodal distribution dominated by the close-packed geometry. The timeline of Ru-Os distance has a feature of switching from one basin with more closely packed state(s), in which bipyridine rings align in a mostly parallel fashion (Figure 4.5b), to another, where the complexes are in close proximity to one another, yet not in direct contact. These conformations correspond to the *2c-Os* bipyridine ring stacking with the triazole ring of *2b-Ru* linker, as shown in Figure 4.5a. In this system, we did not observe a similar perturbation of the peptide scaffold by the bipyridyl complexes as was seen in the *2f-Os/2f-Ru* system. The peptide termini dynamically unfold and refold during the course of simulations (see Appendix B Movies 2 and 3), but not due to association with the bipyridyl complexes in this case. The helicity index of the *2c-Os-P1* and *2b-Ru-P2* peptides is shown in Figure 4.4. Interestingly, the standard deviation of the helicity index is approximately twice that of the *2c-Os/2b-Ru* system, indicating that peptides are more dynamic and actively explore their phase space (see Table 4.1).

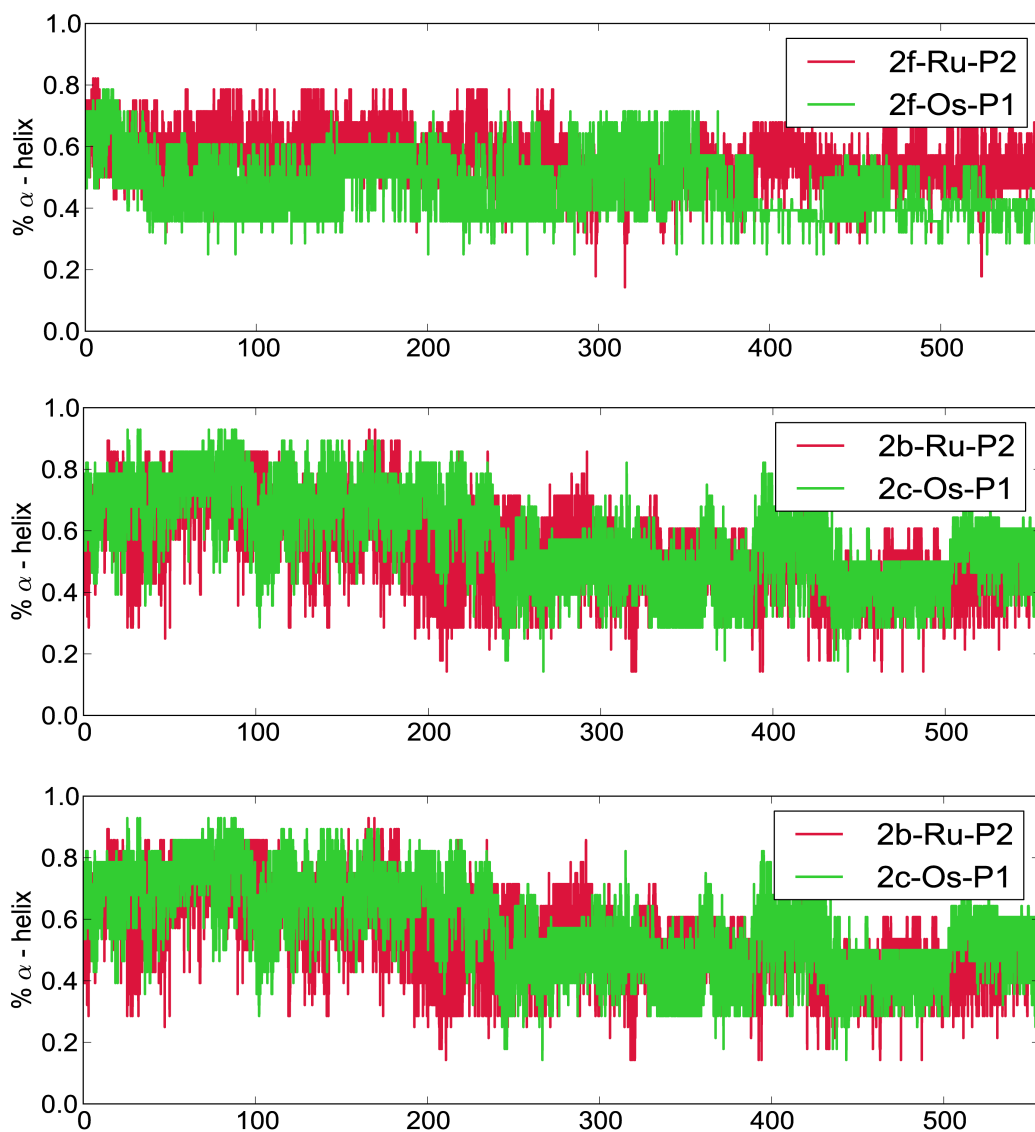


Figure 4.4: Fraction of α -helical content in each peptide as a function of time shown for the *2f-Os/2f-Ru* (top), *2c-Os/2b-Ru* (middle), and *2g-Os/2e-Ru* (bottom) metallopeptide pairs. Each peptide actively explores its conformational space, while predominantly staying in an α -helical state. The exception is *2g-Os/2e-Ru* system (see bottom graph), where an unfolding event is caught during MD. Visualization of the trajectory showed that peptide termini started interacting with the bipyridyl complexes and significantly disrupted the overall coiled-coil ternary and secondary structure.

4.3.3 *2g-Os/2e-Ru* Heterodimer

In a manner very similar to the two previous systems, the bipyridyl complexes in the *2g-Os/2e-Ru* system quickly collapsed onto the coiled-coil peptide scaffold during the equilibration phase 250 ns . The two metal complexes came into Van der Waals contact with each other in a conformation very similar to the intermediate stacking arrangement that was observed in the *2c-Os/2b-Ru* system (Figure 4.5a). For 30 ns the bipyridyl complexes fluctuate between the tight and loose ligand stacking state, as shown in Figure 4.3b. Finally, we observe one more major conformational rearrangement where a tight neck stacking is achieved, which is characterized by the bipyridyl ring and a part of the connected linker of one complex aligning with the corresponding structural parts of the other. As a result, the complexes are facing away from each other (see Figure 4.5c and Appendix B Movie 4). This conformation, which was not observed in the *2c-Os/2b-Ru* system, persists until the end of the simulation. As shown in Figure 4.5c and Appendix B Movie 5, the bipyridyl complexes in the *2g-Os/2e-Ru* system also maintain a close proximity with the bipyridyl ligands spending most of their time in van der Waals contact.

This neck stacking creates a significant amount of strain for the peptide scaffold, as well as an additional hydrophobic surface consisting of the linker side chains pulled together. We show in Figure 4.5c and Appendix B Movie 5 that the peptide termini closest to the bipyridyl complex detach from the coiled-coil interface and bind to the groove between linkers or wrap around the bipyridyl complexes themselves, leading to more disruption of the coiled-coil structure, compared with the other two systems (see Figure 4.5). The analyses of the simulation data for all three systems suggest that the various placements of the complexes lead to a variety of ways in which chromophores interact with the underlying peptide scaffold and influence the corresponding coiled-coil stabilities (see Table 4.1).

Furthermore, the trends predicted from the MD simulations are qualitatively consistent with

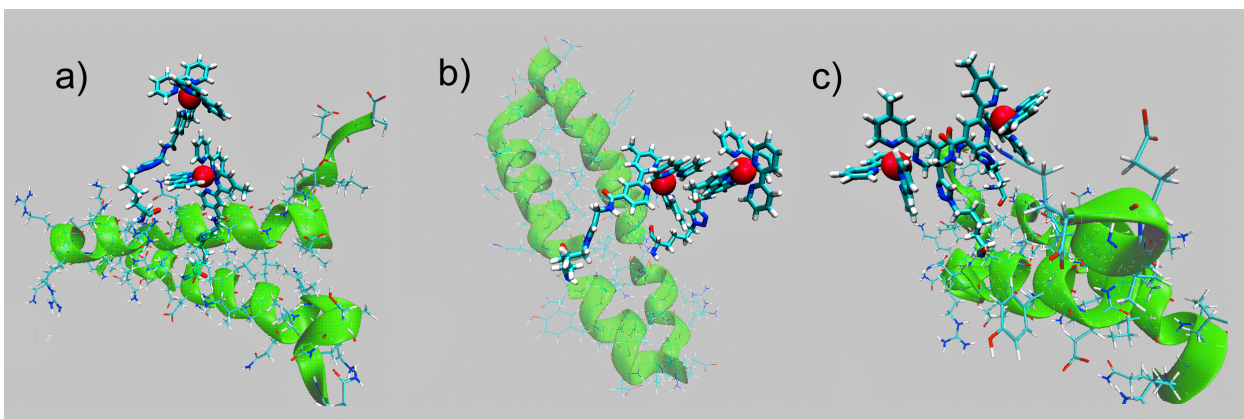


Figure 4.5: (a) Loose stacking arrangement of the bipyridyl complexes (2 nm feature) is a stable basin of conformations with characteristic parallel alignment of one of bipyridine rings and the triazole ring of the linker. This tightly stacked conformation is observed consistently in the *2c-Os/2b-Ru* system and briefly in *2g-Os/2e-Ru* system. This stacking is transitory to closer inter complex stacking conformations. (b) Close stacking arrangement where bipyridyl rings of two complexes are in Van der Waals contact and parallel to each other (1 nm feature). (c) Bipyridyl ligands arranged in a neck conformation, facing away from each other (1.2 nm feature). This conformation was only observed in the *2g-Os/2e-Ru* system.

Table 4.2: Thermodynamic Stability of the Metallopeptide Heterodimers determined using Guanidinium denaturation.

Peptide Pair	ΔG_{unfold}	K_d	α -Helicity index
<i>2f-Os/2f-Ru</i>	8.6	0.49 ± 0.09	80%
<i>2c-Os/2b-Ru</i>	8.2	0.97 ± 0.2	74 %
<i>2g-Os/ 2e-Ru</i>	8.0	1.4 ± 0.3	72 %

the corresponding thermodynamic measurements done by our collaborators from Dr. Waters group (see Table 4.2). They have studied peptides thermodynamic stability using guanidinium denaturation. This method has been used to compare small structural variations within families of similarly designed coiled-coils.

In those experiments, Gibbs free energy change of unfolding (ΔG_{unfold}) was measured for each of the metallopeptide dimers using the method of linear extrapolation. As may be expected, the *2f-Os/2f-Ru* pair formed the most thermodynamically favorable heterodimer (Ta-

ble 4.2). The value of ΔG_{unfold} measured for the *2f-Os/2f-Ru* pair, $8.6 \pm 0.10 \text{ kcal/mol}$, corresponds to a dissociation constant (K_d) equal to $0.49 \pm 0.09 \mu\text{M}$. The α -helicity of the fully folded *2f-Os/2f-Ru* dimer was calculated to be 80 %, based on molar ellipticity measurements at 222 nm ($-28,600 \pm 800 \text{ deg} \cdot \text{cm}^2 \cdot \text{dmol}^{-1}$). The α -helical content determined for the *2f-Os/2f-Ru* dimer falls within the range reported for similar sequences, since values from 69-96% are common for three to five heptad repeat coiled-coils [126–131]. The fact that it is less than 100% helical likely arises from end-fraying, which agrees with what we see in the all-atom MD simulations. Also the overall trend of close stacking of chromophores leading to a slight disruption of the peptide secondary structure is also in qualitative agreement with our simulation results.

However the quantitative extents of the coiled-coil disruption seen in simulations are likely overestimated. The following possibilities could have contributed to producing extra fraying in our MD simulations: 1) overestimating the metalcomplex-peptide interactions, 2) underestimating the strength of the inter-peptide bonding, or 3) preparing the initial coiled-coil conformations in an imperfect way, which did not allow tight enough packing of side-chains or accurate enough alignment of hydrophobic interactions.

In summary, comparison of the dynamics for all three metallopeptide systems shows that the *2g-Os/2e-Ru* pair has the narrowest Ru(II) to Os(II) distance distribution with the smallest probable separation (1 nm), and would therefore be the best promoter for energy transfer. A metal-metal distance of 1 nm suggests that the complexes are in close contact with each other and would imply efficient energy transfer, regardless of the mechanism considered. This is in agreement with the photo-physical measurements made on the metallopeptide systems by our collaborators in Dr. Papanikolas's group (see Figure 4.6 and Table 4.3). They compared the Ru(II) emission quenching for the three coiled-coil metallopeptide pairs: *2f-Os/2f-Ru*, *2c-Os/2b-Ru*, and *2g-Os/2e-Ru* (Figure 4.6), along with the transients from three coiled-coils containing the Ru(II) metallopeptides paired to the P1 apo-peptide. All three of the P1/Ru(II) sys-

Table 4.3: Results of the global analysis showing the dependence of the energy transfer rate on the position.

	$K_a, \mu M^{-1} (K_d, \mu M)$	$k_{Ru}, \times 10^6 s^{-1}$ (lifetime, ns)	$k_{EnT}, \times 10^6 s^{-1}$ (lifetime, ns)
<i>2f-Os/2f-Ru</i>	0.908 ± 0.005 (1.101 ± 0.006)	2.900 ± 0.002 (478.7 ± 0.5)	1.00 ± 0.02 (816 ± 14)
<i>2c-Os/2b-Ru</i>	0.919 ± 0.001 (1.008 ± 0.002)	2.200 ± 0.002 (450.0 ± 0.5)	3.00 ± 0.02 (304 ± 2)
<i>2g-Os/2e-Ru</i>	0.887 ± 0.001 (1.127 ± 0.001)	2.100 ± 0.002 (468.2 ± 0.4)	23.0 ± 0.1 (42.0 ± 0.2)

tems exhibit qualitatively similar mono-exponential decay kinetics (Table 3). Each transient in the mixed Ru(II)/Os(II) systems is bi-exponential, where the slow component arises from the free Ru chains in solution and the fast component reflects Ru quenching due to energy transfer. The peptide pair that places the complexes the farthest apart, *2f-Os/2f-Ru* (see the blue line in Figure 4.6), has the largest distance between alpha carbons (14.0-14.9 Å), and results in the slowest energy transfer. The *2g-Os/2e-Ru* peptide pair (see the green line in Figure 4.6) places the complexes the closest to each other with an α -carbon distance of 9.6-10.3 Å, and has the fastest energy transfer. Lastly, the *2c-Os/2b-Ru* peptide pair has an intermediate spacing (12.7-13.5 Å) and its energy transfer rate falls in the middle (see the red line in Figure 4.6). The trend of the quenching rates indicates that the peptide assembly influences the relative positions of the Ru(II) and Os(II) complexes, and thus their ability to undergo energy transfer, in a predictable manner. These results combined together indicate the *2g-Os/2e-Ru* pair to be the most efficient energy transfer promoter.

Importantly, we have not observed unfolding of the coiled-coil near the linker attachment points for any of the three systems. This suggests that the dynamics of the bipyridyl complexes themselves do not impose a significant stress along the peptide backbone in our scaffold design. To gain deeper insights into the mechanisms of energy transfer in these systems, subsequent

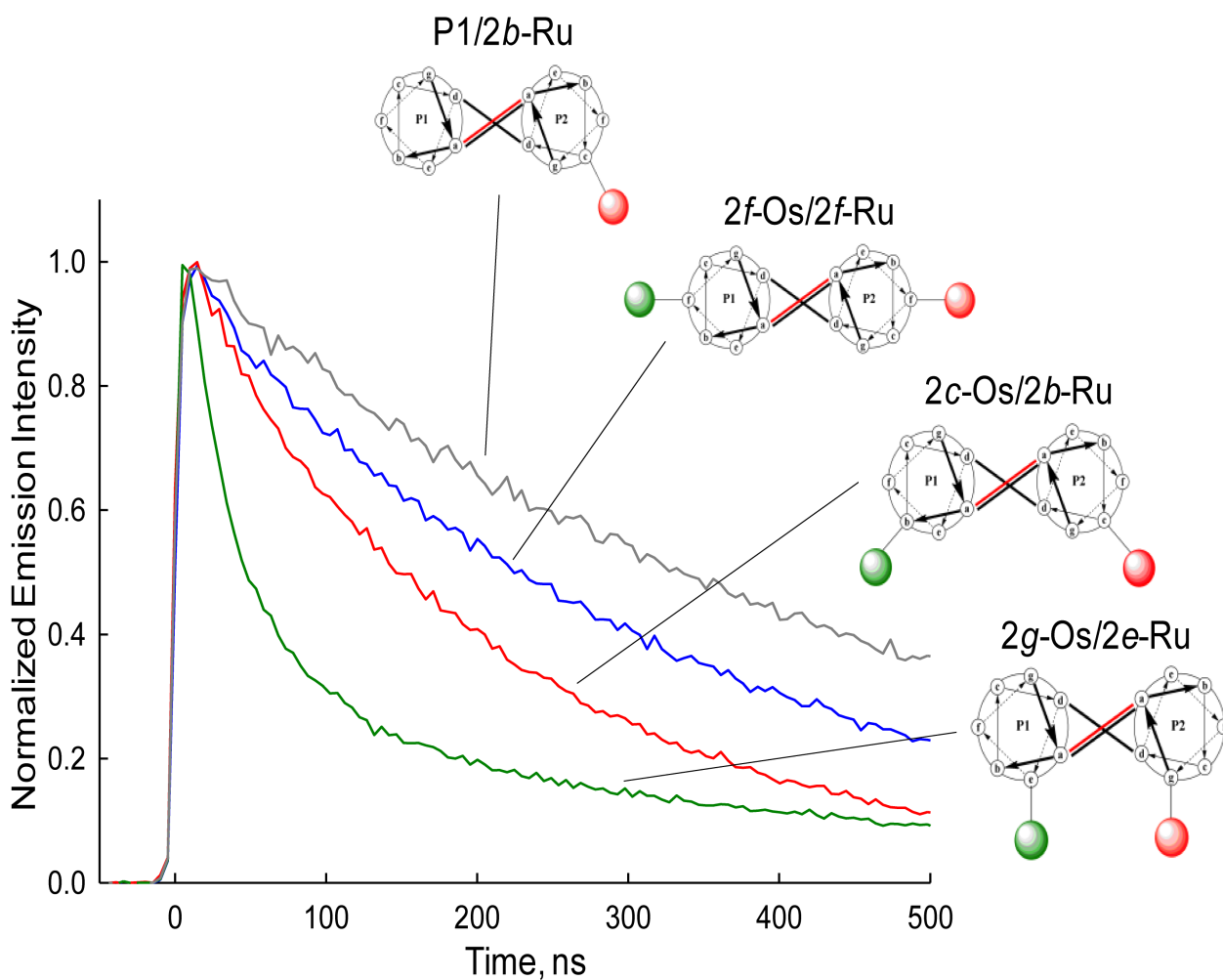


Figure 4.6: Time-resolved emission transients showing the distance dependence of the energy transfer rate for the *2f-Os/2f-Ru* (blue: 25 μM 2f-Ru and 50 μM 2f-Os), *2c-Os/2b-Ru* (red: 25 μM 2b-Ru and 50 μM 2c-Os), and *2g-Os/2e-Ru* (green: 25 μM 2e-Ru and 50 μM 2g-Os) peptide pairs in 10 mM phosphate buffer solution at pH 7 and 25 $^{\circ}\text{C}$. The P1/2e-Ru peptide (grey: 25 μM 2e-Ru and 50 μM P1) is shown for comparison. From the transients it is clear that the energy transfer rate is faster the closer the metal complexes are placed to one another. The time-resolved emission data were collected at 660 nm with an excitation wavelength of 444 nm.

quantum mechanical calculations can be carried out on selected structural snapshots of stable stacking conformations observed in the MD simulations. This, in turn, may help to improve the design of peptide scaffolds, allowing for more precise control over the molecular components.

4.4 Conclusions

The ability to control the positioning and organization of molecular components is central to the design of functional molecular-based materials [78–81]. However, architectures that rely solely on covalent bonding for structure (e.g. polymers, dendrimers) have limited control over the assembly geometry and higher-order spatial control. Using peptides as scaffolds, our team of three laboratories have designed an artificial self-assembling system that utilizes weak forces to control the relative placement of Ru(II) and Os(II) complexes. The assemblies incorporate an α -helical coiled-coil peptide scaffold consisting of α -helical heterodimers in which each coil is functionalized with either a Ru(II)-containing energy donor or with an Os(II)-containing energy acceptor. This architecture differs from many other types of molecular assemblies in that it uses both intra- and intermolecular non-covalent interactions to adopt well-defined secondary and tertiary structures that control the placement of the energy transfer complexes. We performed extensive and detailed all-atom MD simulations of this novel compound for several topological placements of the chromophores and combined our observations with the experimental results obtained by groups of Dr. John Papanikolas and Dr. Marcey Waters. Circular dichroism spectroscopy in conjunction with time-resolved emission spectroscopy confirms the importance of the heterodimeric α -helical coiled-coil structure for modulating energy transfer. Ru(II) to Os(II) energy transfer is only observed in the folded structures, and energy transfer rates measured across a series of structures are consistent with a systematic variation of the metal complex separation.

Molecular dynamics simulations show Ru(II)-Os(II) distance distributions that are consis-

tent with the order of the experimentally measured energy transfer rates. In addition, the simulations suggest that the assemblies maintain their α -helical character, but are dynamic in nature, with stable cores but multiple conformations inter-changing on the nanosecond timescale. These studies demonstrate the sequence-structure-function paradigm found in natural proteins in a robust artificial self-assembling system and provide a promising new scaffold for functional materials that couples straightforward synthesis with a fine control of three dimensional structure.

This chapter is partially reproduced with permission from Dale J. Wilger, Stephanie E. Bettis, Christopher K. Materese, Maria Minakova, Garegin A. Papoian, John M. Papanikolas, and Marcey L. Waters, Position-Dependent Energy Transfer between Ruthenium(II) and Osmium(II) Modified Coiled-Coil α -Helical Peptide Dimers, Inorganic Chemistry, Article ASAP, June 8, 2012. Contributions: Dale under supervision of Marcey has made the complexes, performed structural experiments and provided samples for the photophysical experiments; Stephanie under supervision of John performed photophysical measurements; Christopher under supervision of Garegin has run DFT, equilibration and the beginning of the productive runs for the computational study. Maria under supervision of Garegin has worked on various alternative designs (not reported herein), structure corrections to the initial setup and following equilibration and production runs. Christopher and Maria analyzed chromophore-chromophores distance distributions. Maria has studied visual dynamics and elucidated chromophore packing conformations and analyzed peptide secondary structure dynamics.

Chapter 5

Non-equilibrium Water Transport in a Nonionic Microemulsion System *

5.1 Introduction

Microemulsions have been of great fundamental and industrial interest for many decades [143]. In addition to the rich morphological behavior, microemulsions have a valuable property to store and transport small and macro- molecules, allowing a wide range of applications, including drug storage and release, oil recovery, textile cleaning, preparation of various cosmetic products and perfumes, and food industry [143].

Water transport as a particular example of mass transport has great importance in membrane and microemulsion science, especially for biological systems. Although, water transfer has been more extensively studied in application to synthetic and biological membranes [144–153], passive (diffusive) and active (usually osmotic) water transport in various emulsions and microemulsions has also been investigated [146, 154–162]. On the macroscopic scale, in absence of osmotic pressure, coalescence is believed to be a major transport mechanism [163]. On the mesoscopic scale, it was suggested that water transport could occur through the formation of reverse micelles [146, 156], spontaneous emulsification [158, 159], hydrated surfactants [154], and diffusion of single molecules [160]. All these mechanisms have been

*Maria Minakova, Alexey Savelyev, Garegin A. Papoian

observed under different conditions, but no unified picture has been created so far. Consequently, most of the available knowledge on molecular transport in microemulsions was obtained mainly from the macroscopic scale measurements, which do not provide direct atomistic insight [146, 154, 159, 164].

To shed light on the microscopic mechanisms of water transport, Molecular Dynamics (MD) simulations with All-Atom (AA) resolution can be used. Although, it is challenging to study long time scales phenomena with AA MD simulations, they give more detailed and thorough view on the dynamical behavior of a system. In particular, they do not contain strong simplifications that are characteristic of coarse-grained computational models. In this work, we used atomistic Replica Exchange Molecular Dynamics (REMD) simulations to investigate a non-ionic ternary mixture of water/octane/C₉ E₃ [nonyl tri(ethylene oxide)] at various temperatures, with an oil thickness of the nanoscale size.

The main goal of our work was to examine how water permeation occurs in a system with surfactant rich phases. Since there is a high energetic cost to increase the area per amphiphilic molecule at equilibrium, complex formation and transport can not be observed in equilibrated systems on the timescales available for the MD simulations, unless there is a biased force acting perpendicular to the leaflets [165–169] or a concentration gradient of a solute (ions, surfactant molecules and etc.) in the system [169, 170]. In particular, the compression or saturation of surfactant leaflets is a useful technique, allowing to create a difference of the surfactant chemical potential inside and outside the leaflet and to initiate active transport [171–173].

We chose the approach similar to the latter due to its implementational simplicity and conceptual correspondence to many experimental setups. The difference in composition creates a difference in chemical potentials of the dispersed molecules, which in turns generates osmotic pressure and a compound flux. The necessary time to achieve an equilibrium state can be quite long, however this simulation setup allows studying microscopic details about transport phenomena and relaxation dynamics in the initial response of the system.

One of our particular goals was to investigate the way surfactants mediate such water transport, since it could go through independent diffusion, inverse micelles, hydrated surfactants, or even channel formation processes. We also studied water-surfactant complexes' statistics (clustering combined with number fraction distributions) and chemical interactions (visual analysis combined with radial distribution functions). We highlight our findings in the context of prior models of water transport.

5.2 Methods

5.2.1 MD Simulation Protocol

We have built an atomistic ternary system of water/octane/C₉E₃ [nonyl tri(ethylene oxide)], with constituents placed in a desired geometry of 5 alternating layers: water/surfactant/octane/surfactant/water (see Figure 5.1). The AMBER10 [174] suit of programs was used for system initialization and all-atom MD simulations. First, we prepared octane and surfactant molecules since they do not enter the standard molecular database of AMBER10 package. To generate topology files and also to assign the general AMBER force-field (GAFF) parameters [175] for these molecules, we used the Antechamber module [176] of the AMBER10 package. Water molecules were parametrized according to the TIP3P model [177]. Initial structure of a five-layer system, with octane and surfactant molecules being perfectly aligned along z -direction, was built using the Biochemical algorithm library (BALL) [178]. The composition of the ternary mixture has been chosen to be $\%_{weight}$ water ≈ 0.301 , $\%_{weight}$ surfactant ≈ 0.327 , $\%_{weight}$ oil ≈ 0.372 . Specifically, the system was comprised of 5776 water molecules, 338 surfactant molecules and 1125 oil molecules. The the average area per surfactant molecule is $\approx 21.3 \text{ \AA}^2$, which is smaller than the equilibrium range $40 - 50 \text{ \AA}^2$ for similar surfactants. This setup allows us to observe fast response of the system, once the relaxation dynamics is started. The total number of atoms is 63,816, and the system is placed in a rectangular box having dimensions $60 \times 60 \times 160 \text{ \AA}^3$.

This is the largest all-atomistic ternary microemulsion system simulated to date [179–181].

The initial conformation was first equilibrated at $T = 500 \text{ }^\circ\text{K}$ in the NPT ensemble in order to melt the oil layers and the surfactant tails, followed by the gradual temperature decrease to $300 \text{ }^\circ\text{K}$ and subsequent switch to the NVT ensemble with total equilibration time $\approx 30 \text{ ns}$. Periodic boundary conditions were imposed in all directions. The productive run was performed by replica exchange molecular dynamics (REMD) for 42 replicas of the system in the temperature range $280 - 361 \text{ }^\circ\text{K}$ ($7 - 88 \text{ }^\circ\text{C}$). The temperature difference between neighboring replicas was $1.93 \text{ }^\circ\text{C}$, which set an average probability of an exchange to 0.33 [182]. A time range between switches was chosen to be 0.8 ps [183]. The total simulation time was $\approx 26 \text{ ns}$ for each replica, which summed up to $1 \text{ } \mu\text{s}$ for all replicas. Because of the large system size, the UNC Topsail supercomputer was used to perform simulations in the parallel regime with the 4 nodes usage per replica.

5.2.2 Cluster Analysis

To characterize water and surfactant association into the complexes of varying sizes, we implemented two clustering algorithms based on reiterative sorting procedure applied to water and surfactant molecules participating in hydrogen bonds. The first one-dimensional 1D clustering approach considered “water-water” connectivity only. Two water molecules were considered to form a link (hydrogen bond) if the distance between the oxygen (any hydrogen) of the first molecule and any hydrogen (the oxygen) of the second molecule was less or equal to a certain threshold value $l_{cl,ww}$. The second approach is technically similar yet has a different topological concept. It accounts not only for the water-water contacts, but also for the water-surfactant and surfactant-surfactant contacts, taking into account inter-molecular connectivity in the clusters. In such a way, if the distance between any two heavy atoms (oxygen or carbon) of water and surfactant or surfactant and surfactant molecules was less than $l_{cl,ws}$, the corresponding molecules were considered to be associated with each other.

The numerical values of these thresholds were set to the size of the first solvation shell for each pair of molecules ($l_{cl,ww} = 3.1 \text{ \AA}$, $l_{cl,ws} = 3.8 \text{ \AA}$). The latter was determined, in turn, from the corresponding water-water, water-surfactant, surfactant-surfactant atomistic Radial Distribution Functions (RDF).

After that, lists of links between water and surfactant molecules were used in the recursive iterations, which are briefly described below. At the first sorting, one arbitrary molecule is put to the first cluster, then all molecules linked with the chosen one (neighbors) are also added into the first cluster. At the second and the subsequent sorting cycles, all neighbors of neighbors are added into the cluster. Sorting is performed until the cluster size stops increasing. Then one of the molecules not added to the first cluster is included into the second cluster and the procedure is subsequently repeated until all water and surfactant molecules have been sorted.

As a result, the cluster size probability distribution function $P(M,N)$ was obtained by histogramming clusters with respect to their sizes (M - number of water molecules and N - number of surfactant molecules involved) and averaging this distribution over all simulation snapshots for the corresponding temperature.

We also checked how the cluster size $P(M,N)$ depends on the value of the link parameter $l_{cl,ww}$, since it was particularly important due to the relation to the “inverse micelle” water transport mechanism. Namely, if the marginal distribution of water cluster sizes $P'(M) = \sum_N P(M,N)$ showed a maximum at the $M > 1$, it would indicate that the dense water core formation commonly occurs. This, in turn, would provide strong support for the “inverse micelle” water transport model.

Clustering analysis was, therefore, performed for the following set of l_{cl} : 2.5, 2.7, 3, 3.5, 4, 5, 6, and 7 \AA , at the temperature 25 $^{\circ}\text{C}$. All resulting cluster size probability distributions $P'(M)$ have a maximum value around the unity, although, for 7 \AA $P'(M)$ showed low broad peaks (probability value less than 0.1) for some values $M > 5$. With growing value of $l_{cl,ww}$, $P'(M)$ becomes wider, but preserves its shape.

In addition to that, we calculated the average ratio $\langle M/N \rangle$ which shows how many surfactant molecules per water molecule are in a cluster. We compared $\langle M/N \rangle$ for all temperatures and found that $\langle M/N \rangle$ is conserved within the 2 – 3 range. At the same time, the maximum of $P(M, N)$ (most probable value) was found for $\langle M/N \rangle$ within the 1 – 2 range for any M and all temperatures.

5.3 Results and discussion

The preparation of the initial configuration was performed in a such way that there would be an excess of surfactant molecules in the leaflets, thus providing no energetic penalty for the surfactants to leave the layers of residence. At such circumstances it would be straightforward to expect active surfactant permeation of the oil layer, which might cause passive water transport as well. It should be noted that at the equilibrium surfactant density in the leaflets one can not observe the formation of “water-surfactant” complexes at the sub-microsecond timescales. To verify that, we constructed a microemulsion system containing a very similar $C_{10}E_4$ surfactant, water and octane with the same volume fractions, but the equilibrium value of the area per surfactant $A_0 \approx 44 \text{ \AA}^2$. Nor significant water permeation into the oil layer, neither the “water-surfactant” complex formation were observed in this system for a wide range of temperatures during $\approx 2 \mu s$ of the REMD simulations. Therefore, we suggest that the formation of such aggregates at the timescales smaller than a microsecond is provided by the non-equilibrium effects in the microemulsion system containing C_9E_3 surfactant. Accordingly, the focus of the current paper is on the C_9E_3 microemulsion system, and the extensive analysis of the equilibrium $C_{10}E_4$ microemulsion system will be presented elsewhere.

A typical MD simulation snapshot along with various water-surfactant complexes is shown in Figure 5.1. The central observation of the present study is the formation of the water-surfactant complexes in the surfactant/oil layer, as a results of relaxation dynamics of the

surfactant-rich leaflets, that primarily contain surfactant molecules along with oil molecules penetrating from the oil slab and water molecules dragged in by the surfactant molecules. We observed such aggregates at all stages of the MD simulation. Additionally, visual inspection suggested that water-surfactant complexes actively permeate surfactant and oil layers of the ternary mixture and vary in sizes.

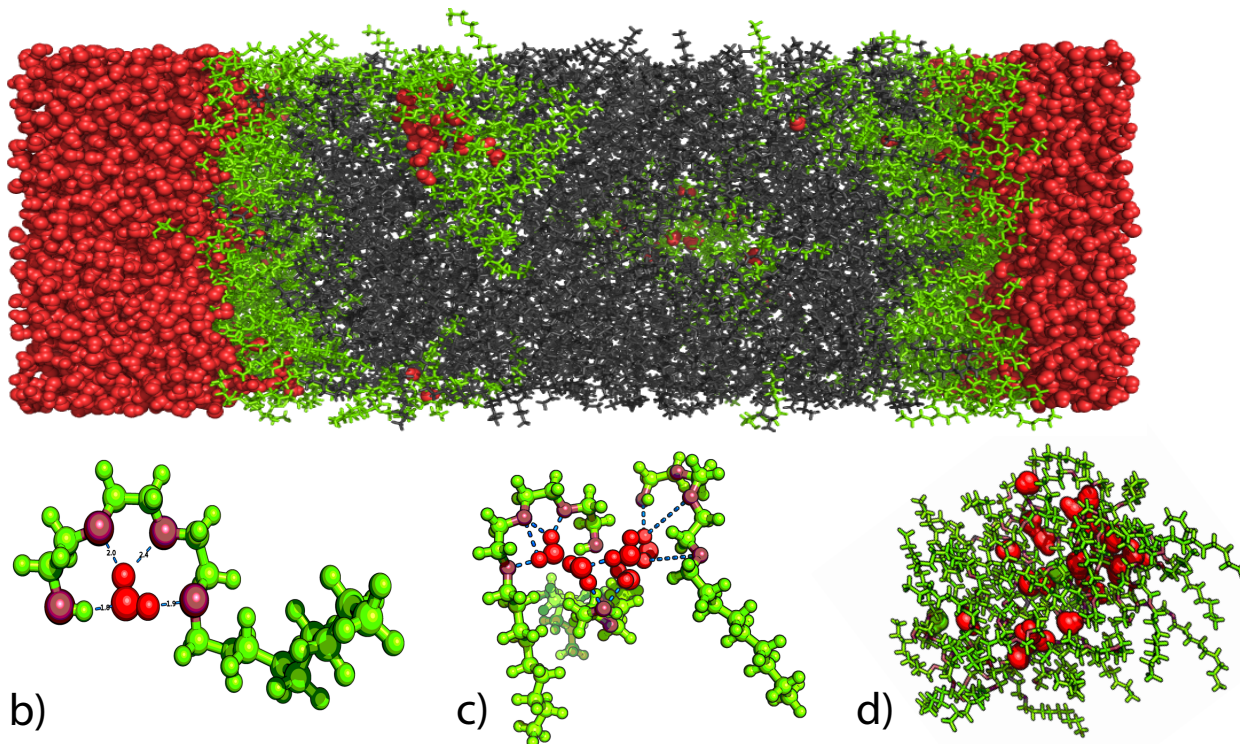


Figure 5.1: (a) A snapshot of the system in a box at $T_1=25\text{ }^\circ\text{C}$. Color scheme: water molecules are red, surfactant molecules are green, and oil molecules are grey. The water-surfactant complexes formed at the boundary of/in the oil layer can be seen. (b) A snapshot of a single surfactant molecule solvating one water molecule. Color scheme: green spheres are surfactant carbons and hydrogens; ruby spheres are surfactant oxygens; red spheres are water hydrogens and oxygens. (c) A snapshot of several surfactant molecules solvating several water molecules. The color scheme is the same as in (b). (d) A snapshot of a micellar-like aggregate, including surfactant molecules (green) and water (red). Oil molecules in (b)-(d) are removed for the lucid demonstration of the water-surfactant complexes.

Therefore, for more quantitative description of the water permeation process, we imple-

mented two clustering algorithms. First approach was based on statistical histogramming of all water clusters in the system with respect to their sizes. Two water molecules were treated as belonging to one cluster if the oxygen-hydrogen distance was less than a size of the first solvation shell, taken from corresponding radial distribution functions (see Figure 5.4). After the clustering procedure they were histogrammed by number of water molecules in a cluster, thus providing a probability distribution function $P(M)$ at a particular temperature (see Figure 5.2). It is important to mention that such one-dimensional (1D) water clustering algorithm accounts only for the water complexes that are directly connected through hydrogen bonding and does not take into account the role of surfactant molecules in these processes. As shown in Figure 5.2, the most probable size of water clusters is one, which means that the number of larger clusters is insufficient and water penetration happens mostly without dense water core formation. This observation needed further investigation to elucidate whether a single water molecule diffusion or the surfactant mediated permeation was the most probable transport mechanism.

For this reason, the second clustering algorithm has been implemented to obtain 2-dimensional cluster size probability distribution $P(M, N)$, where P is a probability to find a cluster with M waters and N surfactants. We found that $P(M, N)$ reaches a maximum for N/M ratio in the range $\approx 1 - 2$ for all M . Yet the average number of surfactants per water molecule in a cluster is $\langle N/M \rangle \approx 2 - 3$, indicating that water sharing of a surfactant polar cage commonly occurs in the complexes. Nevertheless, the marginal distribution of water cluster sizes $P'(M) = \sum_n P(M, N)$ peaks around unity as shown in Figure 5.3, hence, most of the water molecules in the oil layer prefer to aggregate with surfactant molecules (hydrated surfactants) instead of forming water clusters (dense core), surrounded by a shell of surfactant molecules, where the latter structure would correspond to inverse micelles.

To further characterize the formation of the water-surfactant complexes, we tested whether

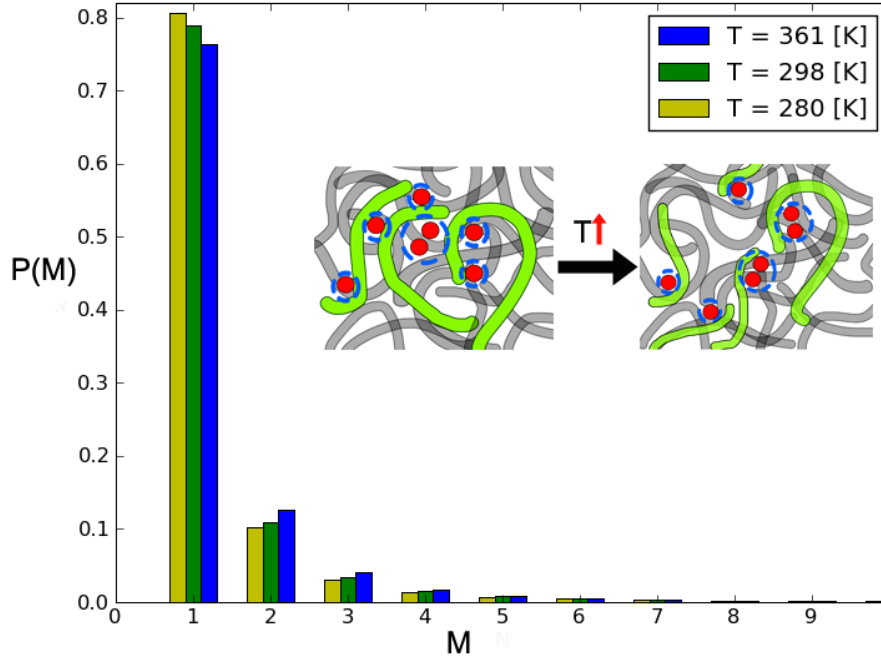


Figure 5.2: Probability distribution function $P(M)$ for one-dimensional (1D) clustering of water molecules shown for several temperatures $T = 7, 25,$ and 88°C . Most probable cluster size is given by the maximum of $P(M)$ and is equal to 1 for all temperatures. With the temperature increase, probability distribution becomes wider, suggesting that larger clusters are permitted in the hydrophobic region. This effect is partially due to the overall increase of the the water density on the oil slab. The change in the clusters' distribution with temperature provided by the visual analysis is schematically shown in the inset. Color scheme: water molecules are red, surfactant molecules are green, and oil molecules are grey. Note the difference between the clusters obtained from 1D clustering and 2D clustering (see Figure 5.3).

any specific chemical interactions are responsible for the solvation of water by surfactant molecules. We calculated a set of RDFs among various atoms of the water and surfactant molecules (e.g., water oxygens and surfactant head's terminal hydrogens). Since there can be a significant number of possible hydrogen-oxygen atom pairs in this system, we show only RDFs with the most pronounced first and second solvation peaks (see Figure 5.4).

The comparison among various RDFs revealed an interesting structural property of water -

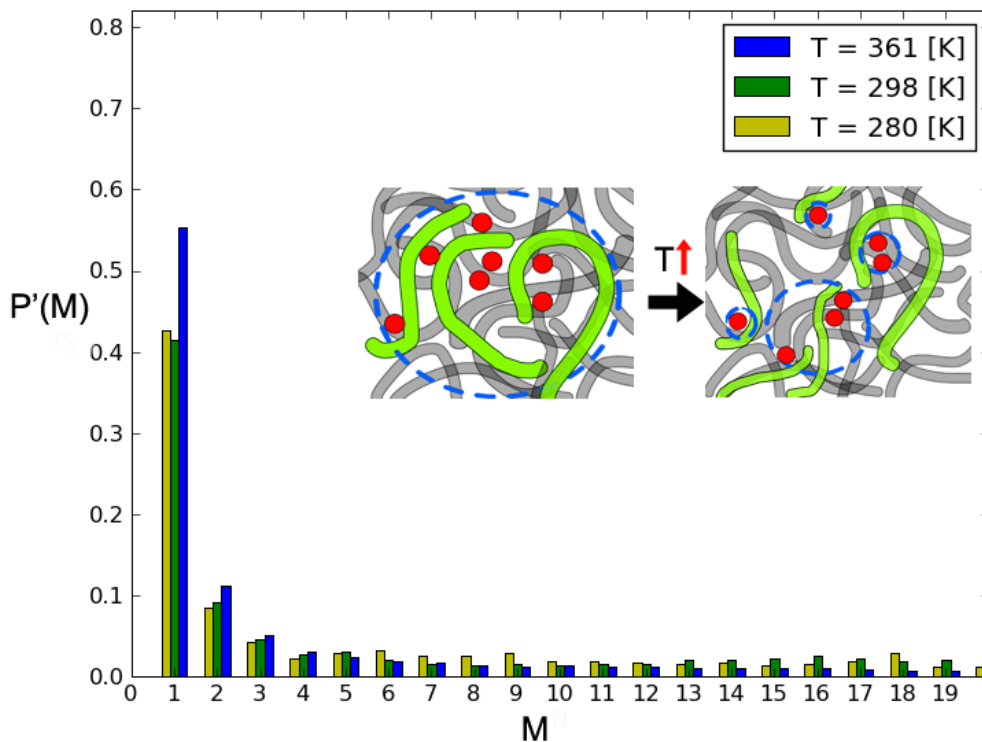


Figure 5.3: Marginal probability distribution function $P'(M)$ for two-dimensional (2D) clustering of water molecules shown for several temperatures $T = 7, 25,$ and 88°C . Most probable cluster size is given by the maximum of $P'(M)$ and is equal to 1 for all temperatures. With the temperature increase, probability distribution becomes narrower, suggesting that clusters dissociate into smaller ones in the hydrophobic region. The change in the clusters' distribution with temperature provided by the visual analysis is schematically shown in the inset. Color scheme: water molecules are red, surfactant molecules are green, and oil molecules are grey. Note the difference between the clusters obtained from 1D clustering and 2D clustering (see Figure 5.2).

surfactant complexes, namely, the hydrogen bond formation between the water oxygen and the terminal surfactant hydrogen is much more common than any other possible hydrogen bonding in the oil-surfactant layer. This is confirmed by the significantly higher first solvation peak of the “water oxygen - surfactant terminal hydrogen” RDF compared to that of all possible “water hydrogen - surfactant oxygen” RDFs in the surfactant/oil layer. This point is illustrated in the Figure 5.4 inset as well, where a typical water-surfactant complex is shown.

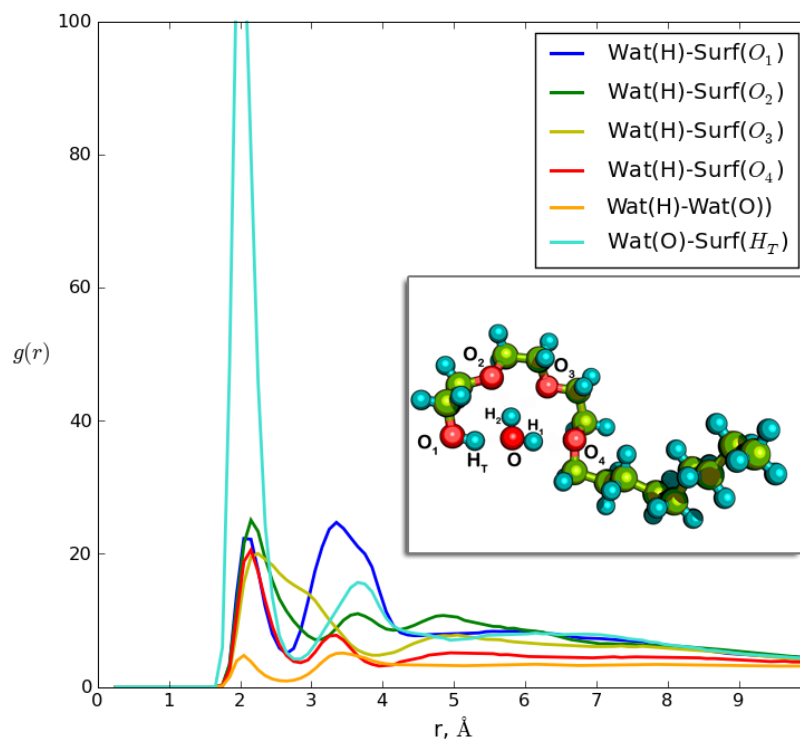


Figure 5.4: Radial Distribution Function(RDF) of various atom pairs of water and surfactant that can potentially contribute to hydrogen bond formation in the oil slab. Since our main interest is the “water-surfactant” complexes in oil, these RDFs has been computed for the molecules located in the oil layer. The notations for RDF atom pairs are shown in the inset, which is a snapshot of a “water-surfactant” complex taken from the simulations.

A discussion above suggests that the main stabilizing mechanism for the water solvation by surfactants is a hydrogen bond formation among water oxygens and the terminal hydrogens of the surfactant head groups. It is important, that the water “solvation cage” is highly dynamic, so single water molecule can be solvated by multiple surfactants or move from one polar cage to another within an aggregate, as well as share one “solvation cage” with other water molecules (see Figure 5.1 (c) and (d)).

Visual analysis of the MD simulation movie revealed another compelling observation, that large water-surfactant complexes are found at the surfactant-oil interface and do not travel

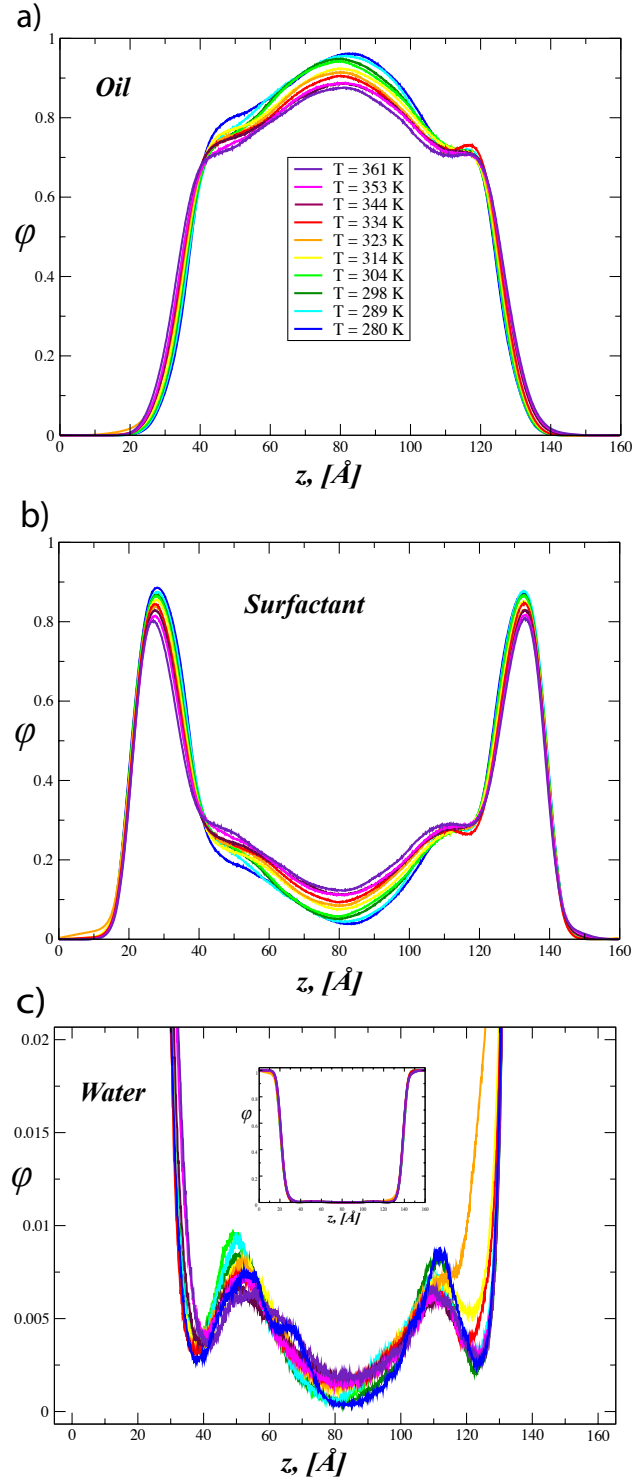


Figure 5.5: Number fraction distributions (NFD) for (a) oil, (b) surfactant, and (c) water for 10 temperatures chosen from 42 available. The subplot in (c) shows full profile of water NFD, whereas the main plot (c) shows the water profile only at low concentrations, since water presence in the oil layer is still quite low comparing to the rest of the system. The abscissa is a coordinate along the layers normal, which corresponds to a horizontal axis in Figure 5.1 (a). The ordinate is a number fraction calculated from Eq. ??.

through the oil layer unless the temperature is very high (70-80 °C). There was seemingly a two-step process of the water transportation in the microemulsion system, where at first water molecules were accumulated in water pockets located within the surfactant layers, and at second, one to several water molecules wrapped by surfactants were transported through oil to a water pocket at the opposite side. To investigate the character of water penetration into the oil-surfactant interface, the number fraction distributions (NFD) along the layer normal (z -axis) were calculated for all components:

$$\phi^j(z) = \frac{N^j(z)}{N^{wat}(z) + N^{surf}(z) + N^{oil}(z)}, \quad j = (water, surfactant, oil) \quad (5.1)$$

Oil, water and surfactant NFDs are plotted for several temperatures in the Figure 5.5. It is seen that for all temperatures there is a local increase in the water number fraction at positions $z = 50\text{\AA}$ and $z = 110\text{\AA}$, as well as an appearance of a “plateau” in surfactant concentration gradient in the range of $z \in (40-60)\text{\AA}$ and $z \in (110-130)\text{\AA}$ [see Figure 5.5(a),(b)]. Oil NFD has local minima at the same regions, where most large water-surfactant aggregates are situated (see Figure 5.1 (a),(c)).

With increasing temperature, surfactant NFD spreads out, and surfactant layers become more friable to water and oil intrusions (see Figure 5.5 (b)). The presence of the surfactant molecules in the oil layer significantly grows as expected, since non-ionic surfactants are known to become more oleophilic with the temperature increase [184]. At the same time, as temperature gets elevated, water concentration in oil increases, which is accompanied by the spreading of the “water-surfactant” complexes traveling through bulk oil (see Figure 5.5 (c)). As for oil distribution profile, it spreads out as well, and oil actively penetrates through the surfactant layers creating more direct “water-oil” contacts (see Figure 5.5 (a)).

5.4 Conclusions

MD simulations help to provide detailed microscopic information, which otherwise is quite difficult to extract from experimental or theoretical studies. In the current paper, we reported results obtained from extensive atomistic REMD simulations on a non-ionic ternary mixture water/octane/ C_9E_3 . The total simulation time in this work was near 1 microsecond, which represents by far the largest atomistic simulation of a microemulsion system to date.

We observed the non-equilibrium relaxation dynamics of the ternary system in a wide range of temperatures (7 - 88 °C) and studied the formation and transport of the water-surfactant complexes. We showed, that surfactants play a role of an effective solvent for water molecules, facilitating water transport through the oil slab. We also found that a “polar solvation cage” created by surfactant molecules is highly dynamic, so there is no specificity in hydrogen bond formation with respect to any particular surfactant oxygens. However, majority of water oxygens form a hydrogen bond with the terminal hydrogen of a surfactant head (see Figure 5.4).

One of the fascinating observations in this work is that the major amount of water solubilized by surfactant is situated in pockets on at the border between surfactant and oil layers and is not homogeneously distributed in the surfactant-oil slab (see Figure 5.5). We also detected that with increasing the temperature the larger aggregates detach from the interface and travel through the oil layer, raising overall water presence in oil.

Despite the fact that water-surfactant complexes vary in topology and sizes, our cluster analysis showed that the majority of these complexes do not form dense water cores, thus, providing evidence for the alternative “hydrated surfactants” transport mechanism [154, 158, 159] (see Figure 5.2).

It will be interesting to investigate the transport mechanisms of other species in the future work, such as weak acids or small ions, as well as their effects on water permeation. Also, calculation of such important characteristics as the diffusion, partition and permeability coefficients and their dependences on temperature would be of great fundamental as well as applied

biological and industrial interest.

Reproduced with permission from Maria Minakova, Alexey Savelyev, Garegin A Papoian,
Nonequilibrium Water Transport in a Nonionic Microemulsion System, *The Journal of*
Physical Chemistry B (2011) ,115 (20), 6503-6508

Appendix A

Supplementary information for the manuscript "Theory of Active Transport in Filopodia and Stereocilia"

A.1 Efficiency of active transport and non-monotonic profile

As mentioned in the main text, the maximum in the actin profile is pumped up by the motors, and should gradually disappear if the transport becomes less and less efficient. The actin profiles for different values of the loading rate, k_1 , (binding between a motor on filament and a G-actin monomer) are plotted Fig.A.1, clearly illustrating this effect.

A.2 The boundary conditions

The choice of the third boundary condition for the equations describing the motor profiles is a subtle issue and depends on the particular question one has in mind. This choice only has a slight effect on the solution of the equations, so it is not very important. However, it is worthwhile to discuss it for clarity purposes.

For the purely mathematical, continuous problem, where the filaments don't exist outside the tube, the appropriate boundary condition is $c_b(0) = 0$ (from which follows the $A(0) = 0$

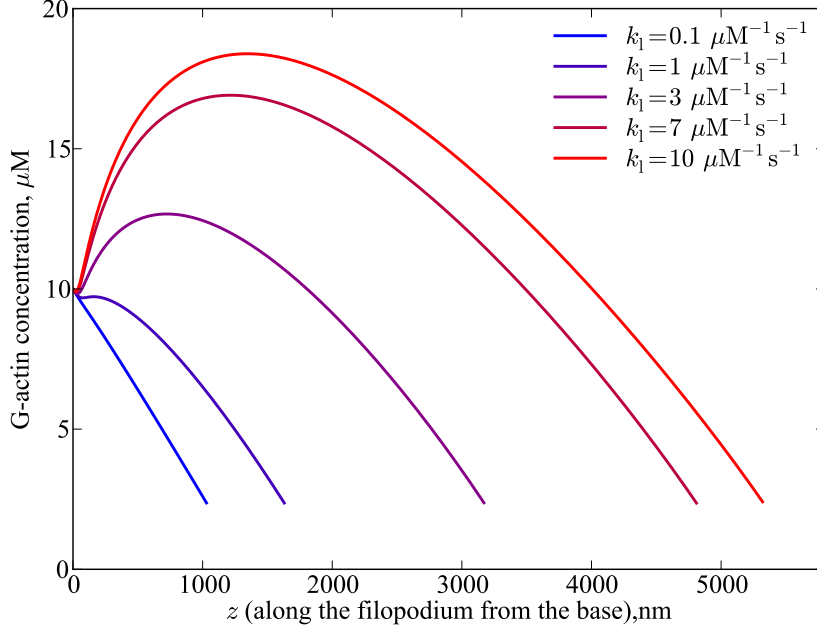


Figure A.1: One of the possible ways to influence the efficiency of transport is to change binding rate of G-actin to motors. Concentration profile changes to a monotonic when transport becomes completely inefficient.

in the actin part) and no additional assumptions (like detailed balance) are required. Indeed, if the filaments do not cross the $z = 0$ point, neither can bound motors, hence $J_b(0) = 0$, and as $J_b = v(c_b)c_b$, $c_b(0) = 0$. This argument can be presented in a more detailed way. Let us consider a small (going to infinitesimal later) volume of the tube near the base. Integrating the second of the motor equations over this volume one gets:

$$\frac{\partial J_b}{\partial z} = -k_{\text{off}}c_b + k_{\text{on}}c_f, \text{ figur} \quad (\text{A.1})$$

$$\int_0^{\delta z} \frac{\partial J_b}{\partial z} dx dy dz = \int_0^{\delta z} (-k_{\text{off}}c_b + k_{\text{on}}c_f) dx dy dz, \quad (\text{A.2})$$

$$(J_b(0 + \delta z) - J_b(0+))S_f = (-k_{\text{off}}c_b(\alpha\delta z) + k_{\text{on}}c_f(\alpha\delta z))S_f\delta z, \quad (\text{A.3})$$

where S_f is cross-section of the filopodium and $0 \leq \alpha \leq 1$.

Since $J_b(0+) = 0$,

$$J_b(0 + \delta z)S_f = (-k_{\text{off}}c_b(\alpha\delta z) + k_{\text{on}}c_f(\alpha\delta z))S_f\delta z, \quad (\text{A.4})$$

$$\lim_{\delta z \rightarrow 0} J_b(\delta z) = \lim_{\delta z \rightarrow 0} (-k_{\text{off}}c_b(\alpha\delta z) + k_{\text{on}}c_f(\alpha\delta z))\delta z = 0, \quad (\text{A.5})$$

and as $J_b = v(c_b)c_b$, one can conclude that $\lim_{\delta z \rightarrow 0} c_b(\delta z) = 0$ and use the boundary condition

$$c_b(0) = 0. \quad (\text{A.6})$$

In our simulations, however, the space is split into compartments, and the concentration profiles are not continuous, and the first point corresponds to the first compartment, which spans 54 nm starting from $z = 0$. It is not obvious how to directly compare the simulation results with continuous analytical curves at $z = 0$. To compare one should take average of the analytical curve over the first 54 nm and using it as $c_b(0)$ and solve the equations again. Alternatively, one can assume detailed balance between c_f and c_b at $z = 0$ (and between c_b and A in the actin equations), which turns out to be a good approximation.

In real filopodia the filaments continue into the cell bulk (unlike our simulations), making the $c_b = 0$ condition of the formal problem less relevant. Detailed balance in the cell bulk, on the other hand, is a plausible assumption as a first approximation. The next approximation would require modeling of the filaments with motors in the bulk (the lamellipodium) explicitly.

Thus, the detailed balance BCs are more interesting and relevant for the physical problem, so they are the ones used in the paper. However, it turns out that both alternative BCs lead to almost indistinguishable results, except for the very beginning of the concentration profiles. To demonstrate this, we plotted below the graphs corresponding to the solution of the formal

mathematical problem, with no additional assumptions, and the $c_b(0) = 0$ boundary condition (Figs. S3.2-S3.6).

A.3 Detailed balance in the motor part

Seeing how soon the detailed balance is established with the $c_b(0) = 0$ boundary condition, one may be prompted to see what will happen, if one assumes detailed balance between motor binding to the filaments and falling off along the whole tube, that is

$$k_{\text{off}}c_b = k_{\text{on}}(1 - c_b/c_s)c_f \quad (\text{A.7})$$

for all z . In this case, both JMM equations trivialize and uncouple, which does not make much physical sense. However, the conservation law for the total flux, $J_b + J_f = 0$ turns out to retain its meaning, and after substituting c_f from the detailed balance condition yields an equation for c_b :

$$-Dc'_f + c_b(v(1 - c_b/c_s) - v_r) = 0, \quad (\text{A.8})$$

$$c_f = \frac{k_{\text{off}}}{k_{\text{on}}} \frac{c_b}{1 - c_b/c_s}, c'_f = \frac{k_{\text{off}}}{k_{\text{on}}} \frac{c'_b}{(1 - c_b/c_s)^2} \quad (\text{A.9})$$

$$c'_b = \frac{k_{\text{on}}}{k_{\text{off}}D} c_b(1 - c_b/c_s)^2 (v(1 - c_b/c_s) - v_r). \quad (\text{A.10})$$

Using notation $b = c_b/c_s$, $r = v_r/v$, we rewrite the equation as

$$b' = \frac{k_{\text{on}}v}{k_{\text{off}}D} b(1 - b)^2(1 - b - r). \quad (\text{A.11})$$

The variables are separated, so one can integrate the equation:

$$z + C = \frac{k_{\text{off}} D}{k_{\text{on}} v_r} \left[\frac{\log \frac{b r^2 (1-b)(1-r^2)}{1-r-b}}{r(1-r)} - \frac{1}{1-b} \right]. \quad (\text{A.12})$$

Taking into account the boundary condition

$$b(z) \Big|_{z=0} = b_0 = c_b(0)/c_s = \frac{k_{\text{on}} c_f(0)}{k_{\text{off}} c_s + k_{\text{on}} c_f(0)}, \quad (\text{A.13})$$

one obtains the solution:

$$z = \frac{k_{\text{off}} D}{k_{\text{on}} v_r} \left[\frac{\log \left[\left(\frac{b(1-b_0)}{b_0(1-b)} \right)^{r^2} \frac{(1-b)(1-r-b_0)}{(1-b_0)(1-r-b)} \right]}{r(1-r)} - \frac{b-b_0}{(1-b)(1-b_0)} \right]. \quad (\text{A.14})$$

A.4 G-actin profiles and experiments

While motor profiles within our model are universal (independent of length), G-actin profiles will obviously be different for different lengths. In fact, G-actin profile sets up the stationary length. However, at stationary length, they will have common features (provided there is no special mechanisms additional to those we consider in this work): negative slopes at the base and at the tip, concentration at the tip such that polymerization balances the retrograde flow. The (de)polymerization rates k^+ and k^- depend on the membrane stress, which can depend on the length, adding a correction to the Eq. 6 in the main text. However, to the first approximation of the straight tube, the membrane force does not depend on the length [185]

Experimental observation of G-actin profiles in filopodia is complicated, mainly, because of the presence of large amounts of F-actin. There are techniques to discriminate between the two, like labeling only small fraction of actin or labeling DNase I, which only binds to G-actin but not F-actin [186]. Hopefully, the latter can achieve sufficient spatial resolution for

obtaining the profiles in the narrow tube full of F-actin like a filopodium or a stereocilium.

A.5 More connections to experiments

Apart from the decrease in the effective motor speed due to traffic jamming, the ATP hydrolysis rate itself (by an individual motor) can decrease due to autophosphorylation, as the local motor concentration increases [44, 187].

There is no direct experimental evidence of G-actin monomers being transported by either Myosin III or Myosin X, but these motors do carry espin1 and Ena/VASP respectively. Both espin1 and Ena/VASP have actin-binding domains, which prompts a plausible suggestion that they may be serving as “delivery devices”, or adaptors, or scaffolds, between the motor and G-actin. We investigated this possibility in our previous work on active transport in filopodia, for Ena/VASP and Myosin X (the framework is general, however, and equally applies to espin1 and Myosin IIIa) [48]. Presence of espin1 promotes elongation of the filopodia [44, 188], although it may be due to its anti-capping and polymerization-promoting functionality rather than active G-actin delivery. Ena/VASP is known to have an anti-capping role.

A.6 Retrograde flow

The retrograde flow plays an important role in setting up the stationary length, as it defines the actin flux through the filopodial cross-section (or, rather two equal fluxes with opposite signs). In the model reported in this work, we use a constant retrograde flow speed, which depends neither on polymerization, nor on various protein concentrations. In reality, the retrograde flow rate can be influenced by many factors both in the cell bulk (active machinery pulling filaments back; rearrangements and filament degradation in lamellipodia) or in filopodia itself, like focal adhesions [57], or force from the membrane acting on a filament

which is polymerizing against it. We investigated the coupling between the retrograde flow and polymerization in our previous work (reported in the corresponding Supplemental Information) [48]. This coupling can be easily taken into account in the mean-field sense, where the results are in close agreement with more detailed stochastic simulations that allow for the retrograde flow fluctuations. In this work we focused on the phenomena brought in by molecular motors inside the filopodium, and, hence, chose in favor of a simpler model where the retrograde flow is simply held constant and does not depend on other parameters and processes. This assumption can be released in a straightforward manner, if needed.

Appendix B

Supplementary videos for Chapter 4

Movie 1: https://www.sugarsync.com/pf/D7478901_65513735_0706

Movie 2: https://www.sugarsync.com/pf/D7478901_65513735_0709

Movie 3: https://www.sugarsync.com/pf/D7478901_65513735_0703

Movie 4: https://www.sugarsync.com/pf/D7478901_65513735_0717

Movie 5: https://www.sugarsync.com/pf/D7478901_65513735_0719

Movie 6: https://www.sugarsync.com/pf/D7478901_65513735_0711

Bibliography

- [1] Berendsen HJC (2007) *Simulating The Physical World: Hierarchical Modeling from Quantum Mechanics to Fluid Dynamics* (Cambridge University Press).
- [2] Peliti L (2011) *Statistical Mechanics in a Nutshell* ed Epstein M (Princeton University Press).
- [3] Ivo Sachs, Siddhartha Sen JCS (2006) *Elements of Statistical Mechanics: With an Introduction to Quantum Field Theory And Numerical Simulation* (Cambridge University Press).
- [4] Yeung T, et al. (2005) Effects of substrate stiffness on cell morphology, cytoskeletal structure, and adhesion. *Cell Motil Cytoskeleton* 60:24–34.
- [5] Chiu WT, Tang MJ, Jao HC, Shen MR (2008) Soft substrate up-regulates the interaction of stim1 with store-operated ca2+ channels that lead to normal epithelial cell apoptosis. *Mol Biol Cell* 19:2220–30.
- [6] Geiger B, Spatz JP, Bershadsky AD (2009) Environmental sensing through focal adhesions. *Nat Rev Mol Cell Bio* 10:21–33.
- [7] Gardel ML, Schneider IC, Aratyn-Schaus Y, Waterman CM (2010) Mechanical integration of actin and adhesion dynamics in cell migration.
- [8] Gardel ML, et al. (2008) Traction stress in focal adhesions correlates biphasically with actin retrograde flow speed. *J Cell Biol* 183:999–1005.
- [9] Chan CE, Odde DJ (2008) Traction dynamics of filopodia on compliant substrates. *Science* 322:1687–1691.
- [10] Sabass B, Schwarz US (2010) Modeling cytoskeletal flow over adhesion sites: competition between stochastic bond dynamics and intracellular relaxation. *J Phys-Condens Mat* 22:194112.
- [11] Petit V, Thiery JP (2000) Focal adhesions: structure and dynamics. *Biol Cell* 92:477–94.
- [12] Evans EA, Calderwood DA (2007) Forces and bond dynamics in cell adhesion.
- [13] Mattila PK, Lappalainen P (2008) Filopodia: molecular architecture and cellular functions.
- [14] Lan Y, Papoian GA (2008) The stochastic dynamics of filopodial growth. *Biophysical Journal* 94:3839–52.
- [15] Rifkin JL, Speisman RA (1976) Filamentous extensions of vegetative amoebae of the cellular slime mold dictyostelium. *Trans Am Microsc Soc* 95:165–73.
- [16] Gustafson T, Wolpert L (1999) Studies on the cellular basis of morphogenesis in the sea urchin embryo. directed movements of primary mesenchyme cells in normal and vegetalized larvae. *Exp Cell Res* 253:288–95.
- [17] Miller J, Fraser SE, McClay D (1995) Dynamics of thin filopodia during sea urchin gastrulation. *Development* 121:2501–11.
- [18] Zhuravlev PI, Papoian GA (2011) Protein fluxes along the filopodium as a framework for understanding the growth-retraction dynamics: The interplay between diffusion and active transport. *Cell Adh Migr* 5:448–56.

- [19] Keren K, Yam PT, Kinkhabwala A, Mogilner A, Theriot JA (2009) Intracellular fluid flow in rapidly moving cells. *Nat Cell Biol* 11:1219–24.
- [20] Lin CH, Espreafico EM, Mooseker MS, Forscher P (1996) Myosin drives retrograde f-actin flow in neuronal growth cones. *Neuron* 16:769–82.
- [21] Kasza KE, Zallen JA (2011) Dynamics and regulation of contractile actin-myosin networks in morphogenesis. *Curr Opin Cell Biol* 23:30–8.
- [22] Medeiros NA, Burnette DT, Forscher P (2006) Myosin ii functions in actin-bundle turnover in neuronal growth cones. *Nat Cell Biol* 8:215–26.
- [23] Sens P, Turner MS (2006) Budded membrane microdomains as tension regulators. *Phys Rev E Stat Nonlin Soft Matter Phys* 73:031918.
- [24] Parton RG, Simons K (2007) The multiple faces of caveolae. *Nat Rev Mol Cell Bio* 8:185–94.
- [25] Tyska MJ, et al. (1999) Two heads of myosin are better than one for generating force and motion. *P Natl Acad Sci Usa* 96:4402–7.
- [26] Takagi Y, Homsher EE, Goldman YE, Shuman H (2006) Force generation in single conventional actomyosin complexes under high dynamic load. *Biophysical Journal* 90:1295–307.
- [27] Peskin CS, Odell GM, Oster GF (1993) Cellular motions and thermal fluctuations: the brownian ratchet. *Biophysical Journal* 65:316–24.
- [28] Mogilner A, Rubinstein B (2005) The physics of filopodial protrusion. *Biophysical Journal* 89:782–95.
- [29] Lele TP, Thodeti CK, Pendse J, Ingber DE (2008) Investigating complexity of protein-protein interactions in focal adhesions. *Biochem Bioph Res Co* 369:929–934.
- [30] van Kampen NG (1992) Stochastic processes in physics and chemistry. *Stochastic Processes in Physics and Chemistry (Revised and enlarged edition)* Publisher: Elsevier Science.
- [31] Andrews, S S, Dinh T, Arkin AP (2009) *Stochastic models of biological processes* ed Meyers R (Springer, NY) Vol. 9, pp 8730–8749.
- [32] Gillespie DT (2007) Stochastic simulation of chemical kinetics. *Annu Rev Phys Chem* 58:35–55.
- [33] Atilgan E, Wirtz D, Sun SX (2006) Mechanics and dynamics of actin-driven thin membrane protrusions. *Biophysical Journal* 90:65–76.
- [34] Li F, Redick SD, Erickson HP, Moy VT (2003) Force measurements of the alpha5beta1 integrin-fibronectin interaction. *Biophysical Journal* 84:1252–62.
- [35] Raucher D, Sheetz MP (1999) Characteristics of a membrane reservoir buffering membrane tension. *Biophysical Journal* 77:1992–2002.
- [36] Merkel R, Nassoy P, Leung A, Ritchie K, Evans E (1999) Energy landscapes of receptor-ligand bonds explored with dynamic force spectroscopy. *Nature* 397:50–3.
- [37] Patla I, et al. (2010) Dissecting the molecular architecture of integrin adhesion sites by cryo-electron tomography. *Nat Cell Biol* 12:909–15.
- [38] Craig EM, Goor DV, Forscher P, Mogilner A (2012) Membrane tension, myosin force, and actin turnover maintain actin treadmill in the nerve growth cone. *Biophysical Journal* 102:1503–13.
- [39] Thomas WE (2009) Mechanochemistry of receptor-ligand bonds. *Curr Opin Struct Biol* 19:50–5.
- [40] Bagnard D, ed (2007) *Axon Growth and Guidance*, Advances in Experimental Medicine and Biology (Springer) Vol. 621.
- [41] Riedel-Kruse IH, Hilfinger A, Howard J, Jülicher F (2007) How molecular motors shape the flagellar beat. *HFSP Journal* 1:192–208.

- [42] Sousa AD, Cheney RE (2005) Myosin-X: a molecular motor at the cell's fingertips. *Trends in cell biology* 15:533–539.
- [43] Prost J, Barbetta C, Joanny JF (2007) Dynamical control of the shape and size of stereocilia and microvilli. *Biophys J* 93:1124–1133.
- [44] Salles FT, et al. (2009) Myosin IIIa boosts elongation of stereocilia by transporting espin 1 to the plus ends of actin filaments. *Nature cell biology* 11:443–450.
- [45] Hänggi P, Marchesoni F (2009) Artificial Brownian motors: Controlling transport on the nanoscale. *Reviews Of Modern Physics* 81:387–442.
- [46] Wang S, Wolynes PG (2011) On the spontaneous collective motion of active matter. *Proceedings of the National Academy of Sciences of the United States of America* 108:15184–15189.
- [47] Lan Y, Papoian GA (2008) The stochastic dynamics of filopodial growth. *Biophys J* 94:3839–3852.
- [48] Zhuravlev PI, Der BS, Papoian GA (2010) Design of active transport must be highly intricate: a possible role of myosin and Ena/VASP for G-actin transport in filopodia. *Biophys J* 98:1439–1448.
- [49] Manor U, Kachar B (2008) Dynamic length regulation of sensory stereocilia. *Seminars in cell & developmental biology* 19:502–510.
- [50] Miller J, Fraser SE, McClay D (1995) Dynamics of thin filopodia during sea urchin gastrulation. *Development* 121:2501–2511.
- [51] Zhuravlev PI, Papoian GA (2011) Protein fluxes along the filopodium as a framework for understanding the growth-retraction dynamics: The interplay between diffusion and active transport. *Cell Adhesion and Migration* 5:448–456.
- [52] Sheetz MP, Wayne DB, Pearlman AL (1992) Extension of filopodia by motor-dependent actin assembly. *Cell Motil Cytoskeleton* 22:160–169.
- [53] McGrath JL, Tardy Y, Dewey CF, Meister JJ, Hartwig JH (1998) Simultaneous measurements of actin filament turnover, filament fraction, and monomer diffusion in endothelial cells. *Biophys J* 75:2070–2078.
- [54] Novak IL, Slepchenko BM, Mogilner A (2008) Quantitative Analysis of G-Actin Transport in Motile Cells. *Biophysical Journal* 95:1627–1638.
- [55] Pollard TD (1986) Rate constants for the reactions of ATP- and ADP-actin with the ends of actin filaments. *J Cell Biol* 103:2747–2754.
- [56] Kovar DR (2007) Intracellular motility: myosin and tropomyosin in actin cable flow. *Current Biology* 17:R244–R247.
- [57] Chan CE, Odde DJ (2008) Traction dynamics of filopodia on compliant substrates. *Science (New York, NY)* 322:1687–1691.
- [58] Sept D, Xu J, Pollard TD, McCammon JA (1999) Annealing accounts for the length of actin filaments formed by spontaneous polymerization. *Biophys J* 77:2911–2919.
- [59] Naoz M, Manor U, Sakaguchi H, Kachar B, Gov NS (2008) Protein localization by actin treadmilling and molecular motors regulates stereocilia shape and treadmilling rate. *Biophys J* 95:5706–5718.
- [60] Parmeggiani A, Franosch T, Frey E (2004) Totally asymmetric simple exclusion process with Langmuir kinetics. *Physical Review E* 70:046101.
- [61] Manor U, et al. (2011) Regulation of stereocilia length by myosin XVa and whirlin depends on the actin-regulatory protein Eps8. *Current Biology* 21:167–172.
- [62] Jolly AL, et al. (2010) Kinesin-1 heavy chain mediates microtubule sliding to drive changes in cell shape. *Proceedings of the National Academy of Sciences of the United States of America* 107:12151–12156.

- [63] Gumy LF, Tan CL, Fawcett JW (2010) The role of local protein synthesis and degradation in axon regeneration. *Experimental neurology* 223:28–37.
- [64] Lan Y, Wolynes PG, Papoian GA (2006) A variational approach to the stochastic aspects of cellular signal transduction. *Journal Of Chemical Physics* 125:124106.
- [65] Sasai M, Wolynes PG (2003) Stochastic gene expression as a many-body problem. *Proceedings of the National Academy of Sciences of the United States of America* 100:2374–2379.
- [66] Muller M, Klumpp S, Lipowsky R (2005) Molecular motor traffic in a half-open tube. *Journal Of Physics-Condensed Matter* 17:S3839–S3850.
- [67] Howard J, Coy DL, Hancock WO, Wagenbach M (1999) Kinesin's tail domain is an inhibitory regulator of the motor domain. *Nature cell biology* 1:288–292.
- [68] Grant BJ, et al. (2011) Electrostatically biased binding of Kinesin to microtubules. *PLoS biology* 9:e1001207.
- [69] Lan Y, Papoian GA (2006) The interplay between discrete noise and nonlinear chemical kinetics in a signal amplification cascade. *Journal Of Chemical Physics* 125:154901.
- [70] Modchang C, et al. (2010) A comparison of deterministic and stochastic simulations of neuronal vesicle release models. *Physical Biology* 7:026008.
- [71] Feng H, Han B, Wang J (2011) Adiabatic and non-adiabatic non-equilibrium stochastic dynamics of single regulating genes. *J Phys Chem B* 115:1254–1261.
- [72] Astruc D, Boisselier E, Ornelas C (2010) Dendrimers designed for functions: From physical, photophysical, and supramolecular properties to applications in sensing, catalysis, molecular electronics, photonics, and nanomedicine. *Chemical Reviews* 110:1857–1959 Astruc, Didier Boisselier, Elodie Ornelas, Catia.
- [73] Drain C, Varotto A, Radivojevic I (2009) Self-organized porphyrinic materials. *Chemical Reviews* 109:1630–1658.
- [74] Szacilowski K (2008) Digital information processing in molecular systems. *Chemical Reviews* 108:3481–3548 Szacilowski, Konrad.
- [75] Hoeben F, Jonkheijm P, Meijer E, Schenning A (2005) About supramolecular assemblies of pi-conjugated systems. *Chemical Reviews* 105:1491–1546.
- [76] Lakowicz J (2006) *Principles of Fluorescence Spectroscopy*.
- [77] McDonagh C, Burke C, MacCraith B (2008) Optical chemical sensors. *Chemical Reviews* 108:400–422.
- [78] Meyer T (1989) Chemical approaches to artificial photosynthesis. *Accounts of Chemical Research* 22:163–170 Meyer, tj.
- [79] Alstrum-Acevedo J, Brennaman M, Meyer T (2005) Chemical approaches to artificial photosynthesis. 2. *Inorganic Chemistry* 44:6802–6827 Alstrum-Acevedo, JH Brennaman, MK Meyer, TJ.
- [80] Gust D, Moore T, Moore A (2009) Solar fuels via artificial photosynthesis. *Accounts of Chemical Research* 42:1890–1898 Gust, Devens Moore, Thomas A. Moore, Ana L.
- [81] Gust D, Moore T (1989) Mimicking photosynthesis. *Science* 244:35–41 Gust, d moore, ta.
- [82] Du P, Schneider J, Luo G, Brennessel W, Eisenberg R (2009) Visible light-driven hydrogen production from aqueous protons catalyzed by molecular cobaloxime catalysts. *Inorganic Chemistry* 48:4952–4962.
- [83] Youngblood W, Lee S, Maeda K, Mallouk T (2009) Visible light water splitting using dye-sensitized oxide semiconductors. *Accounts of Chemical Research* 42:1966–1973.
- [84] Bonchio M, Carofiglio T, Carraro M, Fornasier R, Tonellato U (2002) Efficient sensitized photooxygenation in water by a porphyrin-cyclodextrin supramolecular complex. *Organic Letters* 4:4635–4637.

- [85] Hsiao J, et al. (1996) Soluble synthetic multiporphyrin arrays .2. photodynamics of energy-transfer processes. *Journal of the American Chemical Society* 118:11181–11193 Times Cited: 258.
- [86] Wagner R, Lindsey J (1994) A molecular photonic wire. *Journal of the American Chemical Society* 116:9759–9760 Times Cited: 400.
- [87] Song H, et al. (2009) Excited-state energy flow in phenylene-linked multiporphyrin arrays. *J Phys Chem B* 113:8011–8019 Times Cited: 5.
- [88] Bellows D, et al. (2010) Through-bond versus through-space t(1) energy transfers in organometallic compound-metalloporphyrin pigments. *Organometallics* 29:317–325 Times Cited: 4.
- [89] Jones W, Baxter S, Strouse G, Meyer T (1993) Intrastrand electron and energy transfer between polypyridyl complexes on a soluble polymer. *Journal of the American Chemical Society* 115:7363–7373 Jones, we baxter, sm strouse, gf meyer, tj.
- [90] Dupray L, Meyer T (1996) Synthesis and characterization of amide-derivatized, polypyridyl-based metallopolymer. *Inorganic Chemistry* 35:6299–6307 Dupray, LM Meyer, TJ.
- [91] Dupray L, Devenney M, Striplin D, Meyer T (1997) An antenna polymer for visible energy transfer. *Journal of the American Chemical Society* 119:10243–10244 Yd320 Times Cited:68 Cited References Count:14.
- [92] Friesen D, Kajita T, Danielson E, Meyer T (1998) Preparation and photophysical properties of amide-linked, polypyridylruthenium-derivatized polystyrene. *Inorganic Chemistry* 37:2756–2762 Friesen, DA Kajita, T Danielson, E Meyer, TJ.
- [93] Fleming C, Maxwell K, DeSimone J, Meyer T, Papanikolas J (2001) Ultrafast excited-state energy migration dynamics in an efficient light-harvesting antenna polymer based on ru(ii) and os(ii) polypyridyl complexes. *Journal of the American Chemical Society* 123:10336–10347.
- [94] Sowash G, Webber S (1988) Photophysics of block copolymers of 2-vinylnaphthalene and vinylidiphenylanthracene: unidirectional energy transfer. *Macromolecules* 21:1608–1611 Sowash, gg webber, se.
- [95] Webber S (1990) Photon-harvesting polymers. *Chemical Reviews* 90:1469–1482 Webber, se.
- [96] Marcaccio M, et al. (1999) Electrochemistry of multicomponent systems, redox series comprising up to 26 reversible reduction processes in polynuclear ruthenium(ii) bipyridine-type complexes. *Journal of the American Chemical Society* 121:10081–10091.
- [97] Campagna S, et al. (1995) Dendrimers of nanometer size based on metal complexes: Luminescent and redox-active polynuclear metal complexes containing up to twenty-two metal centers. *Chemistry-a European Journal* 1:211–221.
- [98] Patten PV, Shreve A, Lindsey J, Donohoe R (1998) Energy-transfer modeling for the rational design of multiporphyrin light-harvesting arrays. *J Phys Chem B* 102:4209–4216 Van Patten, PG Shreve, AP Lindsey, JS Donohoe, RJ.
- [99] Xu Z, Moore J (1994) Design and synthesis of a convergent and directional molecular antenna. *Acta Polymerica* 45:83–87 Xu, zf moore, js.
- [100] Balzani V, et al. (1998) Designing dendrimers based on transition metal complexes. light-harvesting properties and predetermined redox patterns. *Accounts of Chemical Research* 31:26–34.
- [101] Tsukube H, Suzuki Y, Paul D, Kataoka Y, Shinoda S (2007) Dendrimer container for anion-responsive lanthanide complexation and "on-off" switchable near-infrared luminescence. *Chemical Communications* pp 2533–2535.
- [102] Stapert H, Nishiyama N, Jiang D, Aida T, Kataoka K (2000) Polyion complex micelles encapsulating light-harvesting ionic dendrimer zinc porphyrins. *Langmuir* 16:8182–8188.

- [103] Ahn T, Thompson A, Bharathi P, Muller A, Bardeen C (2006) Light-harvesting in carbonyl-terminated phenylacetylene dendrimers: The role of delocalized excited states and the scaling of light-harvesting efficiency with dendrimer size. *Journal of Physical Chemistry B* 110:19810–19819.
- [104] Nantalaksakul A, Reddy D, Bardeen C, Thayumanavan S (2006) Light harvesting dendrimers. *Photosynthesis Research* 87:133–150.
- [105] Larsen J, et al. (2007) Extending the light-harvesting properties of transition-metal dendrimers. *Chemphyschem* 8:2643–2651.
- [106] Andersson J, et al. (2004) New paradigm of transition metal polypyridine complex photochemistry. *Faraday Discussions* 127:295–305.
- [107] Thomas K, Thompson A, Sivakumar A, Bardeen C, Thayumanavan S (2005) Energy and electron transfer in bifunctional non-conjugated dendrimers. *Journal of the American Chemical Society* 127:373–383.
- [108] Giansante C, et al. (2011) White-light-emitting self-assembled nanofibers and their evidence by microspectroscopy of individual objects. *Journal of the American Chemical Society* 133:316–325 Times Cited: 2.
- [109] Babu S, Kartha K, Ajayaghosh A (2010) Excited state processes in linear pi-system-based organogels. *Journal of Physical Chemistry Letters* 1:3413–3424 Times Cited: 8.
- [110] Ajayaghosh A, Praveen V, Vijayakumar C (2008) Organogels as scaffolds for excitation energy transfer and light harvesting. *Chemical Society Reviews* 37:109–122 Times Cited: 165.
- [111] Bhattacharya S, Samanta S (2009) Soft functional materials induced by fibrillar networks of small molecular photochromic gelators. *Langmuir* 25:8378–8381 Times Cited: 16.
- [112] Ferreira K, Iverson T, Maghlaoui K, Barber J, Iwata S (2004) Architecture of the photosynthetic oxygen-evolving center. *Science* 303:1831–1838 Times Cited: 1285.
- [113] Hurley D, Tor Y (1998) Metal-containing oligonucleotides: Solid-phase synthesis and luminescence properties. *Journal of the American Chemical Society* 120:2194–2195 Times Cited: 111.
- [114] Hurley D, Tor Y (2002) Donor/acceptor interactions in systematically modified ru-ii-os-ii oligonucleotides. *Journal of the American Chemical Society* 124:13231–13241 Times Cited: 43.
- [115] Hurley D, Tor Y (2002) Ru(ii) and os(ii) nucleosides and oligonucleotides: Synthesis and properties. *Journal of the American Chemical Society* 124:3749–3762 Times Cited: 68.
- [116] Holmlin R, Tong R, Barton J (1998) Long-range triplet energy transfer between metallointercalators tethered to dna: Importance of intercalation, stacking, and distance. *Journal of the American Chemical Society* 120:9724–9725 Times Cited: 41.
- [117] Channon K, Devlin G, MacPhee C (2009) Efficient energy transfer within self-assembling peptide fibers: A route to light-harvesting nanomaterials. *Journal of the American Chemical Society* 131:12520–+ Times Cited: 13.
- [118] Nam Y, et al. (2010) Virus-templated assembly of porphyrins into light-harvesting nanoantennae. *Journal of the American Chemical Society* 132:1462–+ Times Cited: 19.
- [119] Stryer L, Haugland R (1967) Energy transfer: a spectroscopic ruler. *Proceedings of the National Academy of Sciences of the United States of America* 58:719–& Times Cited: 948.
- [120] Pispisa B, Venanzi M, Palleschi A, Zanotti G (1994) Intramolecular electronic energy transfer between naphthalene and protoporphyrin chromophores bound to sequential peptides. *Macromolecules* 27:7800–7808 Times Cited: 26.
- [121] McGimpsey W, Chen L, Carraway R, Samaniego W (1999) Singlet-singlet and triplet-triplet energy transfer in bichromophoric peptides. *Journal of Physical Chemistry A* 103:6082–6090 Times Cited: 27.

- [122] Sahoo H, Roccatano D, Hennig A, Nau W (2007) A 10-angstrom spectroscopic ruler applied to short polyprolines. *Journal of the American Chemical Society* 129:9762–9772 Times Cited: 18.
- [123] Mecklenburg S, Peek B, Erickson B, Meyer T (1991) Photoinduced electron transfer in redox-active lysines. *Journal of the American Chemical Society* 113:8540–8542 Times Cited: 54.
- [124] Mecklenburg S, et al. (1993) Photoinduced electron transfer in amino acid assemblies. *Journal of the American Chemical Society* 115:5479–5495 Times Cited: 107.
- [125] McCafferty D, et al. (1995) Synthesis of redoxderivatives of lysine and their use in solid-phase synthesis of a light-harvesting peptide. *Tetrahedron* 51:1093–1106 Times Cited: 74.
- [126] Kozlov G, Ogawa M (1997) Electron transfer across a peptide-peptide interface within a designed metalloprotein. *Journal of the American Chemical Society* 119:8377–8378 Times Cited: 23.
- [127] Kornilova A, Wishart J, Ogawa M (2001) Effect of surface charges on the rates of intermolecular electron-transfer between de novo designed metalloproteins. *Biochemistry* 40:12186–12192 Times Cited: 15.
- [128] Kornilova A, et al. (2000) Design and characterization of a synthetic electron-transfer protein. *Journal of the American Chemical Society* 122:7999–8006 Times Cited: 37.
- [129] Fedorova A, Chaudhari A, Ogawa M (2003) Photoinduced electron-transfer along alpha-helical and coiled-coil metallopeptides. *Journal of the American Chemical Society* 125:357–362 Times Cited: 24.
- [130] Fedorova A, Ogawa M (2002) Site-specific modification of de novo designed coiled-coil polypeptides with inorganic redox complexes. *Bioconjugate Chemistry* 13:150–154 Times Cited: 11.
- [131] Hong J, Kharenko OA, Ogawa MY (2006) Incorporating electron-transfer functionality into synthetic metalloproteins from the bottom-up. *Inorg Chem* 45:9974–9984.
- [132] Crick F (1952) Is alpha-keratin a coiled coil? *Nature* 170:882–3.
- [133] Talbot J, Hodges R (1982) Tropomyosin: a model protein for studying coiled-coil and alpha-helix stabilization. *Accounts of Chemical Research* 15:224–230 Times Cited: 90.
- [134] Holtzer A, Holtzer M (1987) A statistical test of the proposition that intra-helix salt bridges constitute a significant stabilizing feature of the tropomyosin coiled-coil structure. *Macromolecules* 20:671–675 Times Cited: 2.
- [135] Schrödinger L (2010) The pymol molecular graphics system, version 1.3r1.
- [136] Frisch MJ, et al. (year?) Gaussian 03, revision c.02. Gaussian, Inc., Wallingford, CT, 2004.
- [137] Case D, et al. (2010) Amber 11. *University of California, San Francisco*.
- [138] Hornak V, et al. (2006) Comparison of multiple amber force fields and development of improved protein backbone parameters. *Proteins-Structure Function and Bioinformatics* 65:712–725.
- [139] Lee C, Yang W, Parr R (1988) Development of the colle-salvetti correlation-energy formula into a functional of the electron density. *Physical Review B* 37:785–789 Lee, ct yang, wt parr, rg.
- [140] Hay P, Wadt W (1985) Ab initio effective core potentials for molecular calculations. potentials for the transition metal atoms sc to hg. *Journal of Chemical Physics* 82:270–283 Hay, pj wadt, wr.
- [141] Bayly C, Cieplak P, Cornell W, Kollman P (1993) A well-behaved electrostatic potential based method using charge restraints for deriving atomic charges: the resp model. *J Phys Chem* 97:10269–10280 Bayly, ci cieplak, p cornell, wd kollman, pa.
- [142] Brandt P, Norrby T, Akermark E, Norrby P (1998) Molecular mechanics (mm3*) parameters for ruthenium(ii)-polypyridyl complexes. *Inorganic Chemistry* 37:4120–4127 Brandt, P Norrby, T Akermark, E Norrby, PO.

- [143] Kumar P, Mittal K (1999) *Handbook of Microemulsion Science and Technology* (Marcel Dekker, New York).
- [144] McCain DC, Markley JL (1985) Water permeability of chloroplast envelope membranes: In vivo measurement by saturation-transfer nmr. *FEBS Letters* 183:353 – 358.
- [145] Simons R (1993) A mechanism for water flow in bipolar membranes. *Journal of Membrane Science* 82:65 – 73.
- [146] Bart HJ, Jungling H, Ramaseder N, Marr R (1995) Water and solute solubilization and transport in emulsion liquid membranes. *Journal of Membrane Science* 102:103 – 112.
- [147] Marrink SJ, Berendsen HJC (1996) Permeation process of small molecules across lipid membranes studied by molecular dynamics simulations. *J. Phys. Chem.* 100(41):16729 – 16738.
- [148] Courel M, Dornier M, Rios GM, Reynes M (2000) Modelling of water transport in osmotic distillation using asymmetric membrane. *Journal of Membrane Science* 173:107 – 122.
- [149] Krylov AV, Pohl P, Zeidel ML, Hill WG (2001) Water permeability of asymmetric planar lipid bilayers: Leaflets of different composition offer independent and additive resistances to permeation. *J. Gen. Physiol.* 118:333–340.
- [150] Fornasiero F, Tang D, Boushehri A, Prausnitz J, Radke CJ (2008) Water diffusion through hydrogel membranes: A novel evaporation cell free of external mass-transfer resistance. *Journal of Membrane Science* 320:423 – 430.
- [151] Grime JMA, Edwards MA, Rudd NC, Unwin PR (2008) Quantitative visualization of passive transport across bilayer lipid membranes. *Proc Natl Acad Sci U S A* 105:14277–14282.
- [152] Mathai JC, Tristram-Nagle S, Nagle JF, Zeidel ML (2008) Structural determinants of water permeability through the lipid membrane. *J Gen Physiol* 131:69–76.
- [153] Lee D, Ashcraft JN, Verploegen E, Pashkovski E, Weitz DA (2009) Permeability of model stratum corneum lipid membrane measured using quartz crystal microbalance. *Langmuir* 25:5762–5766.
- [154] Colinart P, Delepine S, Trouve G, Renon H (1984) Water transfer in emulsified liquid membrane processes. *Journal of Membrane Science* 20:167 – 187.
- [155] Clausse D, Pezron I, Gauthier A (1995) Water transfer in mixed water-in-oil emulsions studied by differential scanning calorimetry. *Fluid Phase Equilibria* 110:137 – 150.
- [156] Zielinski RG, Kline SR, Kaler EW, Rosov N (1997) A small-angle neutron scattering study of water in carbon dioxide microemulsions. *Langmuir* 13:3934 – 3937.
- [157] Topgaard D, Malmberg C, Soderman O (2002) Restricted self-diffusion of water in a highly concentrated w/o emulsion studied using modulated gradient spin-echo nmr. *Journal of Magnetic Resonance* 156:195 – 201.
- [158] Wen L, Papadopoulos KD (2001) Effects of osmotic pressure on water transport in w1/o/w2 emulsions. *Journal of Colloid and Interface Science* 235:398 – 404.
- [159] Wen L, Papadopoulos KD (2000) Visualization of water transport in w1/o/w2 emulsions. *Colloids and Surfaces A: Physicochemical and Engineering Aspects* 174:159 – 167.
- [160] Evilevitch A, Jonsson BT, Olsson U, Wennerstrom H (2001) Molecular transport in a nonequilibrium droplet microemulsion system. *Langmuir* 17:6893–6904.
- [161] Deen GR, Oliveira CLP, Pedersen JS (2009) Phase behavior and kinetics of phase separation of a nonionic microemulsion of c12e5/water/1-chlorotetradecane upon a temperature quench. *J Phys Chem B* 113:7138–7146.

- [162] Deen GR, Pedersen JS (2010) Nucleation of an oil phase in a nonionic microemulsion-containing chlorinated oil upon systematic temperature quench. *J Phys Chem B* 114:7769–7776.
- [163] Fisher LR, Parker NS (1984) Osmotic control of bilayer fusion. *Biophysical Journal* 46:253 – 258.
- [164] Evilevitch A, Rescic J, Jonsson B, Olsson U (2002) Computer simulation of molecular exchange in colloidal systems. *J Phys Chem B* 106:11746–11757.
- [165] Jeon J, Voth GA (2008) Gating of the mechanosensitive channel protein mscl: The interplay of membrane and protein. *Biophysical Journal* 94:3497–3511.
- [166] Orsi M, Sanderson WE, Essex JW (2009) Permeability of small molecules through a lipid bilayer: A multiscale simulation study. *J Phys Chem B* 113:12019–12029.
- [167] Wang Y, Cohen J, Boron WF, Schulten K, Tajkhorshid E (2007) Exploring gas permeability of cellular membranes and membrane channels with molecular dynamics. *J Struct Biol* 157:534–544.
- [168] Aksimentiev A, Schulten K (2005) Imaging alpha-hemolysin with molecular dynamics: Ionic conductance, osmotic permeability, and the electrostatic potential map. *Biophysical Journal* 88:3745–3761.
- [169] Shinoda W, Mikami M, Baba T, Hato M (2004) Molecular dynamics study on the effects of chain branching on the physical properties of lipid bilayers: 2. permeability. *J Phys Chem B* 108:9346–9356.
- [170] Luo Y, Roux B (2010) Simulation of osmotic pressure in concentrated aqueous salt solutions. *J Phys Chem Lett* 1:183–189.
- [171] Bohanon TM, Lee A, Ketterson JB, Dutta P (1992) Surface-tension anisotropy and relaxation in uniaxially compressed langmuir monolayers. *Langmuir* 8:2497–2500.
- [172] Danov KD, Kralchevsky PA, Stoyanov SD (2010) Elastic langmuir layers and membranes subjected to unidirectional compression: Wrinkling and collapse. *Langmuir* 26:143–155.
- [173] Pocivavsek L, et al. (2008) Stress and fold localization in thin elastic membranes. *Science* 320:912–916.
- [174] Case DA, et al. (2005) The amber biomolecular simulation programs. *J Comput Chem* 26:1668–1688.
- [175] Wang J, Wolf RM, Caldwell JW, Kollman PA, Case DA (2004) Development and testing of a general amber force field. *Journal of Computational Chemistry* 25:1157–1174.
- [176] Wang J, Wang W, Kollman PA, Case DA (2006) Automatic atom type and bond type perception in molecular mechanical calculations. *Journal of Molecular Graphics and Modelling* 25:247260.
- [177] Miyamoto, S.; Kollman PA (1992) Settle: An analytical version of the shake and rattle algorithm for rigid water models. *J Comput Chem* 13:952–962.
- [178] Kohlbacher O, Lenhof HP (2000) Ballrapid software prototyping in computational molecular biology. *Bioinformatics* 16:815–824.
- [179] Abel S, Waks M, Marchi M, Urbach W (2006) Effect of surfactant conformation on the structures of small size nonionic reverse micelles: a molecular dynamics simulation study. *Langmuir* 22:9112–9120.
- [180] Senapati S, Berkowitz ML (2003) Molecular dynamics simulation studies of polyether and perfluoropolyether surfactant based reverse micelles in supercritical carbon dioxide. *The Journal of Physical Chemistry B* 107:12906 – 12916.
- [181] Chen YJ, Xu GY, Yuan SL, Sun HY (2006) Molecular dynamics simulations of aot at iso-octane/water interface. *Colloids and Surfaces A: Physicochemical and Engineering Aspects* 273:174 – 178.
- [182] Nymeyer H (2008) How efficient is replica exchange molecular dynamics? an analytic approach. *Journal of Chemical Theory and Computation* 4:626–636.
- [183] Abraham MJ, Gready JE (2008) Ensuring mixing efficiency of replica-exchange molecular dynamics simulations. *Journal of Chemical Theory and Computation* 4:1119–1128.

- [184] Winsor PA (1948) Hydrotropy, solubilisation and related emulsification processes. part i. *Transactions of the Faraday Society* 44:376–398.
- [185] Atilgan E, Wirtz D, Sun SX (2006) Mechanics and dynamics of actin-driven thin membrane protrusions. *Biophys J* 90:65–76.
- [186] Cramer LP, Briggs LJ, Dawe HR (2002) Use of fluorescently labelled deoxyribonuclease I to spatially measure G-actin levels in migrating and non-migrating cells. *Cell Motil Cytoskeleton* 51:27–38.
- [187] Quintero OA, et al. (2010) Intermolecular autophosphorylation regulates myosin IIIa activity and localization in parallel actin bundles. *The Journal of biological chemistry* 285:35770–35782.
- [188] Merritt RC, et al. (2012) Myosin IIIB Uses an Actin-Binding Motif in Its Espin-1 Cargo to Reach the Tips of Actin Protrusions. *Current Biology* 22:320–325.